



---

# SPATIALLY RESOLVED MOLECULAR EMISSION AS A TRACER OF THE PHYSICS AND CHEMISTRY OF YOUNG STARS

MASTER'S THESIS

Written by *Victoria Quist*

May 20, 2021

Supervised by

Jes Kristian Jørgensen

UNIVERSITY OF COPENHAGEN

An abstract geometric design consisting of several overlapping circles and lines, rendered in a light gray color, located in the bottom right corner of the page.



UNIVERSITY OF  
COPENHAGEN

NAME OF INSTITUTE: Niels Bohr Institute

NAME OF DEPARTMENT: Centre for Star and Planet Formation

AUTHORS: Victoria Quist

EMAIL: viq@science.ku.dk

TITLE: Spatially resolved molecular emission as a tracer  
of the physics and chemistry of young stars

SUPERVISORS: Jes Kristian Jørgensen

HANDED IN: May 20, 2021

# Contents

## Abstract

<b>1</b>	<b>Introduction</b>	<b>1</b>
1.1	Motivation and thesis outline . . . . .	1
1.2	Star formation . . . . .	2
1.2.1	Temperature profile . . . . .	7
1.3	Astrochemistry . . . . .	9
1.4	IRAS 16293-2422 . . . . .	12
1.5	Radiative transfer . . . . .	13
1.5.1	Line transfer . . . . .	16
1.5.2	Radiative transfer code . . . . .	16
<b>2</b>	<b>Observation</b>	<b>19</b>
<b>3</b>	<b>Line identification</b>	<b>20</b>
3.1	Contour maps of the identified lines . . . . .	24
<b>4</b>	<b>Einstein A coefficient and the structure of the molecule</b>	<b>29</b>
<b>5</b>	<b>The upper energy and the extent of the molecular emission</b>	<b>33</b>
5.1	IRAS16293B . . . . .	34
5.2	IRAS16293A . . . . .	37
5.3	Comparing IRAS16293A and IRAS16293B . . . . .	38
<b>6</b>	<b>Radiative transfer</b>	<b>42</b>
6.1	The temperature profile . . . . .	42
6.2	The empirical temperature profile . . . . .	45
6.3	The empirical and theoretical temperature profiles . . . . .	52
6.4	The temperature profile dependency on the luminosity . . . . .	55
<b>7</b>	<b>Conclusion and summary</b>	<b>64</b>
	<b>Acknowledgements</b>	<b>66</b>
	<b>References</b>	<b>66</b>
<b>A</b>	<b>Appendix: Contour maps</b>	<b>67</b>

# Abstract

Star formation is a complicated physical and chemical process. With the Atacama Large Millimeter/submillimeter Array (ALMA), it is possible to study chemistry on solar system scales. In addition, line rich spectra of a young stellar object help understand the chemistry during star formation because it is possible to look at complex organic molecules.

In this thesis, we analysed the binary system IRAS16293-2422 (IRAS16293), using the data from the ALMA Protostellar Interferometric Line Survey (PILS) and detailed dust and line radiative transfer simulations. Looking at different complex organic molecules, the structure of the molecule is studied. We investigated how the upper energy and the optical depth change the structure of the molecules. We also looked at the temperature profile for an optical thick envelope and how it matches the empirical temperature profile from the observed data from PILS. Furthermore, we tried to recreate the observed data with the radiative transfer simulations and looked further into the temperature profile for an envelope. Finally, a constrain on the luminosity of IRAS16293A and IRAS16293B is found from the empirical temperature profile.

For the analysis of the structure of IRAS16293B and the optical depth, it looks like they are related. However, more investigation needs to be done to make sure that there is a relationship. Furthermore, it also needs to be tested for other protostars. We found a correlation between the upper energy for a transition and the extent of the molecular emission. From this, we can say that the higher the upper energy is, the smaller is the extent of the emission from the line. This correlation represents the temperature profile for an optical thick envelope for the highest of the energies, the empirical temperature profile. We recreate the empirical temperature profile we saw in the observed data from PILS from the radiative transfer simulations. The empirical fits match well the outcome of the dust radiative transfer simulations with an inner optically thick and outer optically thin envelope. Finally, from an analysis of the change in luminosity compared with the temperature profile and the empirical temperature profile, it was possible to constrain the luminosities of the two sources in IRAS16293 to  $L_A = 13 L_{\odot}$  and  $L_B = 8 L_{\odot}$ . The difference in the luminosity can be due to the difference in the age, accretion rate, mass or size of the two protostars.



# 1 Introduction

## 1.1 Motivation and thesis outline

Star formation is a complicated process, which has been studied for many years. There are still many unknown factors and processes that we do not know the origin of. With the new technology and better telescopes, it becomes easier to zoom in on a smaller scale during star formation, and a lot of new information is gained.

Star forming region show rich and complex chemistry. Therefore it is essential to include astrochemistry when looking at star formation. Astrochemistry can help trace some of the physical parameters, especially in the earliest stage of star formation because of the extreme conditions. Furthermore, physics is important to understand the chemistry happening in the star formation regions. So, both physics and chemistry are vital to understanding the star formation process.

In this thesis, the aim is to understand some of the physical processes in star formation using astrochemistry. To do this, we look at different molecular transitions from spectra of a young stellar object, the binary system IRAS16293-2422. With the different transitions, the temperature profile of an envelope is explored by looking at the extents of the emissions from different molecular lines. Furthermore, detailed dust and line radiative transfer simulations are used to see if we can reproduce the data from IRAS16293-2422 and further investigate the temperature profile of its protostellar envelope.

In the rest of Section 1 is an introduction to star formation and astrochemistry. Furthermore, information about IRAS16293-2422, radiative transfer and the radiative transfer codes used in this project are introduced.

In Section 2 is the information about the ALMA *Protostellar Interferometric Line Survey* (PILS), which is the data used in this project.

Section 3 describes how to identify a line in a spectrum when the temperatures and the column densities are known. From an identified line, contour maps are made that are used for further analyses. These analyses are in Section 4 and 5. In Section 4 is the analysis of the optical depth, i.e. Einstein A coefficient and how the optical depth plays a role in the structure of the molecules. Finally, in Section 5 is the analysis of the upper energy and how it affects the extents of the emissions from different molecular lines.

The last analyses using the radiative transfer code is in Section 6. Here we investigate the temperature profile of an envelope, and the analysis in Section 5 continued by being compared to the radiative transfer data. Further in Section 6 is an analysis of the luminosity and the temperature profile.

Finally, in Section 7 is the conclusion for the analyses.

## 1.2 Star formation

The interstellar medium (ISM) consists of gas and dust. It is what fills the void between the stars in a galaxy. There are different phases to the ISM, distinguish by the density, temperature and whether the matter is atomic, molecular or ionised. One of these phases is the molecular clouds which mostly consist of molecular hydrogen. Molecular clouds have the highest density of all the phases in the ISM and the lowest temperature. The density is  $\geq 10^2$  atoms  $\text{cm}^{-3}$  and the temperature is around 10 – 20 K. To trace the molecular clouds, CO is most commonly used. This is because it has a relatively high abundance and it has frequent collisions, which makes it easy to trace. However, one problem with CO is that it becomes optically thick, meaning that the CO emission is absorbed and reemitted many times before it can escape the cloud because of the high density. Nevertheless, CO is still a useful tracer for the  $\text{H}_2$  in molecular clouds.  $\text{H}_2$  is not used to trace a molecular cloud because it does not have a dipole moment, and the temperature is too low to see other transitions. Molecular clouds are mostly seen in giant molecular cloud complexes, which have masses of  $\sim 10^5 M_\odot$  and diameters of  $\sim 50$  pc. It is in these giant molecular clouds that star formation occurs. The giant molecular clouds gravity is keeping the cloud cohesive, and we can ignore thermal pressure. So on large scales like the giant molecular cloud, we have that kinetic energy keeps the cloud from collapsing (Stahler & Palla, 2004).

In the giant molecular clouds, we have filaments, and these filaments have a preferred width of  $\sim 0.1$  pc. These filaments break into substructures called fibres. Fibres are relatively short compared to filaments, and they have a length of  $\sim 0.5$  pc. In these fibres, we have the dense cores where stars arise from. A dense core have a diameter of 0.1 pc and a mass of  $10 M_\odot$ . To start star formation, we need a gravitational collapse. This occurs when the gravitational energy becomes larger than the thermal energy. On larger scales (e.g. in the giant molecular cloud), we have that kinetic energy, i.e. turbulence support against gravitational collapse. On small scales, it is the thermal pressure that keeps the dense core from collapsing (Stahler & Palla, 2004). When the collapse will occur is described with the Jeans criterion, which says that it will collapse when the mass becomes larger than the Jeans mass. Jeans mass describe at what mass the thermal energy can no longer hold up the gravitational pressure, and the core will collapse. The Jeans mass is given by (Jeans, 1902):

$$M_J = \left( \frac{\pi c_s^2}{G} \right)^{3/2} \rho_0^{-1/2}$$

Where  $c_s$  is the isothermal sound speed in the cloud and  $\rho_0$  is its density. From this equation and the fact that  $c_s \propto \sqrt{T}$ , it is possible to see that a dense core of low temperature and high density has a high probability of undergoing gravitational

collapse.

After this brief introduction to molecular clouds, we will now look at different types of the collapse of the dense core.

There are broadly speaking three different scenarios for collapse (Stahler & Palla (2004), Hartmann (2008)). In order to look at the different collapse, we first need to derive the *free-fall time*. The free-fall time is the time it would take for a core to collapse under its own gravity if nothing else supports it against the collapse. To derive this, we look at the virial theorem, where we only have the term from gravity since nothing is giving support against it.

$$\begin{aligned} \frac{1}{2} \frac{\partial^2 I}{\partial t^2} &= \mathcal{W} \\ \frac{1}{2} \frac{\partial^2 I}{\partial t^2} &= \frac{1}{2} \frac{\partial^2 (MR^2)}{\partial t^2} = \mathcal{W} = -\frac{GM^2}{R_{eff}} \end{aligned}$$

When we solve this equation, we get the free-fall time:

$$t_{ff} = \sqrt{\frac{R_{eff}^3}{GM}} \quad (1)$$

Now that we have derived the free-fall time, we will look at the first scenario: the *uniform core*. For a uniform core, we have the same density throughout the entire collapsing core. For cores with constant densities, the inward acceleration is only determined by mass within a specific radius. We can consider a case where the particle is located far away from the centre of the core; the particle will have to travel far to reach the centre during the collapse. Most of the mass is located at smaller radii, which means that the gravitational pull in the particle far away will be significantly longer. We can then rewrite the free-fall time in Equation 1, so it only depends on density.

$$t_{ff} = \sqrt{\frac{3\pi}{32G\rho}} \quad (2)$$

This means that all of the material reaches the centre at the same time since the density is constant. A uniform core does not exist in nature because we need some kind of hydrostatic balance to have a core at all, so this is just theory. We then look at the second scenario, which is the *singular isothermal sphere*.

For the singular isothermal sphere, we have a core whose density increases toward the centre. For the singular isothermal sphere we have  $\rho \propto r^{-2}$  (or  $\rho^{-1/2} \propto$

$r$ ). Looking at the density in the free-fall time in Equation 2, we have that  $t_{ff} \propto \rho^{-1/2}$ , which means that we can write the free-fall time as a function of radius.

$$t(r) \approx t_{ff}(r) \propto \rho^{-1/2} \propto r$$

From this equation, we have that material closer to the centre will fall in more rapidly than the material coming from larger radii. This means that we get an inside-out collapse because the inner part of the core reaches the centre first and collapse. Inside the collapse the density profile will follow  $\rho \propto r^{-3/2}$  (free-fall) and outside  $\rho \propto r^{-2}$ . Furthermore, for a singular isothermal sphere, we have  $M_r \propto r$ . So the build-up of mass in the centre proceeds linearly in time, and the mass accretion rate is therefore constant. This scenario is not 100 % realistic, which brings us to the last scenario.

The third scenario is a *Bonnor-Ebert sphere*. For this scenario, we have a combination of the two previous ones. We have a uniform density core on small scales and a singular isothermal sphere on larger scales. In the inner part of the collapse, all material will reach the centre at the same time. This means that we have a high accretion rate at the beginning of the collapse, and later when we have a singular isothermal sphere, we then get a constant accretion rate and have the inside out collapse. Again, this scenario is not 100 % realistic. However, it is a good enough approximation.

From the previous section, it is essential to remember that we have  $\rho \propto r^{-p}$ , where  $p = 1.5$  is for free-fall, and  $p = 2$  is for the singular isothermal sphere. In the following section, we will look into what happens after the collapse has started and the classification of protostars.

After the collapse has started, the material will continue to fall into the central lump. The central lump then becomes more and more compress and will at some point become opaque to its own infrared radiation, meaning that the centre starts to heat. This results in hydrostatic equilibrium. Because there is an increase in temperature, there will also be an increase in pressure. The pressure then slows down material falling in, and as a result, it settles in the *first hydrostatic core* (Larson, 1969). The outer layer can still radiate energy freely, and the core grows in density and temperature but not in size. The size of the first core is a few AU, and the mass is  $\sim 0.05 M_{\odot}$ . Because the temperature keeps increasing, the temperature will reach 2000 K and collisional dissociation of  $H_2$  sets in. Most of the energy from the gravitational compression now goes to dissociation of  $H_2$ , and the temperature will start to increase slowly. Now the core quickly becomes unstable, and a second collapse will occur (Stahler & Palla, 2004).

The second core has a radius of a few solar radii, a mass of  $0.1 M_{\odot}$  and a temperature of  $\sim 10^5$  K. At this point, hydrogen becomes completely ionised

through collisions, and the gas settles down into another hydrostatic structure. Thus, the second hydrostatic core is what we call the protostar itself (Stahler & Palla, 2004).

Gas is now travelling at free-fall velocity to the protostar surface. This is faster than the sound speed, and it is supersonic. The cloud then proceeds with the inside-out collapse. At this point, the protostar is said to be in the *main accretion phase*. Because of the accretion onto the protostar, we have a release of gravitational energy. This radiates away as the accretion luminosity:

$$L_{acc} = \frac{GM_{star}\dot{M}}{R_{star}} \quad (3)$$

Where  $M_{star}$  and  $R_{star}$  is the stellar mass and radius, and  $\dot{M}$  is the mass accretion rate (Stahler & Palla, 2004).

Observation shows sign of a disk around protostars, but from the models of the spherical collapse, a disk should not form. This means that something else must go on to get a disk-like structure. The dense core has an initial rotation, so not all the material will collapse into the centre when the core collapse. Instead, some of the material will land on a circular disk and end up at a *centrifugal radius*. The centrifugal radius is where the gravitation pulls inwards is balanced by the rotation. A particle that comes from further out in the envelope, i.e. from a larger distance, will have larger angular momentum. This means that they will end up at a larger centrifugal radius. The centrifugal radius will therefore grow with time (Stahler & Palla, 2004).

Exactly when and how disk form remains unclear. However, at some point or another disk have to form around protostars. In the disk, the formation of planetary systems happens, and there are still many unanswered questions about planet and disk formation, but new observation helps to understand it. Furthermore, in the search for life on other planets, it is vital to understand the physics and chemistry in disks and planet formation.

After the second hydrostatic core and the protostar has formed, it is possible to classify the evolution of star formation based on the *Spectral energy distribution* (SED). First, star formation was only classified into three different stages; class I, II and III. Later, class 0 was added to incorporate the earliest stage of star formation. Class 0 and I are protostars, whereas class II and III are pre-main-sequence stars. Because of this, the SED for class 0 and I peaks at far-infrared and sub-millimetre wavelength, indicating that most of the emission comes from the cold dust. On the other hand, class II and III are characterised by peaking in the optical and near-infrared wavelength, where the emission comes from the

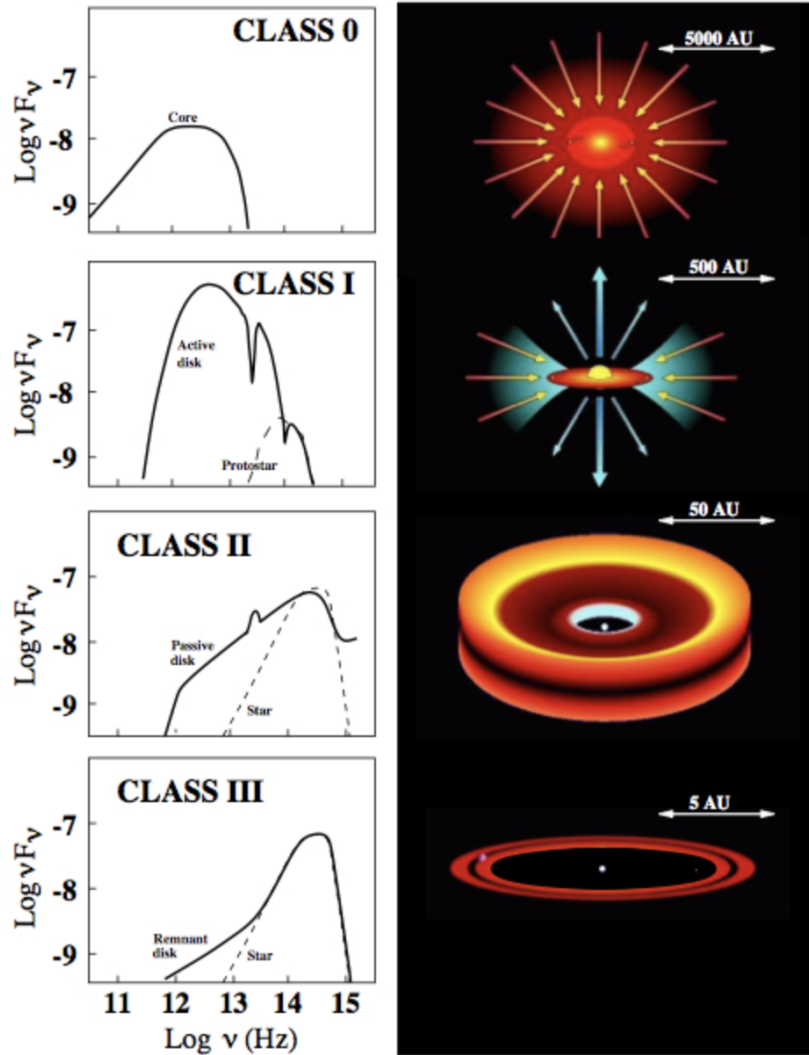


**Figure 1:** The different classes for star formation based on the spectral energy distribution and a schematic of them. (<https://ay201b.files.wordpress.com/2013/04/isella.jpg>)

stellar photosphere. In Figure 1, the SED and a schematic of the different classes can be seen. Here it is possible to see how the frequency becomes larger as the protostar evolves because of the envelope slowly disappearing (Stahler & Palla (2004), Hartmann (2008)).

**Class 0:** After the protostar has formed, it is still deeply embedded in a dusty envelope. The SED peaks at sub-millimetre wavelength, and they show collimated outflows at radio wavelength. The SED have a width of approximately a blackbody, but they have extremely low temperatures. This is because of the energy from the protostar being absorbed and then reemitted at longer wavelength. At this stage,

a protoplanetary disk is thought to be formed. The sources lifetime are in the order of  $\sim 2 \cdot 10^5$  yr (Stahler & Palla (2004), Dunham et al. (2015)).

**Class I:** At this stage, some of the envelope has been lost. The disk, as well as some of the envelope, is present. These sources have a broader black body function than for a class 0 and peaks at far-infrared and sub-millimetre wavelength. They have an excess of infrared emission compared to a normal photosphere, which comes from the dust around the protostar. They are sometimes detected in near-infrared, where this emission comes from scatted light. The age of these sources are  $\sim 4 \cdot 10^5$  yr (Stahler & Palla (2004), Dunham et al. (2015)).

**Class II:** Now that the envelope is gone, it is possible to see a dusty circumstellar disk, which is optically thick. This means that the SED still has some infrared excess. Like class I, the SED is broader than a typical black body, but it peaks in visible or near-infrared wavelength. Class II sources are also called *T-Tauri stars* (Hartmann, 2008).

**Class III:** The disk is not entirely gone, but not much is left. During the time as a class III source, only planetesimals and planets are left behind. The emission looks like a regular black body in the visible and infrared wavelength. They can have a little IR excess left from foreground dust and infall (Hartmann, 2008).

### 1.2.1 Temperature profile

The temperature profile of the dusty envelope around a protostar is different depending on where we look, i.e. it changes with the radius (Hartmann, 2008). This is because of the radiation and dust change across the envelope. The envelope can be divided into two different stages: an optical thick part and an optical thin part. Because of the two different stages in the envelope, the temperature profile will change depending on the region.

For the optically thin part, all radiation can escape freely. Therefore, to get the temperature profile for the optically thin case, it is possible to set the heating and cooling rate equal to each other. From this, the temperature as a function of the radius for the optically thin part is found (Hartmann, 2008):

$$T \propto r^{-2/(4+\beta)}$$

Here  $\beta$  is usual between 1.5 and 2 for the dust in the interstellar medium, and it depends on the dust opacity law. The opacity  $\kappa_\nu$  change with frequency, and  $\kappa_\nu \propto \nu^\beta$ .

For the optically thick part of the envelope, the radiation is trapped inside the envelope at small radii. The temperature profile then becomes steeper than the temperature profile for the optically thin case. To get the temperature for the

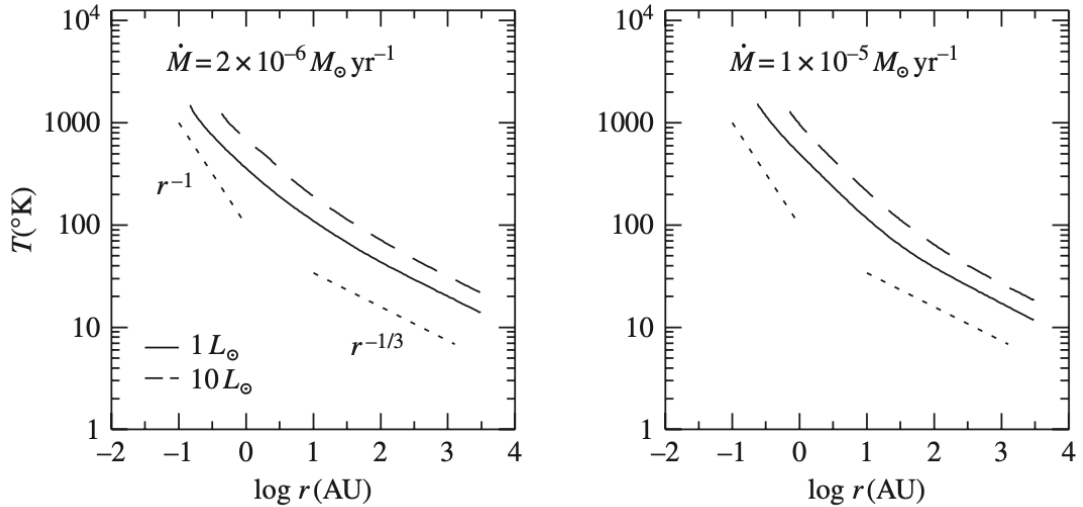


**Figure 2:** The temperature profile for models of a spherical envelope. There is two different mass accretion rate, where the one on the right-hand side is larger. The temperature profile for two different luminosities is shown on each plot, and the dotted lines are the theoretical temperature profile for the two different regimes (Hartmann, 2008).

optical thick case, we look at the usual diffusion approximation (Hartmann, 2008):

$$L = -\frac{64\pi\sigma r^2 T^3}{3\kappa_R \rho} \frac{dT}{dr}$$

Integrating this, with the boundary condition that when  $T \rightarrow 0$ ,  $r \rightarrow \infty$ , get the relationship between the temperature, radius and luminosity for the optical thick part of the envelope:

$$T \propto L^{1/(4-\beta)} r^{-(1+p)/(4-\beta)}$$

Where  $p$  is density dependency, and as mention earlier, we have that  $\rho \propto r^{-p}$  where  $p = 1.5$  is for a free-falling envelope, and  $p = 2$  is for a singular isothermal sphere.

In Figure 2, the temperature profile for two different envelopes is shown. Here the plot on the left-hand side has a lower mass accretion rate. The two dotted lines show the temperature profile, where we have the optically thick case closest to the centre with  $r^{-1}$ , so  $\beta = 1.5$  and  $p = 1.5$ . On the outer part of the envelope, we have the optically thin part, and the temperature profile follows  $r^{1/3}$  using  $\beta = 2$  (Hartmann, 2008).

To summaries, we have two different part of the temperature profile, depending



on if the envelope is optical thin or thick:

$$T \propto r^{-2/(4+\beta)} \quad \text{Optical thin} \quad (4)$$

$$T \propto r^{-(1+p)/(4-\beta)} \quad \text{Optical thick} \quad (5)$$

The luminosity of the envelope does not follow a classic black body. Instead, in the optically thick part of the envelope, the temperature follows the luminosity as:

$$T \propto L^{1/(4-\beta)} \quad (6)$$

In this section, we looked at the temperature profile of the optically thick and thin envelope. The temperature profiles are fundamental equations in this project, especially for an optical thick envelope. The following section is an introduction to astrochemistry and why chemistry is essential to understand physics.

### 1.3 Astrochemistry

Chemistry in space is quite different from chemistry on Earth. One of the biggest differences is the temperatures and densities found in space compared to that on Earth. On Earth, the temperature is around 300 K and the density is around  $3 \cdot 10^{19} \text{ cm}^{-3}$ . If we look at a dense core or a protostar, the temperature varies from 10 – 1000 K, and the density is  $10^4 - 10^{13} \text{ cm}^{-3}$ , which is a lot lower than on Earth. Because of the low density, unsaturated molecules are often seen in space. The same goes for several ions that rarely occur on Earth. (Jørgensen et al., 2020).

Over the past decade, a significant advance in astrochemistry has been made due to new technology and improvements in telescopes (Jørgensen et al., 2020). Because of the latest technology, it is possible to find various complex organic molecules (COM), especially in star formation regions. Herbst & Van Dishoeck (2009) define complex organic molecules as carbon molecules with six atoms or more. Complex organic molecules can be considered the building block for pre-biotic chemistry, and they can be divided into different categories depending on which elements they contain besides carbon and hydrogen. The most common COMs are O-bearing and N-bearing complex organic molecules, which contain oxygen and nitrogen, respectively. Complex organic molecules also differ from each other depending on how they are constructed. If a molecule has the same amount of carbon, hydrogen and oxygen but not the same structure, they are *isotopomers*. So they consist of the same number of each isotopic atom, but the position in the molecule is not the same. If two complex organic molecules have the same structure, but they only differ from each other by having one or more

atoms substituted, they are *isotopologs*. One example of this could be substituting hydrogen out with deuterium in a complex organic molecule Jørgensen et al. (2020).

In this project, different complex organic molecules are used. All of the molecules are O-bearing COM, and an isotopolog is used for one of the molecules. The reason why we used an isotopolog is that the primary molecule was too optically thick. If a molecule in an envelope is optically thick, it is only the outer layer of the envelope we see. Therefore it can be a good idea to use an isotopolog since there is less emission from an isotopolog than the primary molecule.

When talking about chemistry in star formation, the grain surface reaction is crucial (van Dishoeck, 1988). Some of the most complex organic molecules are thought to form on the grain surface. The formation of these molecules is too slow to happen in the gas phase chemistry, and the formation of  $\text{H}_2$  is evidence that grain surface chemistry exists since  $\text{H}_2$  cannot form by itself. For a grain surface reaction, we first have an atom that is colliding with a grain, and then the atom sticks to the grain. Another atom will also collide with the grain, and the two atoms will then go together and form a molecule on the grain surface. Depending on what molecules are formed on the grain, it will either leave the grain or stay on it like ice mantles. If the molecule remains on the grain, more atoms can come in, and it is possible to get complex organic molecules.

The chemistry inside protostellar cores is essential because they trace the physical conditions. At the beginning of the collapse, the envelope is cold like the dense core. This means that we have complex organic molecules forming on the grain surface like described above. As the protostar starts to form, the protostar begins to warm up the envelope, so the complex organic molecules can begin to sublime from the grain. The sublimation temperature is different for each molecule. As seen in Figure 3, the different molecules evaporate at different radii from the protostar as the temperature is highest at the protostellar core. Here we can see that CO evaporate further out in the envelope than  $\text{H}_2\text{O}$ . This is because the sublimation temperature for CO is lower than for  $\text{H}_2\text{O}$ . For more complex organic molecules like  $\text{CH}_3\text{OH}$ , the sublimation temperature is even higher, and therefore it only evaporates from the grain surface closest to the protostellar core. This is why it is possible to use chemistry to trace some of the physical parameters and vice versa (van Dishoeck, 1988).

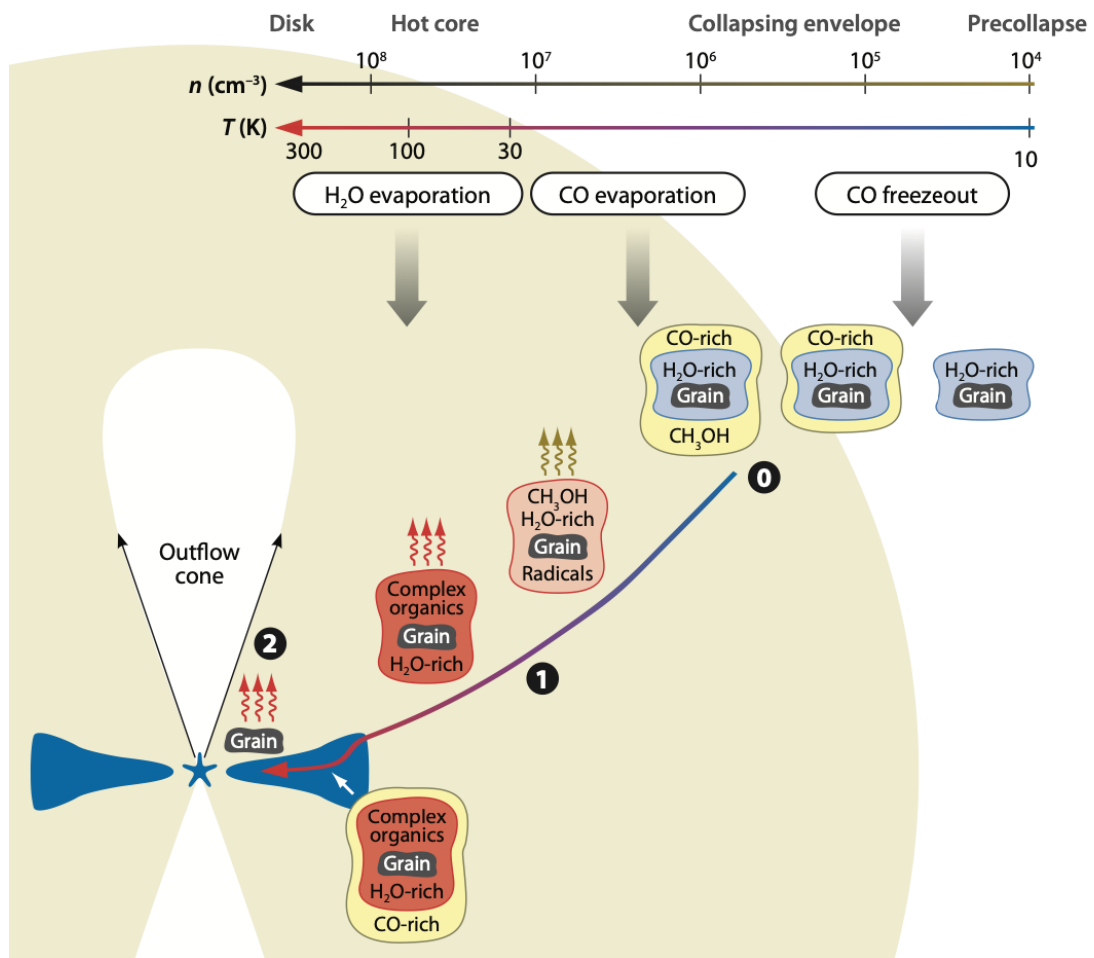


**Figure 3:** The evolution of complex organic molecules in grain surface chemistry. At the top, it is possible to see how the temperature change and how different molecules evaporate at different temperatures (Herbst & Van Dishoeck, 2009).

## 1.4 IRAS 16293-2422

In the last section, we have discussed astrochemistry. In this section, an overview of IRAS16293-2422 and the knowledge already obtained is presented in this section.

IRAS 16293-2422 (IRAS16293) is a well studied young stellar object. It is located in the L1689 region in the eastern part of the  $\rho$  Ophiuchus cloud complex (Jørgensen et al., 2016). The distance to IRAS16293 is  $141_{-21}^{+30}$  pc (Dzib, S. A. et al., 2018). IRAS16293 is a binary system that consists of IRAS16293A and IRAS16293B (seen Figure 4), and it is the first protostar to be classified as a binary system. The two protostars are separated by  $\approx 5.1''$ , and they both show continuum emission on 100 AU scales, which implies that they have a disk-like structure inside a circumbinary envelope. IRAS16293A is also a tight binary with a distance of about  $1''$  (120 AU). Both source A and B are classified as class 0 protostars, and source A is an edge on and source B a face on protostar (Jørgensen et al., 2016). The local-standard-of-rest (LSR) velocity for IRAS16293A and IRAS16293B is  $3.1$  and  $2.7$  km s $^{-1}$  respectively (Jørgensen, J. K. et al., 2011). The total luminosity is  $L = 21 \pm 5L_{\odot}$  (Jørgensen et al., 2016), which is found with a distance of 120 pc. Jacobsen et al. (2018) did 3D models to try to estimate the luminosity of the two protostars. They found that the luminosity of IRAS16293A is most likely much higher than IRAS16293B. Their best estimate of the luminosity is  $L_A \sim 18L_{\odot}$  and  $L_B \sim 3L_{\odot}$ . However, there are still uncertainties on what the specific luminosity of IRAS16293A and IRAS16293B is.

The outflow morphology is very complex for IRAS16293. It has two pair of outflow. One more collimated in the NE-SW direction and one that is less collimated in the E-W direction. The one in the NE-SW direction is said to be associated with IRAS16293A (Jørgensen et al., 2016). Regarding source B, there has been some debate whether or not there is an outflow associated with this protostar. Oya et al. (2018), presented SiO maps indicate outflows from source B. However they also suggest that this could be interaction with the outflows from source A.

The masses of the two protostars have tried to be estimated for years. Nevertheless, different methods yield different masses. However, all of the methods

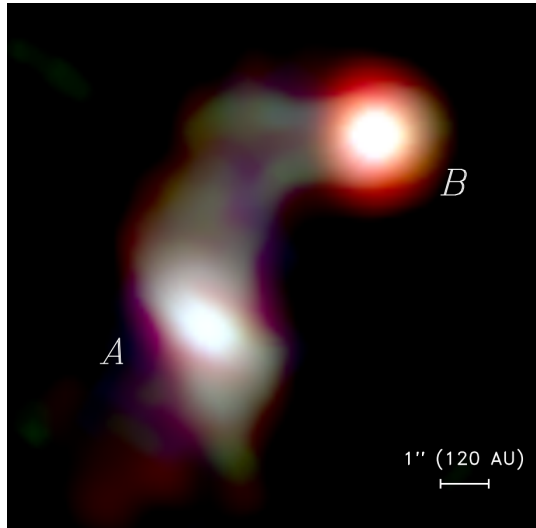


**Figure 4:** Three-colour image of IRAS 16293-2422 from Jørgensen et al. (2016)

shows masses inside the low-mass regime (van der Wiel et al., 2019).

IRAS16293 has mainly been observed with single-dish telescopes. Because of its rich spectra, IRAS16293 has been targeted in many single-dish and interferometric studies (see Jørgensen et al. (2016) for a survey). The data used in this thesis are from the Atacama Large Millimeter/submillimeter Array (ALMA) and obtained as part of the Protostellar Interferometric Line Survey (PILS; Jørgensen et al. (2016)). With the interferometric observations, it becomes possible to zoom in on a solar-system scale and study the presence of complex organic molecules observed toward sources such as IRAS16293. These molecules are present in the gas phase since the temperature is so high that grain ice-mantles have sublimated (Jørgensen et al., 2018).

Many COM has already been detected toward IRAS16293A (Manigand et al., 2020) and IRAS16293B (Jørgensen et al., 2018). This has been done by fitting synthetic spectra where the column density and the excitation temperature were free parameters. IRAS16293A has line widths which are approximately two to three time wider than IRAS16293B (Manigand et al., 2020). Because of the complexity of the protostars, e.g. emission being obscured by dust, offset positions were used for both protostars. The offset for IRAS16293A was 0.6'' in the NE direction, while the offset for IRAS16293B was 0.5'' in the SW direction (Calcutt, H. et al., 2018). The two sources are relatively close to each other, so they are expected to have similar molecular abundances and share the molecular heritage with the cloud. However, half of the species have a lower abundance with respect to CH<sub>3</sub>OH for IRAS16293A compared to IRAS16293B (Manigand et al., 2020).

## 1.5 Radiative transfer

In the following section, we will go over the basics of radiative transfer. This section is to a large degree based on the material from Stahler & Palla (2004) and the lecture notes from the course: *Radiative transfer in astrophysics* at the University of Heidelberg<sup>1</sup>. Lastly, in this section, we go into details about the radiative transfer code we use in this project.

When light is travelling through space, it is a complicated process. The light travels through a gaseous and dusty medium, which causes the light to be both absorpt and scatted. If we look at a radiation field, we can describe it by the specific intensity  $I_\nu$ , which is the energy per time. If we consider the light from a source travelling through a medium of length  $\Delta s$ , we need to find the change in

---

<sup>1</sup>[https://www.ita.uni-heidelberg.de/~dullemond/lectures/radtrans\\_2017/index.shtml?lang=en](https://www.ita.uni-heidelberg.de/~dullemond/lectures/radtrans_2017/index.shtml?lang=en)

the intensity  $\Delta I$ . When the light is travelling, the dust grains can remove some of the radiation by absorption and scattering, but it can also add radiation through thermal emission and scattering.

If we consider a medium that can absorb a photon, then the photon can travel one mean free path before being absorpt. The mean free path depends on how dense the medium is, so the denser the medium is, the smaller is the mean free path. Besides absorption, a photon can also be scatted. This means that the dust scatters a photon in a new direction, and the radiation is lost from our ray. We take absorption and scattering together as extinction in radiative transfer because both remove radiation from our ray. We use the extinction coefficient  $\alpha_\nu$  to write the negative contribution to our  $\Delta I$ . The extinction coefficient is given by the density  $\rho$  and the opacity  $\kappa_\nu$ , so we have that  $\alpha_\nu = \rho\kappa_\nu$ .

Besides removing radiation from the intensity, radiation can also be added. This can be done through emission, where the dust emits a photon into our ray. Radiation can also be added by scattering from another direction into our ray. The added radiation can be described as the emissivity  $j_\nu$ .

To sum up the change in intensity, we can look at Figure 5. This gives us the change in the specific intensity after travelling through a medium of a length  $\Delta s$ .

$$\Delta I_\nu = -\alpha_\nu I_\nu \Delta s + j_\nu \Delta s$$

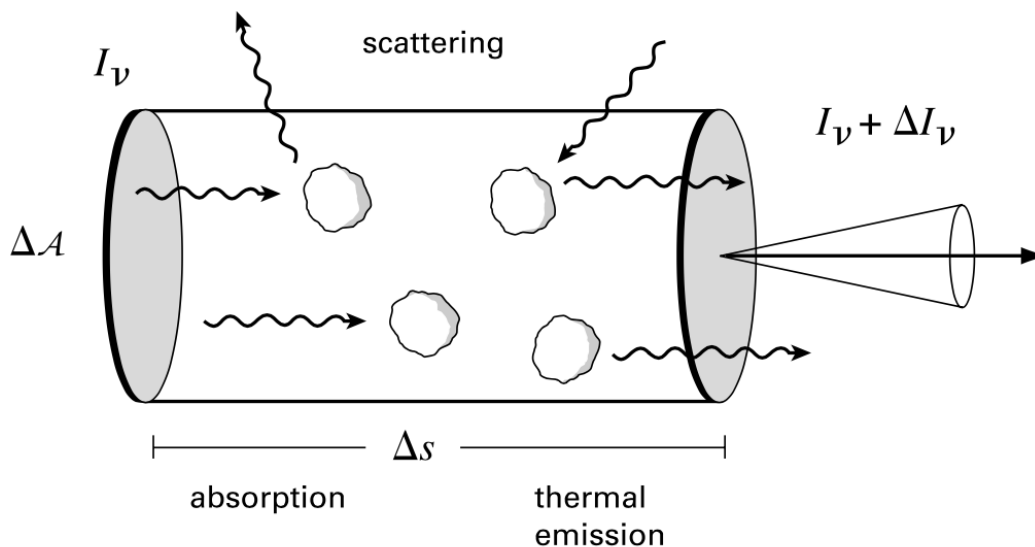


**Figure 5:** Light travelling through a dust medium, where we have the specific intensity  $I_\nu$  before, and after travelling  $\Delta s$ , the intensity has changed to  $I_\nu + \Delta I_\nu$  because of absorption, scattering and emission by grains (Stahler & Palla, 2004).

To get the *radiative transfer equation*, we divide with  $\Delta s$

$$\frac{\Delta I_\nu}{\Delta s} = -\alpha_\nu I_\nu + j_\nu \quad (7)$$

Another way to write the extinction coefficient is by the optical depth. We have  $\Delta\tau = \alpha_\nu \Delta s$ . The optical depth describes how dense a medium is and how likely a photon is to be absorpt. If a medium is optical thick ( $\tau \gg 1$ ), almost no emission escapes. However, if we have an optically thin medium ( $\tau \ll 1$ ), the radiation can travel freely, and absorption is negligible. Be aware that  $\kappa_\nu$  is dependent on the frequency, meaning that a medium can be optically thick at one frequency but optically thin at another frequency.

If we assume local thermal equilibrium (LTE), we need to satisfy the basic laws of thermodynamics. Let us consider a thermal cavity filled with gas with an extinction coefficient  $\alpha_\nu$ , and the gas is in LTE with a temperature  $T$ . The intensity should be equal to a Planck function:  $I_\nu = B_\nu(T)$ . For the radiative transfer equation, this means that  $\frac{\Delta I_\nu}{\Delta s} = 0$ . We can then rewrite Equation 7.

$$j_\nu - \alpha_\nu I_\nu = j_\nu - \alpha_\nu B_\nu(T) = 0$$

From this equation we get:

$$\frac{j_\nu}{\alpha_\nu} = B_\nu(T)$$

This is Kirchhoff's law, and it says that a medium in LTE can have any extinction and emissivity, as long as their ratio is the Planck function.

We do not always have LTE, but we can introduce the source function  $S_\nu$ , which we can use if we do not have LTE, and it becomes the Planck function if we have LTE.

$$S_\nu = \frac{j_\nu}{\alpha_\nu}$$

Now that we have the source function that holds when we have both LTE and non-LTE, we can write the radiative transfer equation (Equation 7) with the source function:

$$\begin{aligned} \frac{\Delta I_\nu}{\Delta s} &= -\alpha_\nu I_\nu + \alpha_\nu S_\nu \\ \frac{\Delta I_\nu}{\Delta s} &= \alpha_\nu (S_\nu - I_\nu) \end{aligned}$$

The intensity wants to approach the source function along the path of the ray. If  $S_\nu$  is constant, then  $I_\nu$  will approach the source function within a few mean free paths. However, if  $S_\nu$  is not constant,  $I_\nu$  will try to approach the source function but always lag behind.

Now we can write the radiative transfer equation with the optical depth instead of  $\Delta s$ . This can be done with the relation between  $\Delta\tau$  and  $\Delta s$ . We then get the radiative transfer equation:

$$\frac{\Delta I_\nu}{\Delta\tau} = S_\nu - I_\nu \quad (8)$$

### 1.5.1 Line transfer

Now that we have introduced the basic radiative transfer equation, we want to introduce the gas line transfer.

Gas line transfer comes from a transition between different energy levels in a molecule or atom. There are various ways these transitions can occur. One is a collision with another atom or molecules that allow them to jump from one energy level to another, called collisional transitions. Another way is sending out a photon or absorbing on. These transitions are called radiative transitions.

If we have LTE, we can use Boltzmann's distribution to calculate the level populations of a given molecule or atom. This can be done because when the density is high, the collisional transitions take place so often. If we do not assume LTE, it is not possible to use Boltzmann's distribution, and the collisional rate coefficient is then a good way to approximate the level populations. Sometimes, if the density is very low, radiative transitions can become more frequent than collisional transitions. If we have a non-LTE environment, the calculation of the level populations can become very difficult, and a complex radiative transfer code is needed.

### 1.5.2 Radiative transfer code

The radiative transfer code used in the project is *Ratran* (Hogerheijde & van der Tak, 2000). *Ratran* uses a monte Carlo method to calculate the level populations of a molecule without assuming LTE. This means that in order to use the code, the collisional rate coefficient of the molecule is needed. Furthermore, this code can take the absorption and the emission by dust into account, but scattering is neglected. Scattering is neglected because scattering usually does not play a role in wavelengths longer than mid-infrared.

The program uses the average intensity  $J_\nu$

$$J_\nu = \frac{1}{4\pi} \int I_\nu d\Omega \quad (9)$$

Where  $I_\nu$  is the solution to the radiative transfer equation, and  $d\Omega$  is all solid angles. To find the intensity, it is crucial to find the extinction coefficient and



the emissivity. Both dust particles and molecules are considered as sources of absorption and emission, so we have

$$\begin{aligned} j_\nu &= j_\nu(dust) + j_\nu(gas) \\ \alpha_\nu &= \alpha_\nu(dust) + \alpha_\nu(gas) \end{aligned}$$

The dust component in the emissivity is simply giving by the Planck function at the thermal temperature and the extinction is given by the dust opacity and the mass density of the dust:

$$\begin{aligned} j_\nu(dust) &= \alpha_\nu(dust) B_\nu(T_{dust}) \\ \alpha_\nu(dust) &= \kappa_\nu \rho_{dust} \end{aligned}$$

For the gas component, we look at the spectral line from one state to another, this gives us:

$$\begin{aligned} j_\nu^{ul}(gas) &= \frac{h\nu_0}{4\pi} n_u A_{ul} \phi(\nu) \\ \alpha_\nu^{ul}(gas) &= \frac{h\nu_0}{4\pi} (n_l B_{lu} - n_u B_{ul}) \phi(\nu) \end{aligned}$$

Where  $\phi(\nu)$  is the Doppler broadening that happens in the interstellar clouds due to the turbulent velocity field, and the Einstein  $A_{ul}$ ,  $B_{ul}$  and  $B_{lu}$  coefficients is the probability of emission or absorption.

The program comes in two separate part. The first part (*amc*) calculates the level populations of the molecule by solving the radiative transfer equation through a Monte Carlo simulation. The second part (*sky*) calculate the emission on the sky for a source that would be observed above the atmosphere and with perfect spatial resolution. The last part is calculated by simple ray tracing, but it needs the distance to the source, and it assumes spherical or cylindrical symmetry (Hogerheijde & van der Tak, 2000).

The level populations are found through the equation of statistical equilibrium:

$$n_l \left[ \sum_{k<l} A_{kl} + \sum_{k \neq l} (B_{lk} J_\nu + C_{lk}) \right] = \sum_{k>l} n_k A_{kl} + \sum_{k \neq l} n_k (B_{kl} J_\nu + C_{kl})$$

Here we have that collision and radiation determine the level populations.  $J_\nu$  depends on the CMB, dust and spectral lines, and the spectral line depends on the level populations. This means that  $J_\nu$  need to be solved iteratively through the Monte Carlo method.

The *amc* part is the Monte Carlo simulation, and it is used to find  $J_\nu$ . The basic idea is that from initial guesses for the level populations,  $J_\nu$  is found. Then

the statistical equilibrium equation is solved, and new level populations are made. Now from the new level populations, a new  $J_\nu$  is found, and the level populations are then updated again. This is done until the level populations and the radiation field has converged on a consistent solution.  $J_\nu$  is found by switching the integral in Equation 9 with the summation over a random set of directions. We can divide the *amc* part into two different parts, where for the first part, the radiation field is based on  $N_0$  rays per cell, which have a random direction and position. The series of random numbers used is the same.  $J_\nu$  and the level populations are then found until the largest difference between the populations in all cells of three subsequent solutions is ten times better than ultimately required. The second part of *amc* then starts. Here the same method is used, but before, it was the same series of random numbers used, and now new random numbers are used for each iteration. The last part of *amc* continues until all cells comply with the required accuracy (Hogerheijde & van der Tak, 2000). Now the population file is written, and the Monte Carlo part of *Ratran* is done. Finally, the sky part, the ray-tracing part of the program, can run with the population file from *amc*. This gives us a FITS file with the synthetic data.

Next, we will discuss what input the different part of the *Ratran* code needs and the various steps in this process. Finally, to give a better overview, a flow chart is created, seen in Figure 6.

Before we can use *Ratran*, we need a source file that describes the system we want to use the radiative transfer code on. To create this file, a separate code is used called *Transphere*. The *Transphere* code makes dust radiative transfer. It solves how the dust absorbs and emits radiation throughout the envelope of the protostar. From *Transphere*, the temperature profile of the envelope at different radii is calculated. When the *Transphere* code has solved the dust radiative transfer problem, it makes a source file for *Ratran*. This source file is divided into different shells. Each shell contains

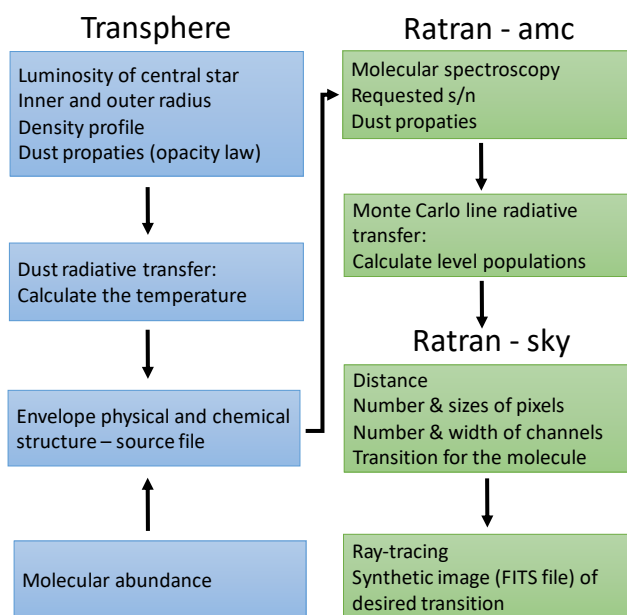


**Figure 6:** Flow chart of *Transphere* and *Ratran*.

the kinetic and dust temperature, the density of molecular hydrogen and the molecule and the inner and outer radius. Besides the source file, *amc* needs a molecular file that contains the frequencies, energy levels, Einstein A coefficients and collision rates coefficient for a transition. *Ratran* does not assume LTE, and therefore it needs the collisional rates for the molecule. The molecular file can be found in the Leiden Atomic and Molecular Database<sup>2</sup>.

## 2 Observation

In this section, we will give an introduction to the observation used in this project. The observation is made with the Atacama Large Millimeter Array (ALMA) telescope<sup>3</sup>. ALMA is the largest radio telescope globally, and it consists of 66 high-precision antennas, which works together as a single telescope, an interferometer. ALMA has fifty-four antennas with a diameter of 12 m and also twelve antennas with a diameter of 7 m. The antenna can be in a different configuration, spacing from 150 meters to 16 kilometres, where the angular resolution depend on how the antennas are placed. In addition, ALMA observes in different bands, where each band correspond to a specific frequency range.

The data on IRAS16293 used in this project comes from the ALMA PILS. It consists of an unbiased spectral survey, covering most of the ALMA’s Band 7 in ALMA’s Cycle 2 (project-id: 2013.1.00278.S) (Jørgensen et al., 2016), but also a selected window of the ALMA’s band 3 and 6 obtained in Cycle 1 (project-id: 2012.1.00712.S). In this project, only the data from the ALMA’s band 7 is used. The continuum has already been subtracted by Jørgensen et al. (2016) as described in their article.

The data cover the frequency from 329.147 GHz to 362.896 GHz, with an angular resolution of 0.5”, and both the 12 m dishes and the 7 m dishes were used. The centre of the observations is between the two sources, IRAS16293A and IRAS16293B and is located at  $\alpha_{J2000} = 16^{\text{h}}32^{\text{m}}22^{\text{s}}.72$ ;  $\delta_{J2000} = -24^{\circ}28'34''.3$ . In total, 18 spectral settings were observed, where each spectral range was divided into four spectral windows. This gives us a total of 72 datacubes, each covering a spectral window of 468.75 MHz over 1920 channels, which gives us a spectral resolution of 0.244 MHz. The data have a noise RMS of  $\sim 7-10$  mJy beam<sup>-1</sup> channel<sup>-1</sup>. For more details on the observation, e.g. how the data were calibrated, see Jørgensen et al. (2016).

For analysis of spectra, around the two sources, we used an offset position. This is to account for the line emission being obscured by dust and because a

<sup>2</sup><https://home.strw.leidenuniv.nl/~moldata/>

<sup>3</sup><https://www.almaobservatory.org/en/home/>

large number of molecules has already been detected at these positions (Calcutt, H. et al., 2018). At the chosen position for IRAS16293B the lines are bright, but do not have strong absorption features. The position is one beam offset  $\sim 0.5''$  in the southwest direction, at  $\alpha_{J2000} = 16^{\text{h}}32^{\text{m}}22^{\text{s}}.58$ ;  $\delta_{J2000} = -24^{\circ}28'32''.8$ . For IRAS16293A, a  $0.6''$  offset position in the northeast direction was chosen, at  $\alpha_{J2000} = 16^{\text{h}}32^{\text{m}}22^{\text{s}}.9$ ;  $\delta_{J2000} = -24^{\circ}28'36''.2$ . The FWHM of the lines at the offset position for source B is  $\sim 1 \text{ km s}^{-1}$ , and for source A, the FWHM is  $\sim 2-3 \text{ km s}^{-1}$ . Because the lines are broader for source A, line blending can be a problem when identifying and analysing lines of different molecules.

### 3 Line identification

This section will go over how to identify an emission line in a spectrum and create contour maps of the lines we identify. From the contour maps, further analysis happens in Section 4 and 5.

The frequency on the spectra we get from the data, need to be corrected for Doppler shift. This is due to the local LSR velocity of our sources that we need to take into account. For IRAS16293B, the LSR is  $2.7 \text{ km s}^{-1}$ , so the Doppler formula is used:

$$\frac{\Delta\nu}{\nu} = \frac{\Delta v}{c} \Rightarrow \Delta\nu = \nu \frac{\Delta v}{c} \quad (10)$$

Where  $\Delta\nu$  is the change in frequency, which we need to add to our initial frequency  $\nu$ , and  $\Delta v$  is our change in velocity, which is our LSR.

The frequency range for IRAS16293B can now be corrected for Doppler shift. However, for IRAS16293A, we have a large velocity gradient across the source. This means that we cannot change the frequency with a constant velocity. So instead, Calcutt, H. et al. (2018) VINE (Velocity-corrected Integrated Emission) Maps are used. For the VINE maps, we have a velocity key. In this document, the velocity at each pixel, where there is emission, is given. We can Doppler shift the frequency range for each pixel with the velocity key, so we have the correct frequency range for IRAS16293A no matter what position we are looking at.

We now have the right frequency for the spectra from both sources, so we can start to identify molecular lines. We get the spectroscopic data from two different catalogues, depending on the molecules. The two catalogues are The Cologne Database for Molecular Spectroscopy<sup>4</sup> (CDMS) and Jet Propulsion Laboratory<sup>5</sup> (JPL). For the analysis in this project, a handful of different O-bearing COMs are

<sup>4</sup><https://cdms.astro.uni-koeln.de/classic/entries/>

<sup>5</sup><https://spec.jpl.nasa.gov/ftp/pub/catalog/catdir.html>

used. Before the molecules are used, we have to check if the molecules are too optically thick, meaning that the radiation cannot escape the envelope. If they are too optically thick, we only see the outer emission for the molecules. This was a problem with CH<sub>3</sub>OH, so instead, an isotopolog that is not optical thick is used.

We now want to identify an emission line in the spectrum. With the data from the catalogues, it is possible to see when a molecule will have a transition, and thereby when there will be an emission peak in the spectrum. However, multiple molecules can have a transition at the same frequency. Therefore, just because a molecule has a transition at a specific frequency does not mean that we see an emission line in the spectrum. So we need to see if the emission line in the spectrum is the molecule we suspect. In the next few pages, we will go over the equations used to identify a line in a spectrum.

To investigate if the emission line is the suspected molecule, we plot a Gaussian function that is supposed to resemble the emission peak of the molecule we look at. If the Gaussian function matches the emission peak, we can say that the emission peak must come from that molecule. To fit a Gaussian function, we need an amplitude,  $\sigma$  and the transition frequency. From the catalogue, it is possible to get the frequency at where the emission peak would be. From the emission peak in the spectrum we can get the FWHM, and then transform it into  $\sigma$  because  $\text{FWHM} = 2\sqrt{2\ln(2)}\sigma$ . The last thing we need is then the amplitude in units of Jy/beam because this is the unit we have for the intensity in the spectra. To find the amplitude for our Gaussian function, we need to find the line strength for a given excitation for one of the molecules first. We can use the following equation, which is a combination of Equation 8, 15 and 19 from Goldsmith & Langer (1999):

$$\int T_B dv = \frac{A_{ul}c^3h}{8\pi k\nu^2} \frac{g_u}{Z(T)} \exp\left(-\frac{E_u}{kT_{ex}}\right) N_T \quad (11)$$

$\int T_B dv$  is the line strength we want to find,  $Z(T)$  is the partition function, and  $g_u$  is the upper state degeneracy. To use this equation, we have assumed LTE and optical thin emission.

Before we use Equation 11, some extra factors need to be taken into account to get the Gaussian function to represent the data as much as possible. The first thing to take into account is the beam-filling factor. The equation for the beam-filling factor assuming a Gaussian beam and distribution of the emission is (Wilson, 2009):

$$f_{BEAM} = \frac{\theta_s^2}{(\theta_s^2 + \theta_b^2)}$$

Here  $\theta_b^2$  is the beam size and  $\theta_s^2$  is the actual source size. In our case the beam size is 0.5'' and we assume that the extent of the emission is 0.5'' (Jørgensen et al.,

2016), so we get:

$$f_{BEAM} = \frac{0.5^2}{(0.5^2 + 0.5^2)} = \frac{0.25}{(0.25 + 0.25)} = 0.5$$

This needs to be added to Equation 11, but we will look at the optical depth before doing this.

For Equation 11 we assume that the emission is optically thin, but we do not know if this is true. If we find the optical depth,  $\tau$ , it is possible to check if the emission is optical thin or not. To find the optical depth, Equation 6 from Goldsmith & Langer (1999) is used. Furthermore, we get  $N_u$  from Equation 19, and the relationship between the Einstein A and B coefficient is described above Equation 7 (Goldsmith & Langer, 1999). This then gives us:

$$\begin{aligned} \tau &= \frac{h}{\Delta\nu} N_u B_{ul} \left( \exp\left(\frac{h\nu}{kT}\right) - 1 \right) \\ B_{ul} &= A_{ul} \frac{c^3}{8\pi h\nu^3} \\ N_u &= \frac{N}{Z} g_u \exp\left(-\frac{E_u}{kT}\right) \end{aligned} \quad (12)$$

Which we can rewrite to get one equation for the optical depth

$$\tau = \frac{h}{\Delta\nu} \frac{N}{Z} g_u \exp\left(-\frac{E_u}{kT}\right) A_{ul} \frac{c^3}{8\pi h\nu^3} \left( \exp\left(\frac{h\nu}{kT}\right) - 1 \right)$$

If we have optical thick emission, the emission peak will be lower than expected. So to account for the optical depth, we divide our line strength in Equation 11 with a factor. This factor comes from Equation 16 in Goldsmith & Langer (1999)

$$C_\tau = \frac{\tau}{1 - \exp(-\tau)}$$

If we have optical thin emission ( $\tau \ll 1$ ),  $C_\tau \rightarrow 1$ , which means that this will not affect the line strength. Nevertheless, if we do not have optical thin emission, this factor will change the line strength to match the data better.

We can now write the final equation for the line strength:

$$\int T_B dv = \frac{A_{ul} c^3 h}{8\pi k\nu^2} \frac{g_u}{Z(T)} \exp\left(-\frac{E_u}{kT_{ex}}\right) N_T \frac{f_{BEAM}}{C_\tau}$$

For our Gaussian function, we need the amplitude instead of the line strength. The line strength is the integral of the Gaussian function, and the integral of a Gaussian function is<sup>6</sup>:

$$\int_{-\infty}^{\infty} e^{-\alpha x^2} dx = \left(\frac{\pi}{\alpha}\right)^{1/2}$$

Here we have that in the Gaussian function,  $\alpha = \frac{1}{2\sigma^2}$ . We also need to remember that in the Gaussian function, we have the amplitude multiplied on. This gives us

$$\text{Line strength} = \text{amplitude} \times (\pi 2\sigma^2)^{1/2}$$

We know that  $\text{FWHM} = 2\sqrt{2\ln(2)}\sigma$ . So if we insert this in the equation above, we get

$$\text{Line strength} = \text{amplitude} \times \left(\frac{2\pi\text{FWHM}^2}{(2\sqrt{2\ln(2)})^2}\right)^{1/2} = \text{amplitude} \times \text{FWHM} \times 1.064$$

Where we have that  $\left(\frac{2\pi}{(2\sqrt{2\ln(2)})^2}\right)^{1/2} = 1.064$ . This means that we can now find the amplitude of the Gaussian function with the following relationship:

$$\text{Amplitude} = \frac{\text{line strength}}{1.064 \times \text{FWHM}}$$

Now that we have the amplitude, we need it in the correct unit to match the data. The line strength is in units of temperature times velocity, so we need the FWHM to be in units of velocity instead of GHz to get the amplitude in temperature. To get the FWHM in velocity, we use Equation 10, where we want to find  $\Delta v$  and we have that  $\nu$  is our frequency at the peak and  $\Delta\nu$  is our FWHM is GHz. We then get the amplitude in temperature. However, we want the amplitude in units of Jy/beam, which can be done with the following formula that comes from the Rayleigh-Jeans law (Wilson, 2009):

$$\left(\frac{I_\nu}{\text{Jy/beam}}\right) = \frac{1}{13.6} \left(\frac{T_\nu}{\text{K}}\right) \left(\frac{\lambda}{\text{mm}}\right)^{-2} \left(\frac{\theta_b^2 \cdot \theta_b^2}{1'' \cdot 1''}\right)$$

Again  $\theta_b^2$  is  $0.5''$ .

We can now plot the Gaussian function with our spectrum and see if the line we want to identify matches the Gaussian function. We need to have the temperature and column density for each molecule at the position where we are looking.

<sup>6</sup><http://www.umich.edu/~chem461/Gaussian%20Integrals.pdf>

IRAS16293 is a well-studied object, so the temperatures and column densities are already known for many COMs. For our analysis, the column density and temperature for the different molecules is in Table 1 in Jørgensen et al. (2018) for IRAS16293B and in Table 1 in Manigand et al. (2020) for IRAS16293A. The numbers are also in Table 1. The way Jørgensen et al. (2018) and Manigand et al. (2020) found the temperature and the column density for the different molecules was by fitting the spectral lines in the data with synthetic spectra as mention in Section 1.4. This is the opposite of what we are doing when identifying a line.

**Table 1:** Column densities and temperatures for the molecules for the two different protostars at the offset position. Furthermore is the range of the upper energy used in the analysis of the structure of the contour maps in Section 4 and the range of the Einstein A coefficient used in the analysis of the upper energy and the extents of the emissions from different molecular lines is in Section 5.

Source	Molecule	Column density [ $\text{cm}^{-2}$ ]	Temperature [K]	Range of $\log(A_{ji})$ [ $\text{s}^{-1}$ ]	Range of $E_{upper}$ [K]
IRAS16293B	CH <sub>3</sub> CHO	$1.2 \times 10^{17}$	125	[-2.7 : -3.0]	[152 : 341]
IRAS16293B	<sup>13</sup> CH <sub>3</sub> OH	$1.6 \times 10^{17}$	300	[-3.3 : -4.6]	–
IRAS16293B	CH <sub>3</sub> OCHO	$2.6 \times 10^{17}$	300	[-3.1 : -3.3]	[252 : 338]
IRAS16293B	CH <sub>3</sub> OCH <sub>3</sub>	$2.4 \times 10^{17}$	125	[-3.4 : -4.0]	–
IRAS16293B	C <sub>2</sub> H <sub>5</sub> OH	$2.3 \times 10^{17}$	300	–	[57 : 335]
IRAS16293A	CH <sub>3</sub> CHO	$3.5 \times 10^{15}$	140	[-2.7 : -2.9]	–
IRAS16293A	CH <sub>3</sub> OCHO	$2.7 \times 10^{17}$	115	[-3.1 : -3.3]	–
IRAS16293A	CH <sub>3</sub> OCH <sub>3</sub>	$5.2 \times 10^{17}$	100	[-3.4 : -4.0]	–

An example of one line identified for both sources are in Figure 7. It is the same line shown for IRAS16293A and IRAS16293B. The red line is the Gaussian fit, and from the fit, it is possible to say that the emission line must be CH<sub>3</sub>CHO.

### 3.1 Contour maps of the identified lines

We have now identified different emission peaks from different molecules, and each emission peak is turned into a contour map. We make the emission peak into a contour map to see how the protostar looks and because the contour maps are used for further analyses in Section 4 and 5.

In Section 4 we look at the correlation between the contour maps and the optical depth, i.e. the Einstein A coefficient. In Section 5 we look at the correlation between the upper energy and the extents of the emissions from different molecular lines.

For the contour maps used in Section 4 we kept the upper energy as constant as possible to eliminate any changes this may have on the analysis. Likewise, in



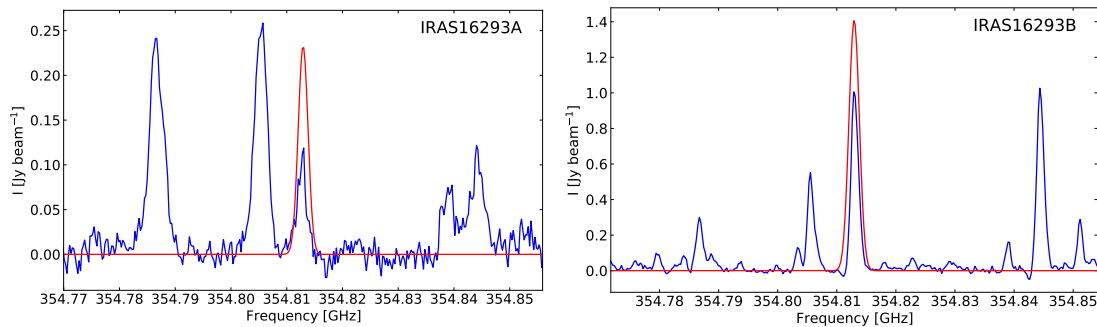


**Figure 7:** The PILS data (blue) and a fitted Gaussian function (red) to identify a line. The identified line is  $\text{CH}_3\text{CHO}$  with a frequency of 354.81 GHz. The left plot is from the offset position of IRAS16293A, and the right plot from the offset position of IRAS16293B.

Section 5 we kept the Einstein A coefficient as constant as possible to eliminate the change this might give.

To create a contour map from an emission peak, we integrate over the width of the emission line. We do this to get the intensity of the emission peak across the source. We then get a 2D array, where we have the intensity of the emission peak at each position for the source.

When we have the contour map, we want to plot the different levels of contours expressed by the error of the integrated line intensity  $\sigma$ . We find  $\sigma$  from the RMS. The RMS is found by taking a point away from both sources to ensure no emission comes from the sources.

$$RMS = \sqrt{\text{mean}(I^2)}$$

Here  $I$  is the intensity at the chosen point away from both sources. With the RMS, it is possible to find  $\sigma$

$$\sigma = \sqrt{N} \cdot RMS$$

Where  $N$  is the number of channels integrated over to get the contour map.

When the error ( $\sigma$ ) is found, the contour maps for the different transitions are made. For IRAS16293A the width of the integrated emission, in order to make the contour map, is  $5 \text{ km s}^{-1}$ , and for IRAS16293B, the width is  $2 \text{ km s}^{-1}$ . The contour maps for  $\text{CH}_3\text{CHO}$  for IRAS16293A is in Figure 8. These contour maps are made with the velocity key from Calcutt, H. et al. (2018) because of the large velocity gradient across the source. The width of the emission peak for IRAS16293A is  $5 \text{ km s}^{-1}$  even though the width of the emission peak change across the protostar. At the centre of the protostar, the width of the transition is  $\sim 10 \text{ km s}^{-1}$ . We then chose a width of  $5 \text{ km s}^{-1}$  because we are not interested in resolving the emission at the centre. The reason for that is when we use the extent of the emission from

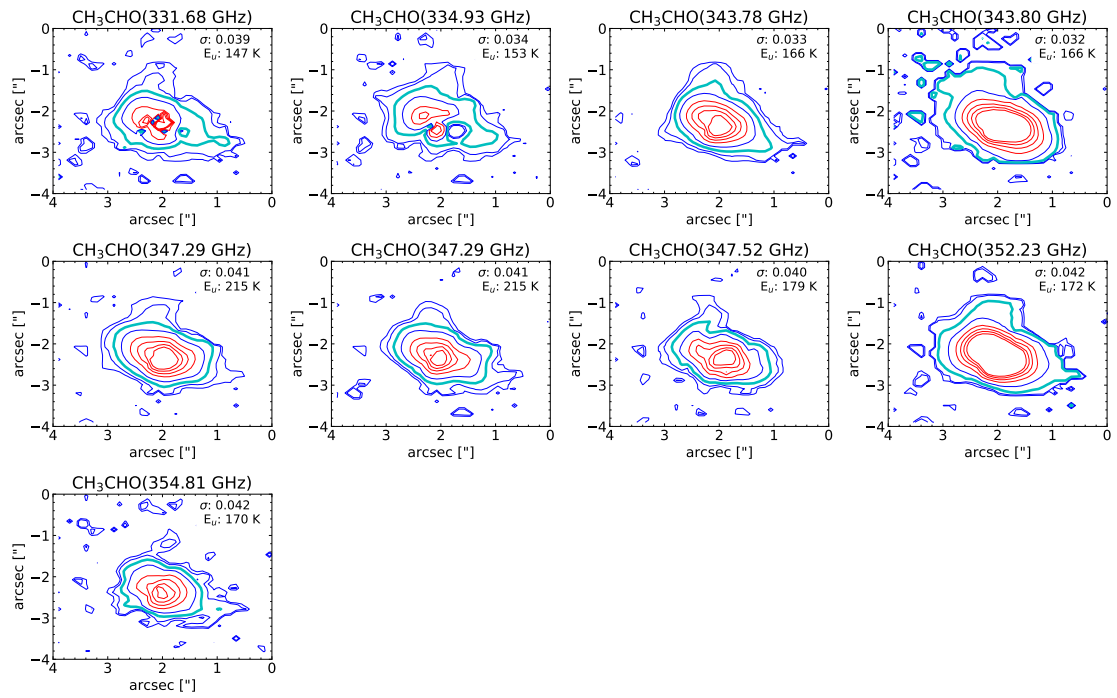


**Figure 8:** Contour maps of  $\text{CH}_3\text{CHO}$  for IRAS16293A. The different levels are for  $3\sigma$ ,  $5\sigma$ ,  $10\sigma$ ,  $20\sigma$ ,  $40\sigma$ ,  $60\sigma$ ,  $80\sigma$ ,  $100\sigma$ , where the  $10\sigma$  contour is in cyan. The upper energy and  $\sigma$  is displayed on the plots. These contour maps are VINE maps (Calcutt, H. et al., 2018).

the line for the analysis in Section 5, we do not have to resolve the centre part of the emission, but we use the  $10\sigma$  contour. This lays further out, as seen in Figure 8 in cyan. Even though the width of the transition change across IRAS16293A, the width of  $5\text{ km s}^{-1}$  is the best possible fit to avoid too much line blending. It is also the best way to get the line resolved as much as possible at the  $10\sigma$  contour.

Figure 9 shows a subset of the contour maps for  $\text{CH}_3\text{CHO}$  toward IRAS16293B (the rest can be found in Appendix A). From the contour maps for IRAS16293B, there is an indication of a correlation between the upper energy and the extent of emission from the molecular lines. The correlation shows that molecular lines with higher values of  $E_u$  show more compact emission. To test this correlation, the area inside the  $10\sigma$  contour is found. This is shown as cyan in the figure, and the analysis is in Section 5. Only the upper energy is shown in the contour maps because, in this analysis, we kept the Einstein A coefficient as constant as possible.

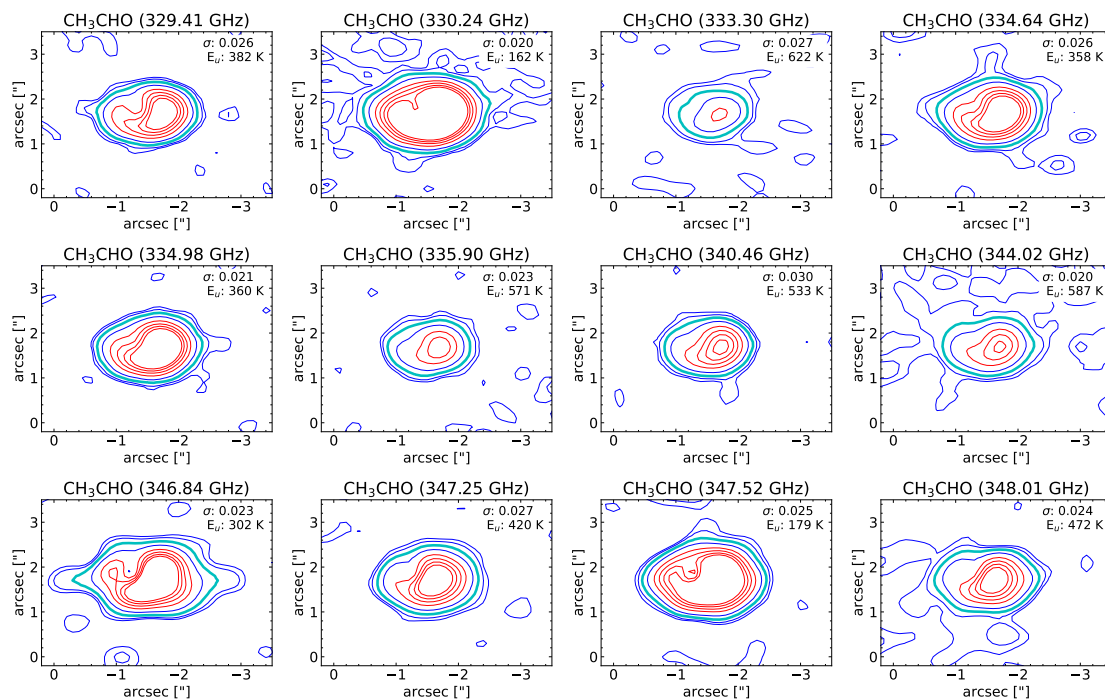


**Figure 9:** A subset of the contour maps of  $\text{CH}_3\text{CHO}$  for IRAS16293B. The different levels are for  $3\sigma$ ,  $5\sigma$ ,  $10\sigma$ ,  $20\sigma$ ,  $40\sigma$ ,  $60\sigma$ ,  $80\sigma$ ,  $100\sigma$ , where the  $10\sigma$  contour is in cyan. The upper energy and  $\sigma$  is displayed on the plots.

In Figure 9, we can see that there is a feature in the maps for IRAS16293B. The feature we are talking about lays around  $[-1''; 2'']$  in the contour maps. This feature might have something to do with the optical depth, and therefore the

Einstein A coefficient. To investigate the origin of this feature, we select lines with similar values of  $E_u$  but varying  $A_{ul}$ . These can be seen in Figure 10, and here the Einstein A coefficient is on the plot because this is the parameter that we varied. From the figure, it looks like there is an indication of a correlation between the Einstein A coefficient and the feature of the molecule. We return to this in Section 4.

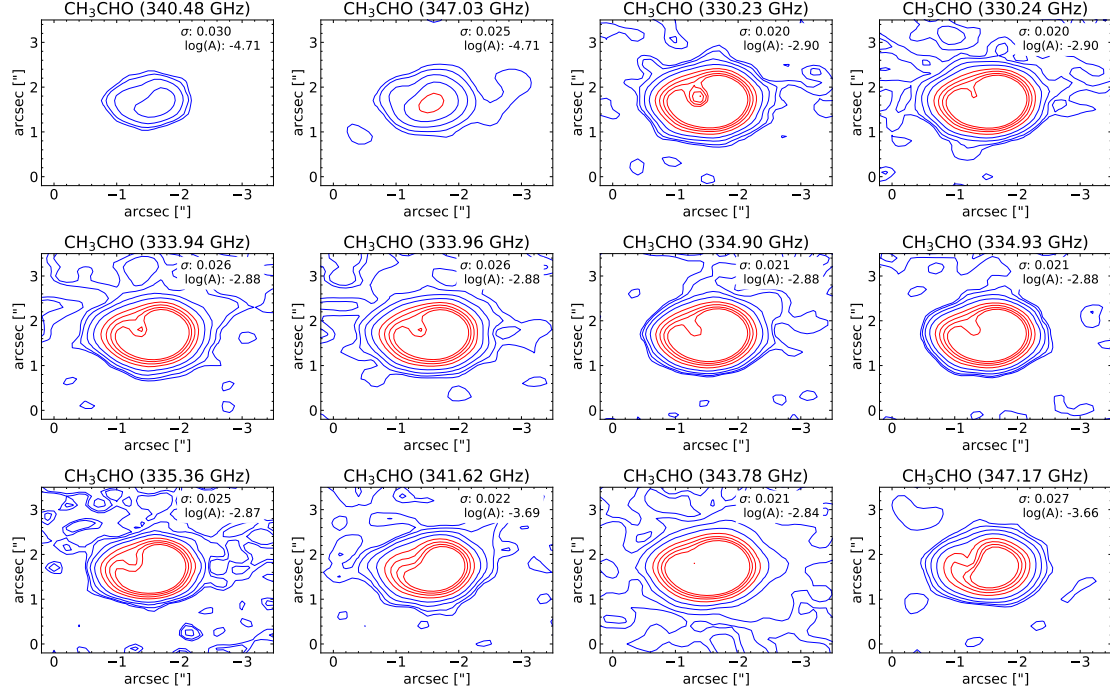


**Figure 10:** A subset of the contour maps of  $\text{CH}_3\text{CHO}$  for IRAS16293B. The different levels are for  $3\sigma$ ,  $5\sigma$ ,  $10\sigma$ ,  $20\sigma$ ,  $40\sigma$ ,  $60\sigma$ ,  $80\sigma$ ,  $100\sigma$ . The Einstein A coefficient and  $\sigma$  is displayed on the plots.

The contour maps for  $^{13}\text{CH}_3\text{OH}$  for IRAS16293B is in Figure 11. Here the structure of the molecule differs from the structure of  $\text{CH}_3\text{CHO}$  for IRAS16293B (Figure 9 and 10). We do not see the same feature around  $[-1''; 2'']$  with the different structure. This is the feature that we suspect to have something to do with the optical depth, and because we do not see it in the contour map of  $^{13}\text{CH}_3\text{OH}$ , it is not included in the analysis of the feature of the molecule. However, we still use it in the analysis of the energy and the extent of the emission line. We have investigated different molecules to find the molecules with the same structure and feature as we see in the contour maps of  $\text{CH}_3\text{CHO}$ .

Looking at Figure 8, we do not see the feature of the molecule either. Therefore, the analysis where we investigate this feature is only done for IRAS16283B.

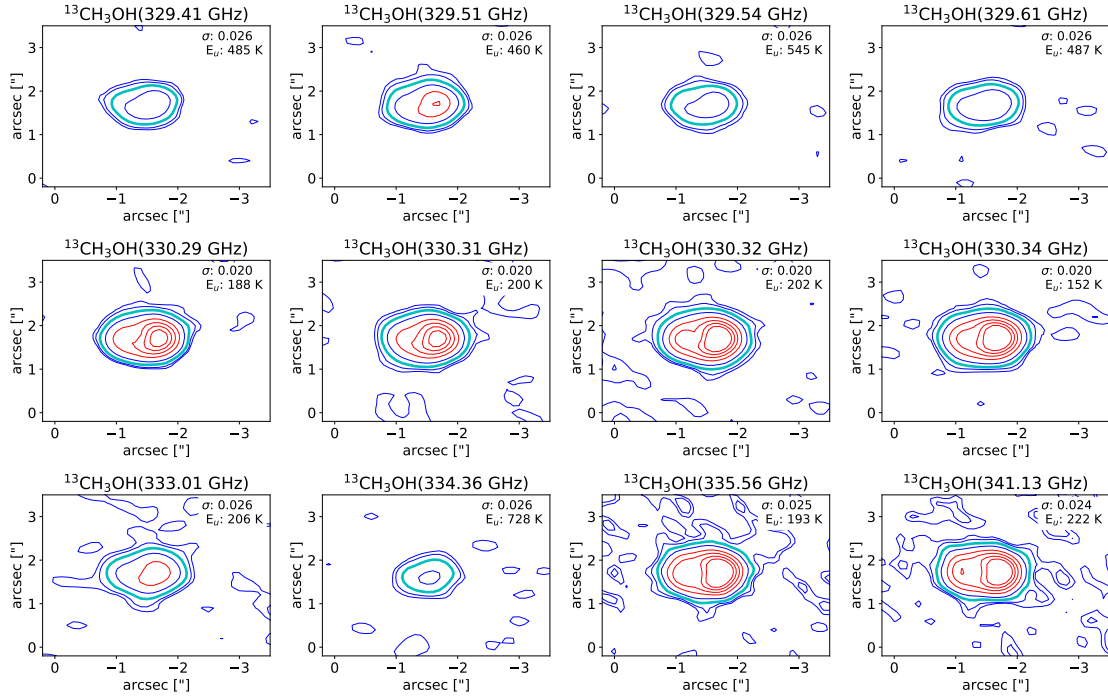


**Figure 11:** A subset of contour maps of  $^{13}\text{CH}_3\text{OH}$  for IRAS16293B. The different levels are for  $3\sigma$ ,  $5\sigma$ ,  $10\sigma$ ,  $20\sigma$ ,  $40\sigma$ ,  $60\sigma$ ,  $80\sigma$ ,  $100\sigma$ , where the  $10\sigma$  contour is in cyan. The upper energy and  $\sigma$  is displayed on the plots.

Contour maps of  $\text{CH}_3\text{OCHO}$ ,  $\text{CH}_3\text{OCH}_3$  and  $\text{C}_2\text{H}_5\text{OH}$  were also made. The structure is similar to those of  $\text{CH}_3\text{CHO}$  for IRAS16293B and is therefore not shown here. All the contour maps for IRAS16293A and IRAS16293B are included in Appendix A.

## 4 Einstein A coefficient and the structure of the molecule

In the previous section we constructed contour maps for different molecules. In the contour maps for IRAS16293B, we saw a feature around  $[-1''; 2'']$  for  $\text{CH}_3\text{CHO}$  (Figure 10). From the contour maps, we thought that the feature might have something to do with the optical depth, i.e. the Einstein A coefficient. Figure 10 shows that the larger the Einstein A coefficient is, the larger and more visible is the feature around  $[-1''; 2'']$ . Furthermore, the larger the Einstein A coefficient is, the larger is the optical depth. In this section, we want to check if our hypothesis is correct, and this is indeed what is happening.

To test our hypothesis, we first want to make sure that the transitions we look at have almost the same upper energy. This is to eliminate any changes in the contour maps that the upper energy might cause. Looking at contour maps from other molecules like  $^{13}\text{CH}_3\text{OH}$  (Figure 11), we can see that the structure of the molecule is not the same as for  $\text{CH}_3\text{CHO}$ , e.g. we do not see the same feature at  $[-1''; 2'']$ . Since we do not have the same structure, we can not include this molecule in this analysis. Furthermore, looking at contour maps for IRAS16293A (Figure 8), the structure is not the same for IRAS16293B. For that reason, this analysis is only done for IRAS16293B, and not all molecules are used. To test the hypothesis, three different molecules are used that all have the same structure. The range for the upper energies for the three different molecules are in Table 1.

From the contour maps of different transitions, we find the ratio between the intensity at the feature around  $[-1''; 2'']$  and the centre around  $[-2''; 2'']$ . To compare the different transitions and molecules, we first normalised each contour map with the maximum intensity. This means that the maximum intensity for each contour map is 1, and the rest is scaled after this. The next thing is to find the ratio between the intensity at the two different positions (the feature and the centre). To find the intensity at the two positions, two boxes of  $0.3'' \times 0.3''$  are constructed around the two positions. Finally, the median intensity from each box is found, and from these two intensities, the ratio is calculated.

In Figure 12 is two different contour plots for  $\text{CH}_3\text{CHO}$  with the two boxes. For each molecule, the boxes are at a fixed position, so even though the molecules size change or the position of the features or centre might slightly change, the boxes are at the same position. The placement of the boxes is chosen to capture the feature and centre as much as possible for all transition. We chose to fix the position of the

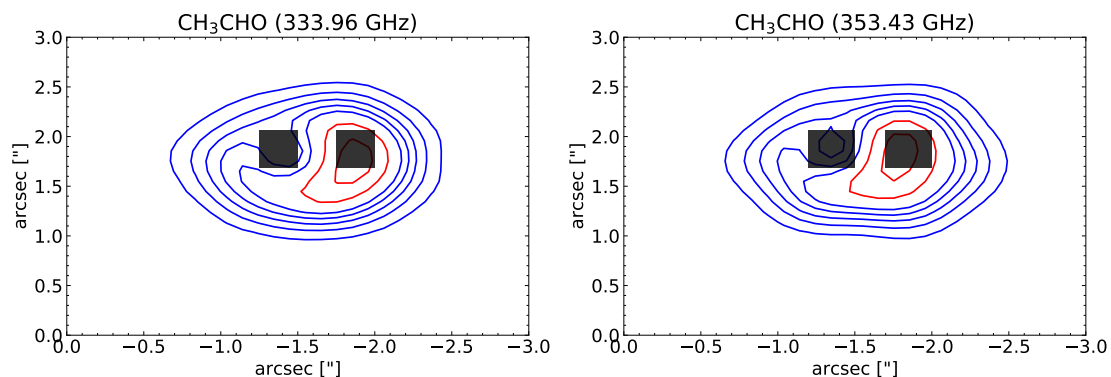


**Figure 12:** Contour maps of two transition of  $\text{CH}_3\text{CHO}$ . These contour maps are normalised, and the different levels are 10%, 20%, 30%, 40%, 50%, 70% and 90% of the maximum intensity.

boxes because we want to compare the ratio at the same position. However, as the

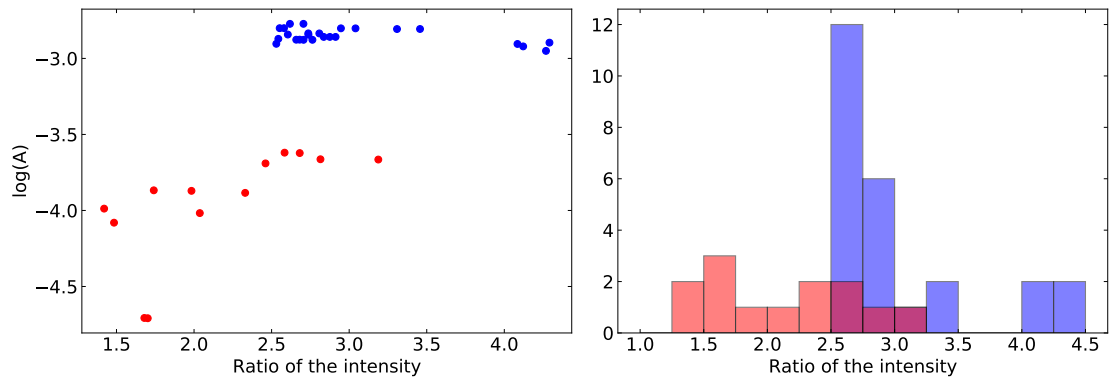
Einstein A coefficient changes, the feature changes as well. We hypothesise that we have a smaller Einstein A coefficient, the feature becomes smaller. This means that the box may not cover the feature entirely for all transitions. Furthermore, the box that is getting the highest intensity in the middle of the molecule may not lay entirely in the middle for all the different transitions.

The position of the boxes can change from molecule to molecule. The change in the position is a maximum of  $0.1''$  in one of four directions. This is much smaller than our beam size of  $0.5''$ . The reason why we need to change the positions is unknown. However, something is different from molecule to molecule since the feature's location is not at the same position for the different molecule. Furthermore, not all molecule have the same structure, which might tell us that something is going on we do not understand yet. This can be seen on the contour maps of  $\text{CH}_3\text{CHO}$  and  $^{13}\text{CH}_3\text{OH}$  for IRAS16293B in Figure 9 and 11 respectively.

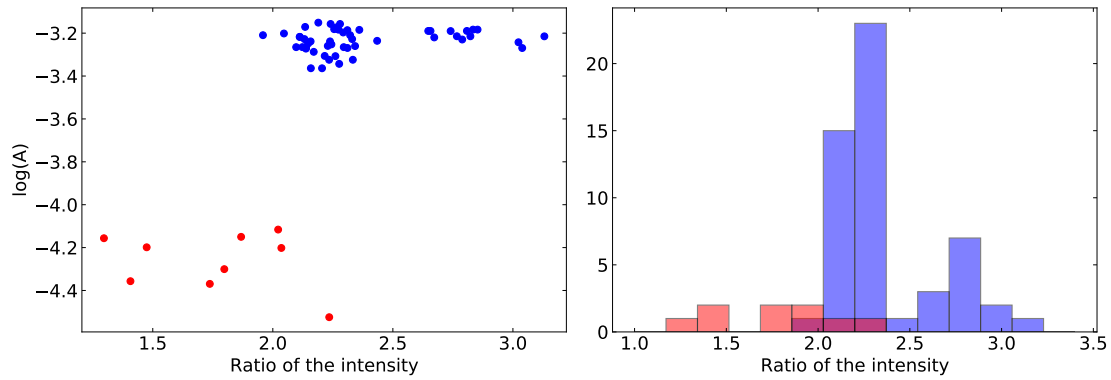
The boxes are the best possible attempt to find the ratio between the feature and the maximum intensity. However, it is possible that another analysis would be better to show the correlation.

When the ratio between the two medians from each box is found, it is plotted in two different ways to show the results best. The first is a scatter plot shown in Figure 13 on the left-hand side for the different molecules. Here it is possible to see a difference in the two medians depending on the Einstein A coefficient. To show this better, three histograms of the ratios are plotted in Figure 13 on the right-hand side. Here the ones with the highest Einstein A coefficient are shown in blue, and they correspond to the blue on the scatter plot. From this, we can see a correlation between the Einstein A coefficient and the feature, and the feature gets more visible if the Einstein A coefficient is larger.

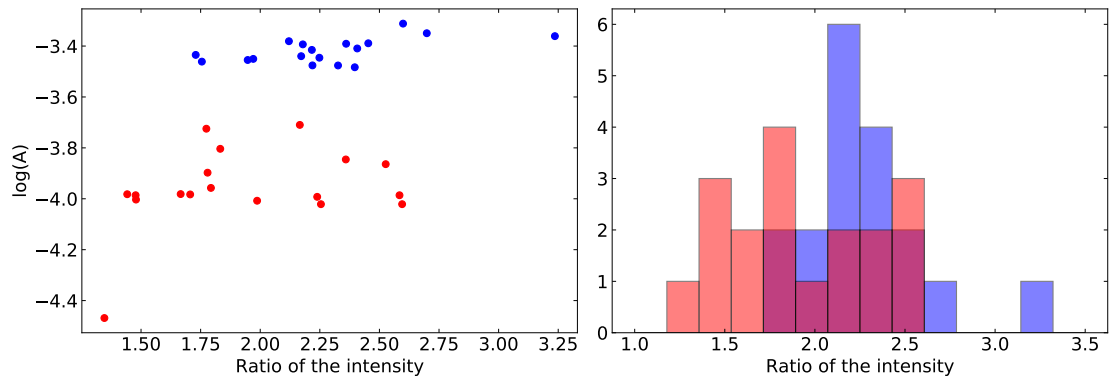
The correlation between the Einstein A coefficient and the feature seen in the contour plot is not clear for all molecules. In Figure 13a and 13b, it is easy to see that there is a correlation. Here we can distinguish the data by the Einstein A coefficient and see a difference in the intensity on the histogram on the right-hand side of the figure. However, when we look at Figure 13c, it is not that easy to distinguish between the different Einstein A coefficients. When we look at the histogram, the two different sections lay on top of each other, and looking at the scatter plot, it is not clear where we needed to separate it. For  $\text{CH}_3\text{CHO}$  and  $\text{CH}_3\text{OCHO}$ , the Einstein A coefficient lies in two different clumps ( $\log(A) \sim -3 \text{ s}^{-1}$  and  $\log(A) \sim -4 \text{ s}^{-1}$ ). This is the reason why it is so easy to separate the data into two sections. We do not see the same separation for  $\text{C}_2\text{H}_5\text{OH}$ , so the histogram does not show the correlation well. It is not 100% clear why we have this separation, but we tried to look at the quantum numbers



(a)  $\text{CH}_3\text{CHO}$



(b)  $\text{CH}_3\text{OCHO}$



(c)  $\text{C}_2\text{H}_5\text{OH}$

**Figure 13:** The ratio between the intensity at the centre and the feature in the contour maps. The red in the scatter plot correspond to the red in the histogram, and the same applies to the blue.



for  $\text{CH}_3\text{CHO}$  and  $\text{CH}_3\text{OCHO}$ . When we have  $\log(A) \sim -3 \text{ s}^{-1}$ , we have that  $J_u - J_l = 1$ , and when  $\log(A) \sim -4 \text{ s}^{-1}$ , we have  $J_u - J_l = 0, 1$  or  $-1$ .

Now that we have looked at three different molecules, it is still not completely clear if our hypothesis is correct or not. To check if there is this correlation between the optical depth, i.e. the Einstein A coefficient and the structure of the molecule, more molecules need to be investigated. We also look at HNC and  $\text{CH}_3\text{CN}$ , two N-bearing COMs, which have the same molecular structure as  $\text{CH}_3\text{CHO}$ . For HNC, we did not have enough transitions within a small energy range where the Einstein A coefficient change significantly to do this analysis. For  $\text{CH}_3\text{CN}$ , the range of the Einstein A coefficient was not large enough to make the analysis. Furthermore, it is unknown if this analysis only applies to IRAS16293B or if this applies to other protostars.

## 5 The upper energy and the extent of the molecular emission

In the previous section, we saw how the optical depth influenced the structure of the molecule. In this section we will look at the extent of the molecular emission and see if there is a correlation with the upper energy. In Figure 8, 9 and 11, the  $10\sigma$  contour is in cyan, and the upper energy is displayed on each contour map. If we look at the cyan contour and compare it with the upper energy, the lower the upper energy is in kelvin, the larger is the extent of the emission from the line. This is our first hypothesis in this section. Our next hypothesis is that from the plot of the upper energy and the radius of the molecular emission, we can get the temperature profile of the envelope, which we talk about in Section 1.2.1.

To test the first hypothesis, we created contour maps of transitions where the Einstein A coefficient was kept almost constant. This is the opposite of what we did in Section 4, where we kept the upper energy constant. We kept the Einstein A coefficient constant, so the only difference for transition to transition is the upper energy. The Einstein A coefficient ranges differ from molecule to molecule, but the ranges are in Table 1.

From the contour maps created, the area where the intensity is equal to or larger than  $10\sigma$  is found. Instead of taking the FWHM of a 2D Gaussian, we used the area inside  $10\sigma$  because there is some structure in the contour maps. When the area inside the  $10\sigma$  is found in arcsec, it is converted into a radius. This is done by assuming that the contour is circular. The radius is then converted from arcsec to AU using the distance to the IRAS16293. Here a distance of 141 pc

(Dzib, S. A. et al., 2018) is used. Furthermore, the uncertainties on the radii are found by finding the radius inside the  $9\sigma$  and  $11\sigma$  contour. Therefore, we have an upper and lower uncertainty. In order to get one uncertainty for each point, the mean of the upper and lower uncertainty is used.

The  $10\sigma$  contour is chosen as the radius that defines the extent of molecular emission. This contour is chosen to avoid the noise at the  $3\sigma$  and  $5\sigma$  contour. We did not use a higher  $\sigma$  contour to avoid any feature at the centre, even when the energy is high. We assume that the emission is spherical when we transform the numbers of pixel to a radius, but on the contour maps, we can see that the emission is not entirely spherical. However, the  $10\sigma$  contour is almost spherical, and the uncertainties would be equal for all transitions, so this would not change the outcome of the analysis.

## 5.1 IRAS16293B

This analysis is first only done for IRAS16293B because the spectra have smaller FWHM than the spectra for IRAS16293A, which help with line confusion. Furthermore, the velocity is constant across the source, making it easier to create contour maps. However, we extended the analysis to include IRAS16293A, and the results for source A are in the next subsection.

Four different molecules were investigated for IRAS16293B, and in Figure 14 is the plot of the radius of the molecular emission as a function of the upper energy. Here it is possible to see a correlation between the upper energy and the extent of the emission from the line, and our first hypothesis is correct. The correlation is not clear for all four molecules, but all of the molecules follow the same pattern. If we look at the lower energies, below 300 K for  $\text{CH}_3\text{CHO}$  and  $^{13}\text{CH}_3\text{OH}$ , below 400 K for  $\text{CH}_3\text{OCHO}$ , and below 150 K for  $\text{CH}_3\text{OCH}_3$ , the transition has almost the same radius no matter what upper energy we look at. If we look above these energies, we have a slope. So below the given energies, the radius is almost constant. When we get above the mention energies, we start having a slope, where the higher the energy is, the smaller the radius of the emission from a line is.

Now that we know that there is a correlation between the upper energy and the radius, we want to test our second hypothesis, which is that the slope of our plot follows the temperature profile for an envelope. A recall to Equation 4 and 5 gives us the temperature profiles:

$$\begin{array}{ll} T \propto r^{-2/(4+\beta)} & \text{Optical thin} \\ T \propto r^{-(1+p)/(4-\beta)} & \text{Optical thick} \end{array}$$

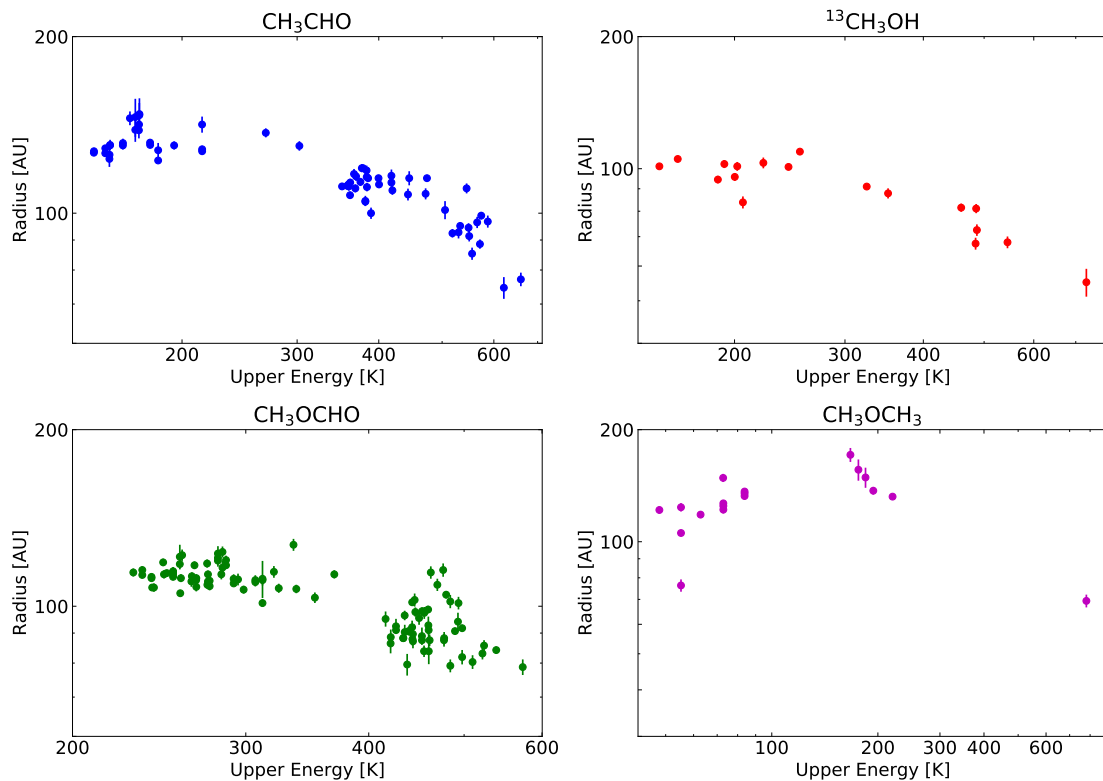


**Figure 14:** The plots of the upper energy and the radius of the molecular emission for IRAS16293B. Here we have the four molecules used in the analysis.

We want to fit the part of our data that have the smallest radii and the largest energies. This is the left side of our plots in Figure 14, where we see the slope. Closest to the protostar, we expect the envelope to be optically thick, so we will fit our data with the temperature profile for an optical thick envelope. If the fit is too steep to match the data, we will look at the temperature profile for an optical thin envelope.

From our plots in Figure 14, we have the radius on the y-axis and the upper energy on the x-axis. Because our error needs to be on the y-axis in order to get the fit to work. So, we need to invert the temperature profile:

$$r = C \cdot E_u^{-(4-\beta)/(1+p)} \quad (13)$$

Where  $C$  is a constant and  $E_u$  is the upper energy in kelvin.  $\beta$  depends on the dust opacity law, and  $p$  depends on the density profile, as mention in Section 1.2.1. For the fit, we use  $\beta = 2$  and  $p = 2$ . This means that we assume that we have a singular isothermal sphere.

Plots of the four different molecules and the fit of the temperature profile for an optical thick envelope is in Figure 15. Here it is important to notice that only the slope is fitted, and the part where the radius is almost constant is left out of the fit. We can see that the data follows the temperature profile for the optically thick part from the fit.

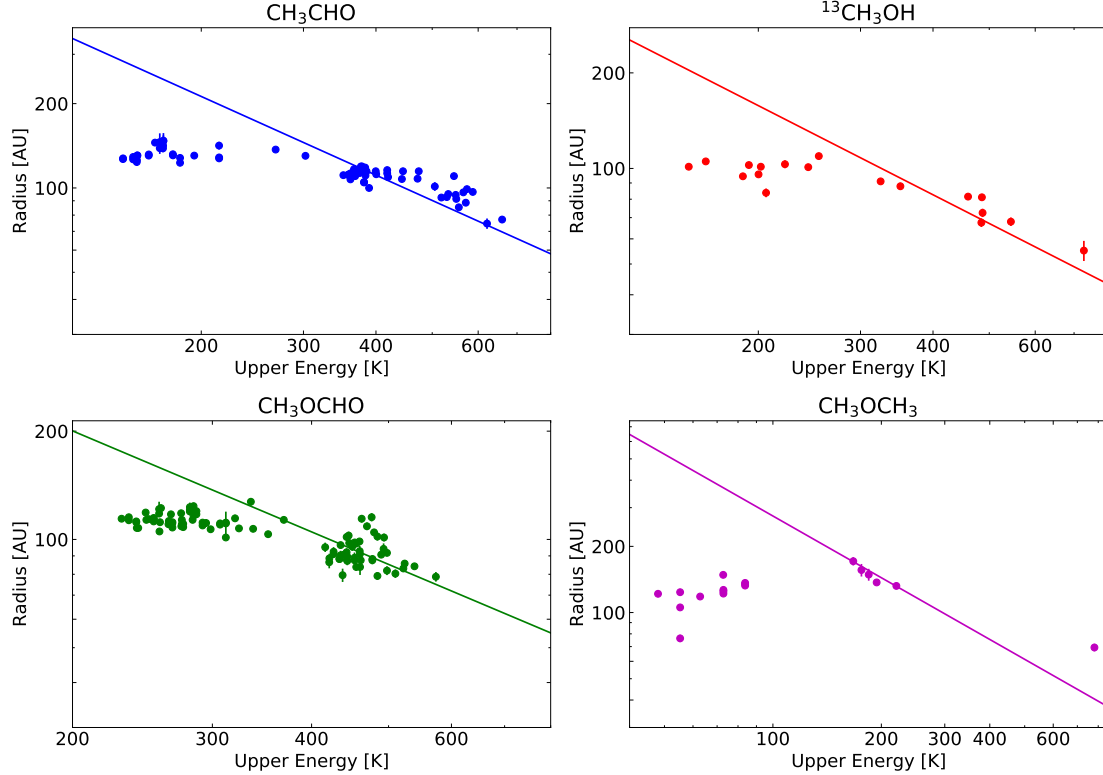


**Figure 15:** The four different molecules and the temperature profile for an optical thick envelope plotted on top for IRAS16293B. When fitted with the temperature profile, only the datapoints with the highest energies, before the slope flattens out, are taking into account.

To see how the temperature profile for the different molecules matches each other, they are all plotted in the same plot. The only variable in the fit is a constant, as we assume that  $p$  and  $\beta$  are the same for all four molecules. However, we do not know if the value we chose for  $p$  and  $\beta$  are the correct ones, so we test this further in Section 6.3. In Figure 16 are the four molecules plotted on top of each other with the fitted temperature profile. From this, we can see a slight difference in the constant for the different molecule, but they lay pretty close together. They may not lay completely on top of each other because of the difference in the abundances. The method we use to find the radius means that the analysis is sensitive to the abundance. However, the slope of the temperature profile will not depend on the abundance.

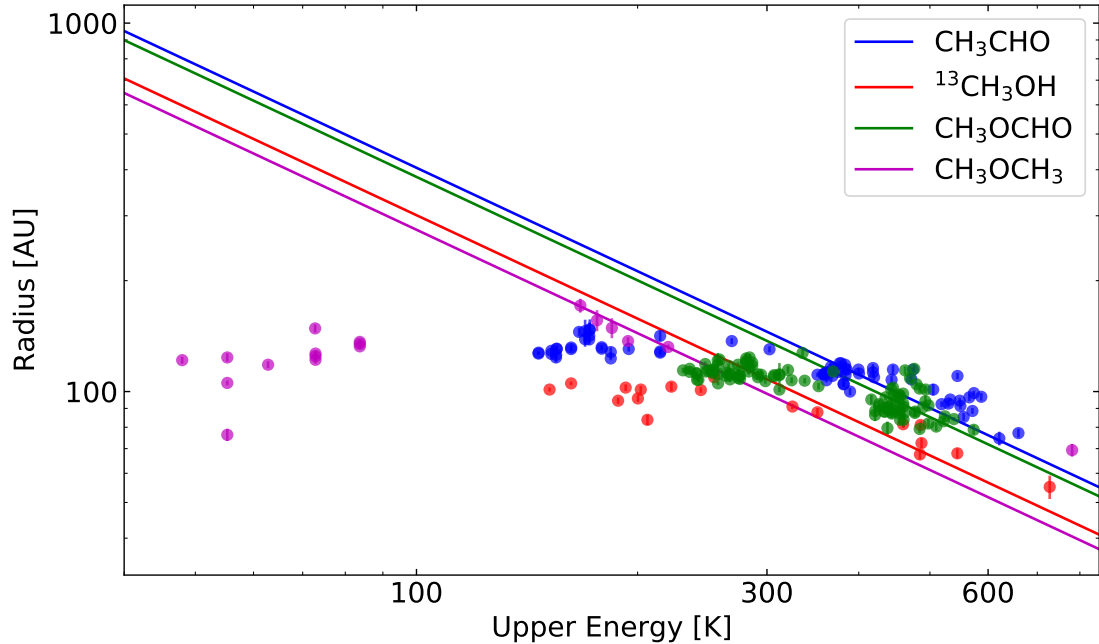


**Figure 16:** The four molecules and their fitted temperature profile from Figure 15 plotted together to show how the different molecules and temperature profiles compare.

## 5.2 IRAS16293A

Now that we have done the analysis for IRAS16293B and found out that both our hypotheses are correct, we wanted to test if the same applies to other protostars. Therefore we did the same analysis for IRAS16293A.

For IRAS16293A, we only used CH<sub>3</sub>CHO, CH<sub>3</sub>OCHO and CH<sub>3</sub>OCH<sub>3</sub>. The reason why we did not use <sup>13</sup>CH<sub>3</sub>OH is that it is too optically thick, just like CH<sub>3</sub>OH is. When we say that the emission for a molecule is too optically thick, the emission from those molecules is only from the outer part of the envelope, as mention in Section 1.3. This means that we would not be able to use them in this analysis since they all would have the same radius no matter the energy. Besides that, we analysed three molecules, and the same analysis is done for IRAS16293A as for IRAS16293B. The line towards IRAS16293A is much broader than towards IRAS16293B. Jørgensen et al. (2016) found that in IRAS16293B, there is approximately one line per 3 km s<sup>-1</sup>, for IRAS16293A we know that the FWHM for a line is  $\sim 2 - 3$  km s<sup>-1</sup>, meaning that we would not have one line per 3 km s<sup>-1</sup> but fewer. This means that we will have fewer emission lines for each molecule. However, it is still possible to make the analysis.

In Figure 17 is the three molecules and the fit of the temperature profile. As

for IRAS16293B, only the highest energies were fitted because the data flatten out at lower energies. We will talk more about this in the following subsection. Again, it is possible to see the correlation, and it is possible to see that the correlation match the optically thick part of an envelope.

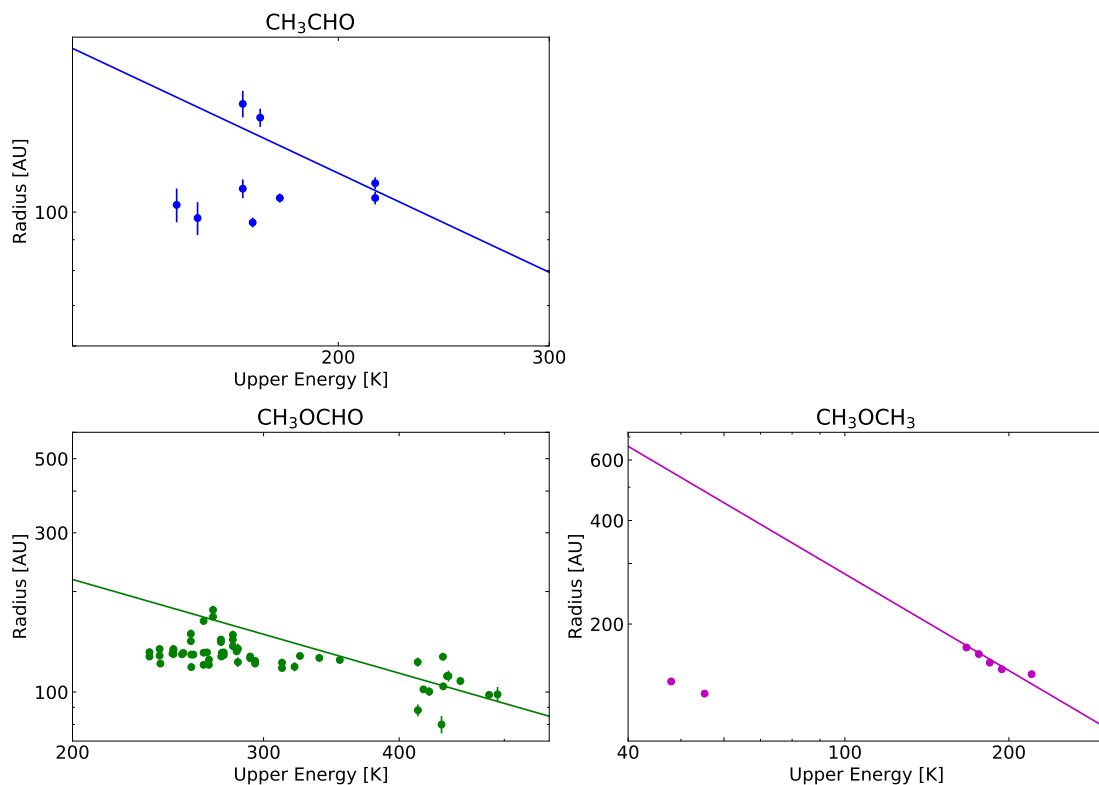


**Figure 17:** The three different molecules and the temperature profile for an optical thick envelope plotted on top for IRAS16293A. When fitted with the temperature profile, only the datapoints with the highest energies are taking into account.

To see how the different molecules look compared to each other, the three molecules are plotted in the same plot. This plot is in Figure 18. Here we again see that the fitted line does not have the same constant. However, all of the molecules lay close together. Again, one reason for this can be the difference in the abundance of the different molecules.

### 5.3 Comparing IRAS16293A and IRAS16293B

In Figure 15 and 17, not all points follow the same trends. However, all points have been checked by looking at both the emission line and the contour maps. This ensures that they do not suffer from issues, e.g. due to contamination by

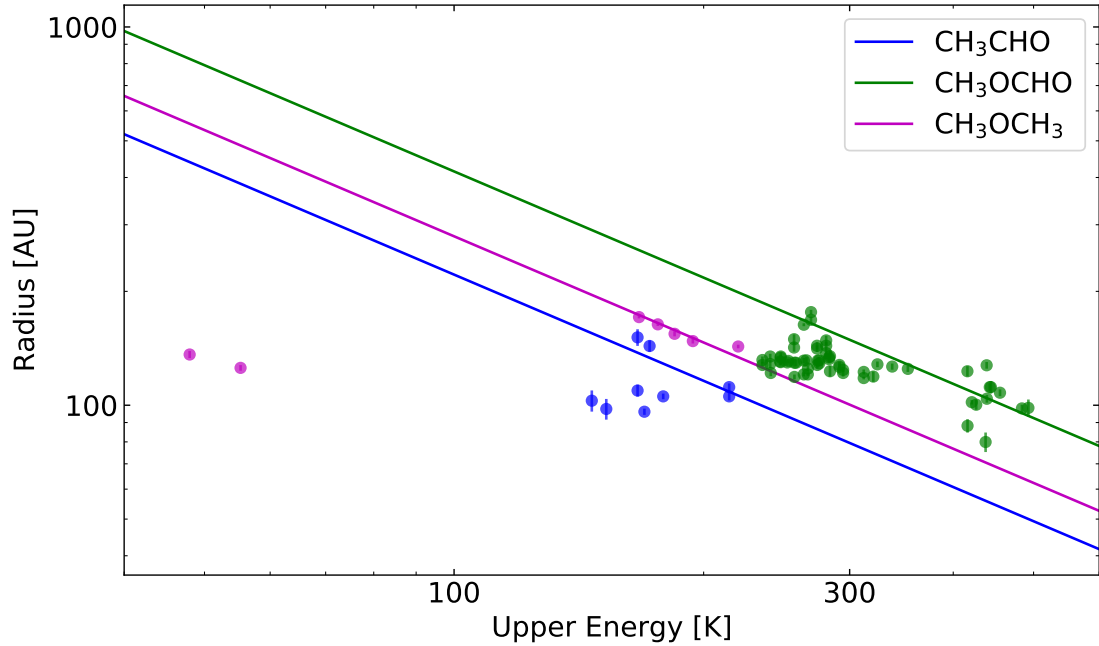


**Figure 18:** The three molecules and their fitted temperature profile from Figure 17 plotted together to show how the different molecules and temperature profiles compare.

other species or instrumental problems. This is all done to ensure that the points lying outside of the trend are the right molecule.

Looking at the different molecules in Figure 15 and 17, it looks like at higher energy, we have a slope, which matches the temperature profile for optical thick emission. However, at lower energies, we see that the data flattens out and does not match the temperature profile. This is why we decided only to use the part with the highest energy to fit the temperature profile to. We know that at higher energies and smaller radii, the envelope is optically thick. Further out, we would expect the envelope to be optically thin, where we have lower energies and, therefore, higher radii. The data does not go that far out, and therefore we do not see this optical thin envelope, so we can not test this. In between the optically thick and thin envelope, we would have a combination between these two, and this might be why we see the data flattens out at some point. The data is going from purely optical thick to have a combination of optical thin and thick. We will come back to this in Section 6, where we try to recreate the data using radiative transfer simulation to test if we see the same structure. Another thing that might happen is that we only trace the hot corino; thus, the flattening out, at the maximum radius, perhaps reflect the outer radius where the molecules are in the gas phase.

Looking at the fit of the temperature profiles in Figure 15 and 17, the temperature profiles are normalised differently. One reason for this could be that the luminosities for IRAS16293A and IRAS16293B are not the same. The luminosity for IRAS16293 is found to be  $21L_{\odot}$  and Jacobsen et al. (2018) found a luminosity for IRAS16293A of  $\sim 18L_{\odot}$  and a luminosity for IRAS16293B of  $\sim 3L_{\odot}$  from 3D modelling. Because of the difference in the luminosity, we would expect to see a difference in the temperature profiles. We would expect that the temperature profile for IRAS16293A would have a higher constant because the source is more luminous and therefore have a higher temperature further out. To check if this is what we see from the different molecules, the same molecule from the two different sources are plotted together. This is in Figure 19, where the three molecules used in both analyses are plotted together. For both  $\text{CH}_3\text{OCHO}$  and  $\text{CH}_3\text{OCH}_3$ , the data and the line for IRAS16293A are higher than those for IRAS16293B, meaning that the radius is larger for IRAS16293A when we have the same upper energy. This is what we would expect since IRAS16293A has a higher luminosity. However, for  $\text{CH}_3\text{CHO}$ , the line and data for IRAS16293B are the highest, so the radius is larger for IRAS16293B when we have the same upper energy. Looking at the different transition for  $\text{CH}_3\text{CHO}$  for IRAS16293A, they are less smooth than the other molecules. In Figure 7 is a transition for  $\text{CH}_3\text{CHO}$ . To the left in the figure, we have the transition for IRAS16293A, and it is possible to see that the emission peak is not as smooth for IRAS16293A as for IRAS16293B, which is on the right-hand side of the figure. One reason for this can be that there is noise in the spectra for IRAS16293A. Another reason can be that we have line confusion with transitions from a different molecule. Another reason why the data and line of IRAS16293A are below IRAS16293B could be the difference in the abundance. We do not yet know how the abundance changes this analysis, but we will look into that in Section 6.4.

To see the difference between the two sources, the ratio between the two lines are found. This is done by dividing the line for IRAS16293A with the line for IRAS16293B. From this, we get the following:

$$\begin{aligned} \text{CH}_3\text{CHO} &: 0.65 \pm 0.01 \\ \text{CH}_3\text{OCHO} &: 1.11 \pm 0.01 \\ \text{CH}_3\text{OCH}_3 &: 1.06 \pm 0.01 \end{aligned}$$

The uncertainty is calculated using error propagation, where the uncertainty used in the error propagation comes from the constant in the temperature profile. The errors on the plots of the energy and radius are small, and therefore the uncertainty of the constant often becomes small. We have almost the same ratio for  $\text{CH}_3\text{OCHO}$  and  $\text{CH}_3\text{OCH}_3$ , but for  $\text{CH}_3\text{CHO}$  we have a much smaller ratio. This matches what we see in Figure 19, where for  $\text{CH}_3\text{OCHO}$  and  $\text{CH}_3\text{OCH}_3$ , the radii



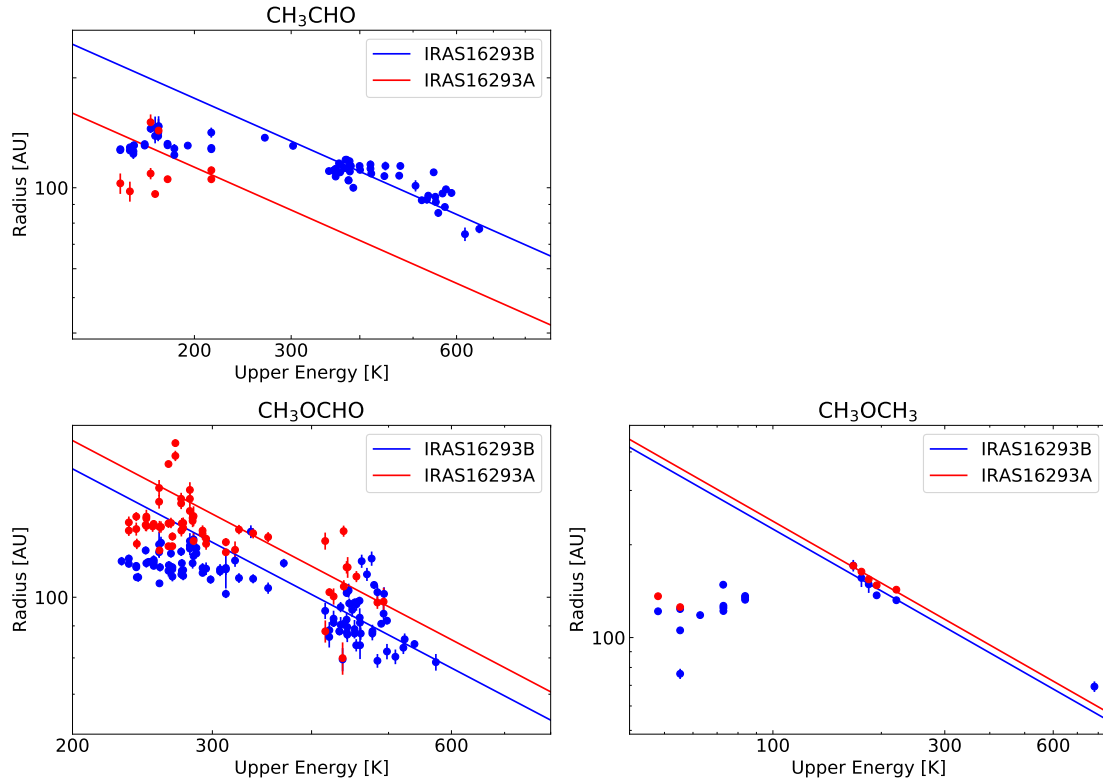


**Figure 19:** The three molecules used in both analysis plotted together with the temperature profile for an optical thick envelope. Only the datapoints with the highest energy are taking into account. These plots are a combination of Figure 15 and 17. We have  $p = 2$  and  $\beta = 2$ .

for IRAS16283A is larger than for IRAS16293B when we have the same upper energy and for CH<sub>3</sub>CHO we have the opposite.

From this section, we can conclude that there is a correlation between the upper energy and the extent of the molecular emission. This correlation can be represented but the temperature profile of an optical thick envelope at the highest energies; the empirical temperature profile. Furthermore, we have discussed why we see the slope for the upper energy and radius flattens out, but we will also look at this further in the next section about radiative transfer simulation. Lastly, we look at how the data from IRAS16293A compared to the data from IRAS16293B. This will be looked at again in Section 6.4.

## 6 Radiative transfer

The last part of the analyses in this project, it the analyses done with the radiative transfer simulation. We performed multiple analyses to investigate the temperature profile and see if we can reproduce the results from in Section 5. First, we will look at the temperature profile. We get this profile for the dust radiative transfer code *Transphere*, which is the code we run before using the line radiative transfer code *Ratran*. We will look at which parameters change the temperature profile and look at the temperature profile of the envelope for the system we are doing radiative transfer code on (a system as close to IRAS16293B as possible). When this is done, *Ratran* will be used to recreate the data and analysis from Section 5. Finally, we will explore what happens with the empirical temperature profile (the profile of the upper energy and radius) and temperature profile if we change the luminosity.

### 6.1 The temperature profile

As described in Section 1.5.2, we need to solve the dust radiative transfer problem before solving the line radiative transfer. To solve this problem, we use a separate code called *Transphere*. For *Transphere* to work, it needs different parameters to solve how the dust changes the radiation from the protostar throughout the envelope. From the *Transphere* code, we get an output file where the temperature profile of the envelope is included.

In Table 2 is the different input parameters *Transphere* need to construct a system as close to IRAS16293B. The parameters come from Schöier et al. (2002) and Jacobsen et al. (2018). Here it is important to notices that we assume that the density profile follows a power-law:

$$\rho = \rho_0 \left( \frac{r}{r_0} \right)^p$$

Here we have  $p$  is the same as used in the temperature profile described in Section 1.2.1.

For the first part of the temperature profile analysis, we want to see how different parameters change the temperature profile. To investigate this, we change two input parameters. The two parameters we change is the power-law for  $\rho$ , and the density at the reference radius  $\rho_0$  and in Table 3 is the different changes.

In Figure 20 is the plot of the temperature profiles for the different models. It is important to say that the temperature profile in yellow has an inner radius at 10 AU, so it starts further out. From this figure, we can see that the most significant impact on the temperature profile is the density. The power-law index changes the

**Table 2:** The parameters used in the set-up of radiative transfer simulation to resemble IRAS16293B.

Parameter	Description	Value
$L_B$	Stellar luminosity	$3 L_\odot$
$T$	Stellar temperature	1000 K
$r_{in}$	Inner radius of shell	1 AU
$r_{out}$	Outer radius of shell	$2 \cdot 10^3$ AU
$r_0$	Reference radius	1 AU
$\rho_0$	Density at reference radius	$3.4 \cdot 10^{-12}$ g cm $^{-3}$
$p$	Power-law for rho	-1.7
$d$	Distance in pc	141 pc
[CH <sub>3</sub> OH], $T > 90$ K	Abundance	$10^{-7}$
[CH <sub>3</sub> OH], $T < 90$ K	Abundance	$10^{-9}$
[CH <sub>3</sub> CHO], $T > 90$ K	Abundance	$1.2 \cdot 10^{-9}$
[CH <sub>3</sub> CHO], $T < 90$ K	Abundance	$1.2 \cdot 10^{-11}$
[CH <sub>3</sub> OCHO], $T > 90$ K	Abundance	$2.6 \cdot 10^{-9}$
[CH <sub>3</sub> OOHO], $T < 90$ K	Abundance	$2.6 \cdot 10^{-11}$

**Table 3:** The different parameters that change in the investigation of the temperature profile.

Density at the reference radius [g cm $^{-3}$ ]	Power-law index	$r_{in}$ [AU]
$2.5 \cdot 10^{-12}$	1.7	1
$2.5 \cdot 10^{-12}$	1.5	1
$2.5 \cdot 10^{-14}$	1.7	1
$2.5 \cdot 10^{-14}$	1.5	1
$2.5 \cdot 10^{-12}$	1.7	10

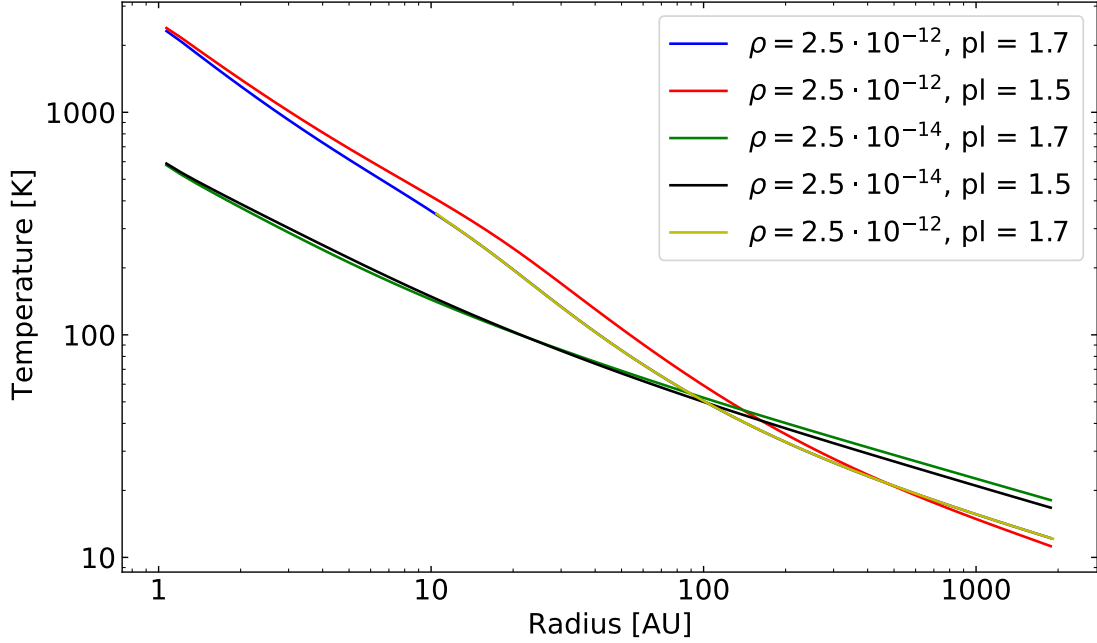


**Figure 20:** The temperature profile for the different dust radiative transfer models in Table 3. This shows how a different density and power-law index change the temperature profile. Furthermore, in yellow,  $r_{in} = 10$  AU, where the others have  $r_{in} = 1$  AU, this is why the yellow line starts at a larger radius.

temperature profile slightly, but not as much as the density does. Furthermore, we know that dust evaporates when the temperature is above 1500 K, which means that it does not make sense to look at the innermost part of the temperature profile because the dust has evaporated.

We now know that the most significant impact on the temperature profile is the density. So we want to see if the temperature profile follows the predicted temperature profile from Equation 4 and 5 where we have that the inner region is optically thick, and the outer region is optically thin.

In Figure 21, is the temperature profile created with the parameters in Table 2. The molecule and the abundance are not yet included since they are not needed for *Transphere* to work. This profile is fitted with a temperature profile for an optical thin and thick envelope, found in Equation 4 and 5. For the fitted temperature profile, we use difference  $p$  and  $\beta$  than we used in the analysis for the observed data in Section 5. When the *Transphere* codes solve the dust radiative transfer, it needs some dust properties, e.g. the opacity, from which it is possible to find  $\beta$ . Furthermore, we also gave it a density dependency, which is  $p$ . In Table 2, we can see that the power-law for  $\rho$  we used to run *Transphere* is 1.7, so when we fit

the temperature profile, we use  $p = 1.7$ . For  $\beta$ , we can find this from the opacity model that we use. We used a dust opacity model OH5, which is for thin ice. From this model, we can plot  $\kappa_\nu$  as a function of frequency, and from this, we can fit the slope of the plot. We have  $\kappa_\nu \propto \nu^\beta$  and from this, we get:

$$\beta = 1.48$$

So when we fit the temperature profile from *Transphere* with the theoretical ones for an optical thin and thick envelope, we use  $p = 1.7$  and  $\beta = 1.48$ .

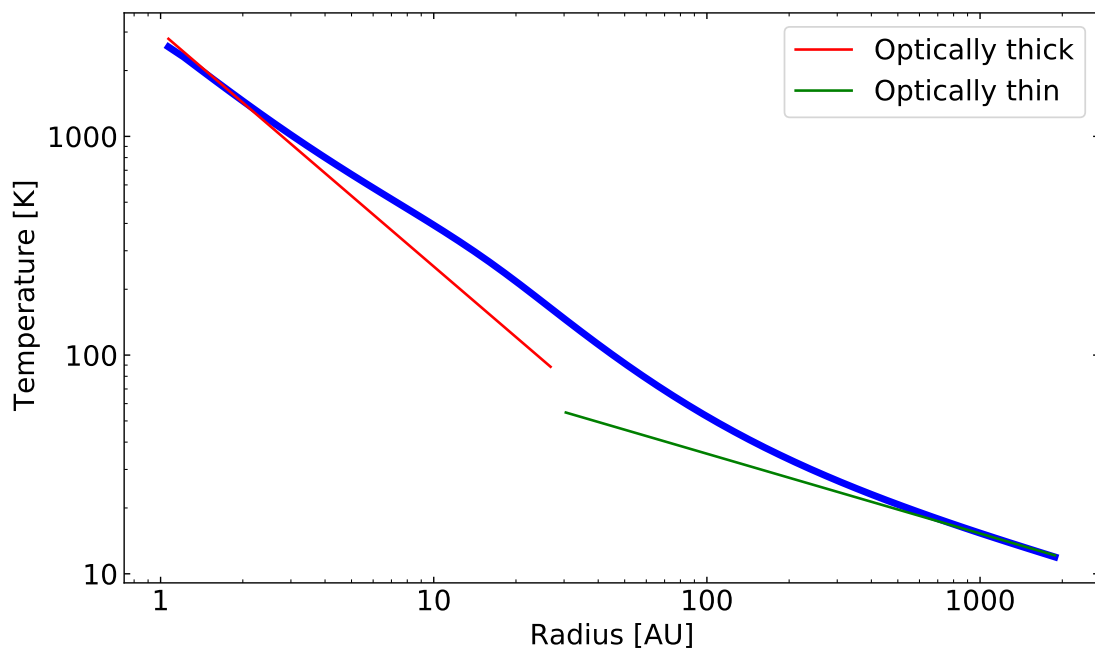


**Figure 21:** Temperature profile for the dust radiative transfer simulation plotted with the temperature profile for an optical thin and thick envelope.

From Figure 21, it is possible to see that the inner part of the envelope is optically thick, and the outer part is optically thin. In the middle of the envelope, we cannot match the temperature profile, which means that the envelope does not go from being optical thick in the centre to suddenly being optical thin further out. Instead, it is a process where it happens over the middle of the envelope.

## 6.2 The empirical temperature profile

In the last section, we looked at the temperature profile, and now we want to see if we can recreate the observed data with the radiative transfer simulation. We want to use the same molecules used in the analysis in Section 5 for the best comparison.

The only molecule, out of the ones used in the empirical temperature profile in Section 5, where the collisional rate coefficients are known is CH<sub>3</sub>OH. This means that we will first try to recreate the data for CH<sub>3</sub>OH.

From Figure 6, we can see that to use *Ratran*, we need to use *Transphere* first. First, we ran *Transphere* with the parameters from Table 2. From this, we get the temperature profile seen in Figure 21. In order to run *Ratran*, we need the abundance of the molecule. For the abundance of the molecule, two different abundance is used based on the temperature. This is because when we have grain-surface chemistry, molecule sublimates from the grain at a specific temperature. Schöier et al. (2002) describe how they found that a jump model works best for CH<sub>3</sub>OH, and they found the temperature of 90 K for the jump. So, if we have a temperature below 90 K, the amount of CH<sub>3</sub>OH in the gas phase is lower because CH<sub>3</sub>OH is stuck to the grain. However, if we are above 90 K, CH<sub>3</sub>OH has evaporated from the grain and is detectable in the gas phase. In Table 4 is the different abundance. For CH<sub>3</sub>OH, we have used the typical abundance. Later, when we try to recreate the data for CH<sub>3</sub>CHO and CH<sub>3</sub>OCHO, the column densities of the molecules were reported in Jørgensen et al. (2018), and are used to calculate the fractional abundance of each species with respect to CH<sub>3</sub>OH.

**Table 4:** The abundance use for the radiative transfer simulation of IRAS16293B.

Molecule	Abundance
[CH <sub>3</sub> OH], $T > 90\text{K}$	$10^{-7}$
[CH <sub>3</sub> OH], $T < 90\text{K}$	$10^{-9}$
[CH <sub>3</sub> CHO], $T > 90\text{K}$	$1.2 \cdot 10^{-9}$
[CH <sub>3</sub> CHO], $T < 90\text{K}$	$1.2 \cdot 10^{-11}$
[CH <sub>3</sub> OCHO], $T > 90\text{K}$	$2.6 \cdot 10^{-9}$
[CH <sub>3</sub> OOHO], $T < 90\text{K}$	$2.6 \cdot 10^{-11}$

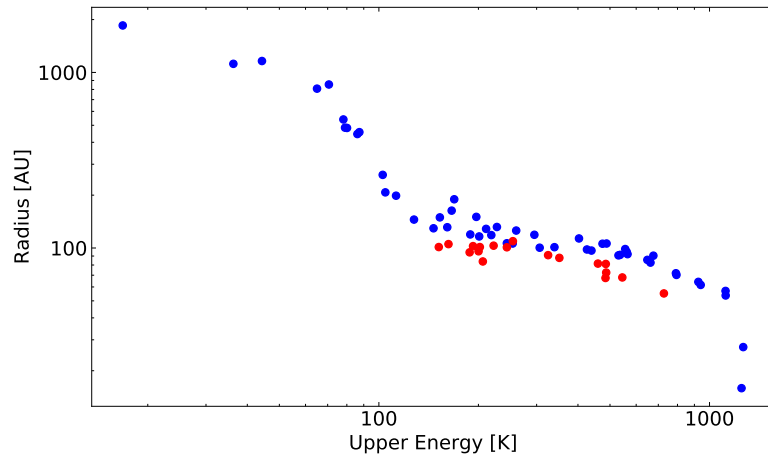
With all the input parameters, we can run *Ratran*. From *Ratran*, each FITS file represents a datacube for each simulated molecular transition. With the data, we first add noise. We want to have the same RMS as we have in the observed data from PILS for the noise. This is about  $7 - 10 \text{ mJy beam}^{-1} \text{ channel}^{-1}$ . This is done by adding random numbers to each pixel, so we have an RMS inside this range. Besides this, the data needs to be convolved to resemble the data from PILS as much as possible. The data is convolved with a 2D gaussian that each has a beam side of  $0.5''$ . When all of this is done, the emission peak is then integrated over to create a contour map, just like we did for the observed data. The radiative transfer data have an FWHM of  $1 \text{ km s}^{-1}$ , which is the same as the data from IRAS16293B. When the contour maps are created, the area inside  $10\sigma$  is found.

We then plot this to see if we have the same correlation between the extent of the molecular emission and the upper energy.

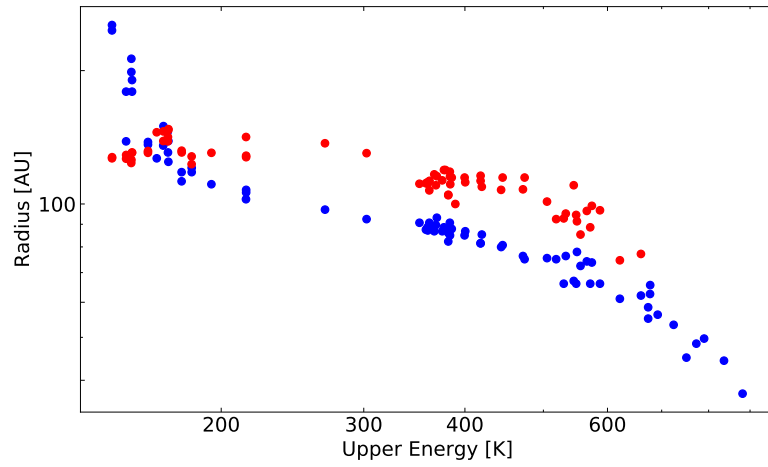
Before we look at the radiative transfer data for  $\text{CH}_3\text{OH}$ , we will recreate the data from  $\text{CH}_3\text{CHO}$  and  $\text{CH}_3\text{OCHO}$ . Because we do not have the collisional rate coefficients for these molecules, we could not use *Ratran* to create the level populations. So we need to create the level populations ourselves and then used the second part of *Ratran* (*sky*), i.e. the ray tracing part, to calculate the synthetic images for the molecules and their emission lines.

To construct the level populations files, we use the catalogues from JPL again. Some of the transition inside the PILS data frequency range is used, mainly the ones that are used in the energy and extent analysis. These transitions are transformed into a molecular file in the same format that *Ratran* uses. Besides that, we rerun *Transphere* to add the new abundance into the source file, which we use to create the level populations with. We still use a jump model, but the abundance is lower for  $\text{CH}_3\text{CHO}$  and  $\text{CH}_3\text{OCHO}$  and is in Table 4. With the source file, it is possible to calculate the level populations if we assume LTE. This is the main difference between the level populations we make ourselves and the ones *Ratran* makes. If we assume LTE, we can use the Boltzmann distribution from Equation 12. We can find the level populations of the different transitions we use and create a population file with the same format as the one *Ratran* produce. When the level population file is produced, the last part of *Ratran* (*sky*) creates the synthetic images.

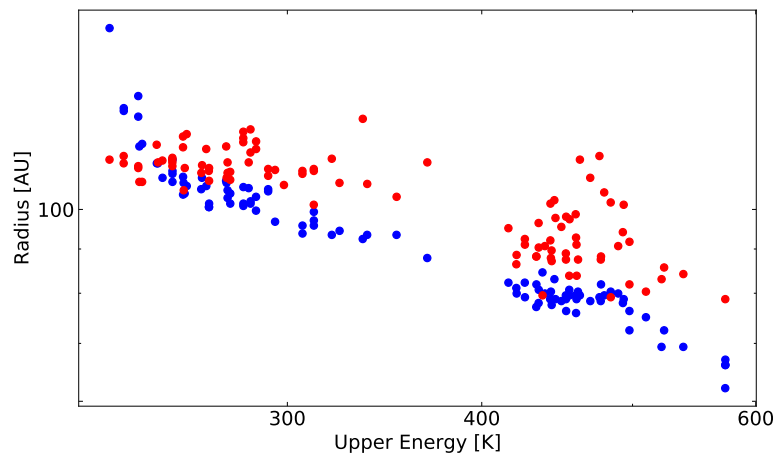
The radiative transfer data and the observed data from PILS are plotted together. This is done for three different COMs,  $\text{CH}_3\text{CHO}$ ,  $\text{CH}_3\text{OH}$  and  $\text{CH}_3\text{OCHO}$ . For  $\text{CH}_3\text{OH}$ , the radiative transfer simulation is based on  $\text{CH}_3\text{OH}$ , and the PILS data is for  $^{13}\text{CH}_3\text{OH}$ . In Figure 22 is the radiative transfer data and the PILS data together. Looking at  $\text{CH}_3\text{OH}$  in Figure 22a, we can see that the PILS data lay just below the radiative transfer data from *Ratran*, so the radii for the *Ratran* data are larger than those for the observed data. However, the difference is so small that the scatter between individual points is larger than the difference between the observed and modelled profiles. Therefore, we can say that the *Ratran* data reproduce the PILS data well. When we look at the data for  $\text{CH}_3\text{CHO}$  in Figure 22b, we can see that the observed data lies above the *Ratran* data for energies higher than 200 K, meaning that the PILS data have larger radii than the *Ratran* data with the same upper energy. One of the reasons for this can be that the luminosity we use on  $3 L_\odot$  is too low or that the abundance for  $\text{CH}_3\text{CHO}$  when making the source file was too low. However, looking at the shape of the data at higher energies, they look alike. At lower energies, below 200 K and larger radii,



(a) CH<sub>3</sub>OH



(b) CH<sub>3</sub>CHO



(c) CH<sub>3</sub>OCHO

**Figure 22:** The *Ratran* data in blue and the observed data from PILS in red to show how they compare.



the PILS data starts to flatten out, while the *Ratran* data continue to increase in radius. For CH<sub>3</sub>OCHO, we have almost the same as for CH<sub>3</sub>CHO. The plot for CH<sub>3</sub>OCHO is in Figure 22c. Here we can see that we again have that the PILS data lies above the *Ratran* data for energies larger than 300 K, and at lower energies, the PILS data flattens out while the *Ratran* data keep increasing in radius. One more thing that is noticeable for the CH<sub>3</sub>OCHO data is if we look at the end with the higher energies, around 480 K, we see that the scattering of the PILS data is quite large compared to the scattering of the *Ratran* data. It looks like six points do not belong. However, looking at the spectra for the transitions and contour plots of these points, they look fine, and no other transitions could be confused with the emission line.

For CH<sub>3</sub>CHO and CH<sub>3</sub>OCHO, we see that when the PILS data flattens out at an energy below 400 K, the *Ratran* data does not. This does not happen for CH<sub>3</sub>OH, so this could be because we assumed LTE to make the population file for CH<sub>3</sub>CHO and CH<sub>3</sub>OCHO. For CH<sub>3</sub>OH, we do not assume LTE because *Ratran* uses the collisional rate coefficient, and when we constructed the population file, we use the Boltzmann distribution. Therefore, we do not know if the whole system is in LTE. The system is most likely in LTE at smaller radii because the density is the highest closest to the protostar. At a point, the system must go from LTE to non-LTE.

In order to investigate this, a population file made with Boltzmann distribution for CH<sub>3</sub>OH is created. This is done so we can compare the population file *Ratran* make with the population file we make. The two different population files are then compared to see when we have a change in the level populations. To see when we have a change in the level populations, the RMS of the populations are found. This means that we find the difference in the two populations files and take the RMS of it. From this, we can see when the two files do not compare anymore. The plot of the RMS and the density of H<sub>2</sub> is in Figure 23 on the left-hand side. We can see that around an RMS on 10<sup>-4</sup>, things start to change. This gives us a density of 10<sup>9</sup> cm<sup>-3</sup>. When we ran the radiative transfer simulation, we chose a minimum population to optimise the coding time. The minimum population was 10<sup>-3</sup> cm<sup>-3</sup>, and if we look at a RMS of 10<sup>-3</sup>, we get a  $N_{H_2} \sim 5 \cdot 10^7$  cm<sup>-3</sup>. We can say that at a density around 10<sup>7</sup> – 10<sup>9</sup> cm<sup>-3</sup>, we do not have LTE anymore.

Another way to investigate when we no longer have LTE is to look at the critical density.

$$n_{crit} = \frac{A_{ul}}{C_{ul}}$$

Here we need the collisional rate coefficient at a specific temperature and the Einstein A coefficient for the same transition. For CH<sub>3</sub>OH, all of this information is in the molecular file *Ratran* uses. In Figure 23 on the right-hand side, the critical

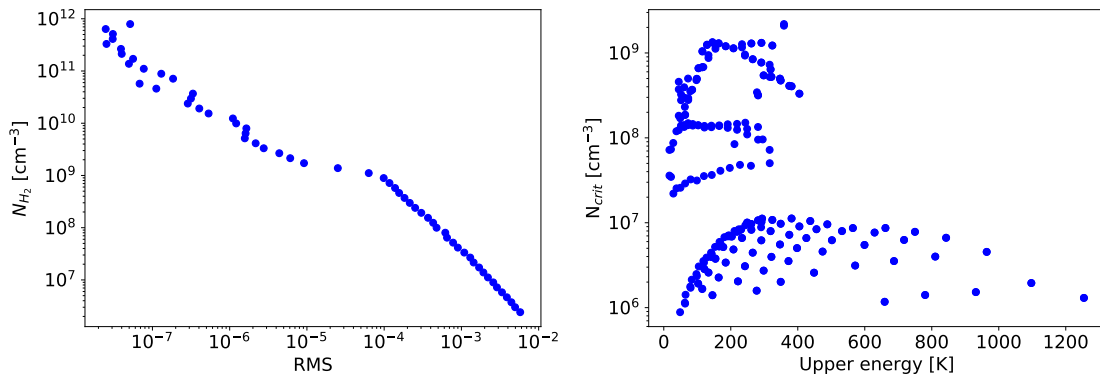


**Figure 23:** To the left is the density of  $\text{H}_2$  as a function of the RMS, and to the right is the critical density as a function of the upper energy. The critical density is calculated using the collisional rate coefficient at a temperature of 100 K.

density is plotted as a function of the upper energy, where we used the collisional rate coefficient at 100 K. Here we used the same frequency range as we used in the radiative transfer analysis of  $\text{CH}_3\text{OH}$ , and we used a lower limit on the Einstein A coefficient of  $\log(A) > -4 \text{ s}^{-1}$ . From the figure, it is possible to see that our critical density is between  $10^6 - 10^9 \text{ cm}^{-3}$ , which is consistent with the range we got from the analysis of the RMS and the density of  $\text{H}_2$ .

Now that we have the density of which we no longer can assume LTE, we transform this density into a radius by looking at the source file. In this file, we have den density for each shell, and we can then find the radius of this shell and find out at what radius we no longer have LTE. If we use the highest density, we get a lower limit for the radius, and if we use a lower density, we get a higher limit for the radius. From the source file, we find that at a radius of  $\sim 70 \text{ AU}$ , we have a density of  $\sim 7 \cdot 10^8 \text{ cm}^{-3}$ . This can be used as a higher limit for the density and thereby a lower limit for the radius. So we no longer have LTE at a radius of  $\sim 70 \text{ AU}$ . Looking at Figure 22b and 22c, we can see that it is around 100 AU that the PILS data and the *Ratran* data no longer follow each other. This match well with the radius where we found out that we no longer have LTE. This means that the data might not follow each other at lower energies because we have assumed LTE when there is no LTE.

Looking at the radiative transfer data for  $\text{CH}_3\text{OH}$  in Figure 22a, if we look at the data with the highest energy (above 1000 K), the last few datapoints do not follow the same trend as the rest. The slope of the data becomes very steep in the end. However, the data for  $\text{CH}_3\text{OH}$  did not look like that when we first used the radiative transfer code. In Figure 24 on the left-hand side is the original data from *Ratran*. Here we have the same number of pixels for each transition and the same

size in arcsec. On the plot, something is going on at the large radius, and looking at the contour plots, we can see that the image is not large enough. To fix this, we took the transitions with the lowest energy and doubled the amount of pixels but kept the size in arcsec the same. On the right-hand side of Figure 24, this has been done, and here we can see that we no longer have a maximum radius. In order to make sure nothing is happening for the other transitions and especially the ones with the highest energy, we again double the number of pixels, but we also change the size in arcsec to half of what it was before. This means that we will end up with an image with the same extent but twice as many pixels. When this is done, it only changes the data with energies higher than 1000 K. We get the steep slope that we also saw in Figure 22a, and this is also in Figure 24 on the right-hand side. In order to see what this could be, we change the beam size that we convolve

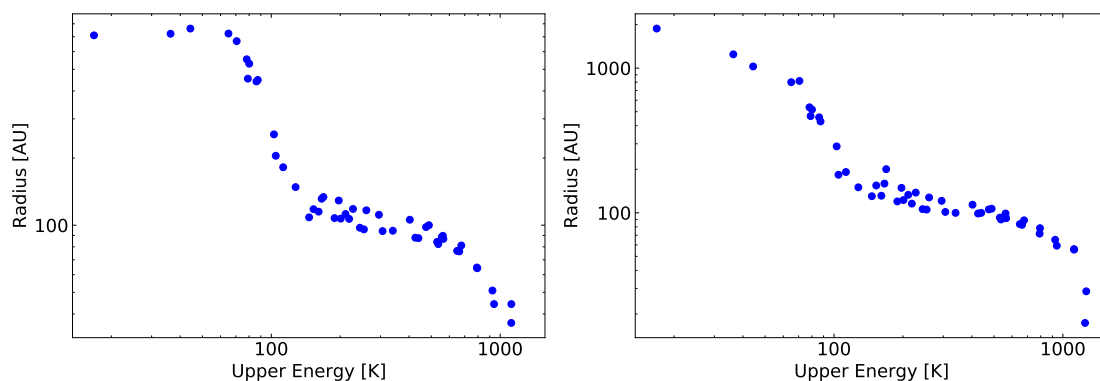


**Figure 24:** The radiative transfer data of  $\text{CH}_3\text{OH}$ . On the left-hand side, all pixels have the same size, and the amount of pixels is the same. On the right-hand side, the amount of pixels is double, but the size of the pixels is smaller for the data with higher energies.

the image with. We tried to convolve the data with a beam size half the size of what we used before, so  $0.25''$ . Here the transition with the highest energy change. However, something also happens to the transitions with the lowest energy. From this analysis, what we can say is that we cannot use the transition with the highest and the lowest energies, but the rest can be used without a problem. For  $\text{CH}_3\text{CHO}$ ,  $\text{CH}_3\text{OCHO}$ , and the rest of the radiative transfer data, the number of pixels and their size is the same for all transition. However, from the analysis above, we can see that something might happen to the data at the highest and lowest energies. We still use the data because we now know that we should not focus on the outer part of our empirical temperature profile but that the data in the middle part is correct and can be used.

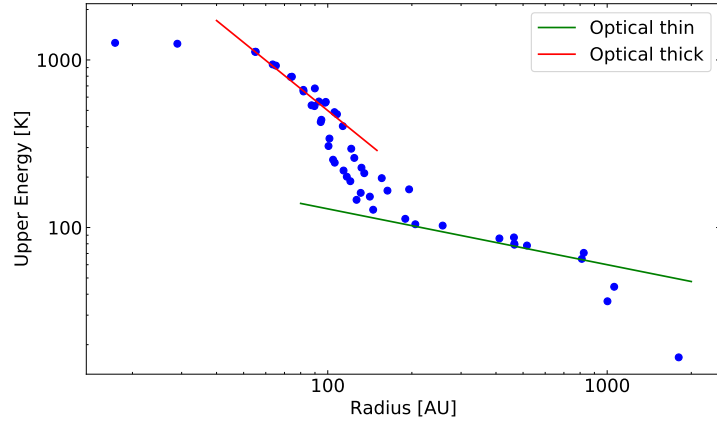
### 6.3 The empirical and theoretical temperature profiles

We found out that it is possible to recreate the observed data with radiative transfer simulation from the previous subsection. Therefore, we want to see if we can compare the temperature profile for the optically thin and thick envelope with the radiative transfer data, just as we did with the observed data in Section 5.

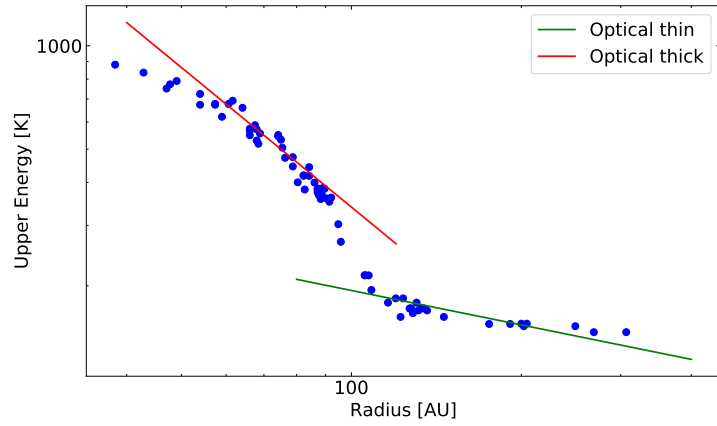
In Section 6.1, we found the values for  $p$  and  $\beta$  used for the radiative transfer simulation, which is also used in the temperature profile in Equation 4 and 5. We want to fit the radiative transfer data from Figure 22 with the temperature profile for both an optical thin and optical thick envelope. We fit it with both temperature profiles because we have more data because the data is computationally produced. The radiative transfer data and the fit for the temperature profiles are in Figure 25. It is vital to notice that we have used the new values for  $p$  and  $\beta$  on 1.7 and 1.48, respectively. From Figure 25, we can see that we have the optical thick envelope at the inner part and the optically thin envelope at the outer part, which is what we expected to see. Furthermore, we can see that we have an optical thick part and an optical thin part, and in the middle, we have a combination of the two. This is most likely what we also saw with the observed data when the data flattens out towards lower energies.

Another possible explanation why the observed data from PILS flattens out was that it was the hot corino we were tracing, and the flatten out was the outer radius where the molecules are in the gas phase. On the radiative transfer data, the data does not flatten out. It is most likely due to us assuming LTE when there is no LTE. However, it is possible to fit the temperature profile of an optical thin envelope in the data, and this is the part where the PILS data flattens out. This might indicate that flatten out in the PILS data is an outer radius of the hot corino.

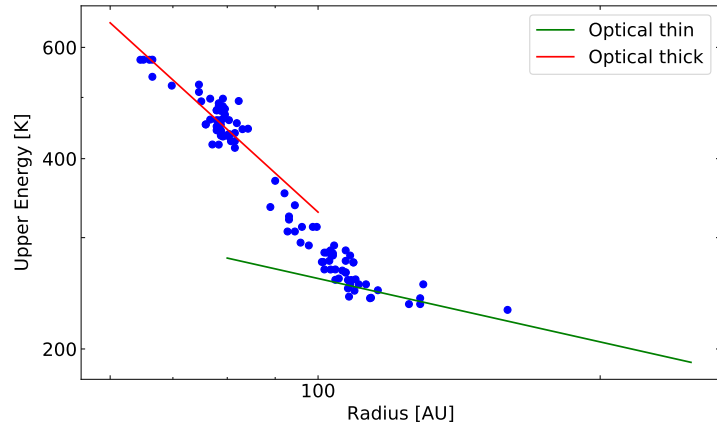
The observed data from PILS with the temperature profile fitted is in Figure 16 and 18. For the temperature profile, we used  $p = 2$  and  $\beta = 2$ , but we know that  $p$  and  $\beta$  can range from 1.5-2. From our radiative transfer model, we found out that the dust profile we use gives us a  $\beta = 1.48$  and that the power-law index we use corresponds to  $p$  is 1.7. Therefore we tried to fit the empirical temperature profile from the PILS data with the optical thick temperature profile, where we used both  $p = 2$  and  $p = 1.7$  and  $\beta = 2$  and  $\beta = 1.48$ . This is in Figure 26, and here it is possible to see that there is some difference in how the two different temperature profile lay compared to each other. However, it does not show that one of the temperature profile is better than the other. Because we cannot say which parameters for the temperature profile is the best, we tried to fit a temperature profile where the power is a free parameter. From the fit, we found out that power should be between  $[-0.5 : -0.6]$ . Here it is the inverted temperature profile we



(a) CH<sub>3</sub>OH



(b) CH<sub>3</sub>CHO



(c) CH<sub>3</sub>OCHO

**Figure 25:** The *Ratran* data in blue and the temperature profile for an optical thin and thick envelope plotted on top. Here we have that the inner part of the envelope is optically thick, and the outer part is optically thin. For the fit, we used  $p = 1.7$  and  $\beta = 1.48$ .

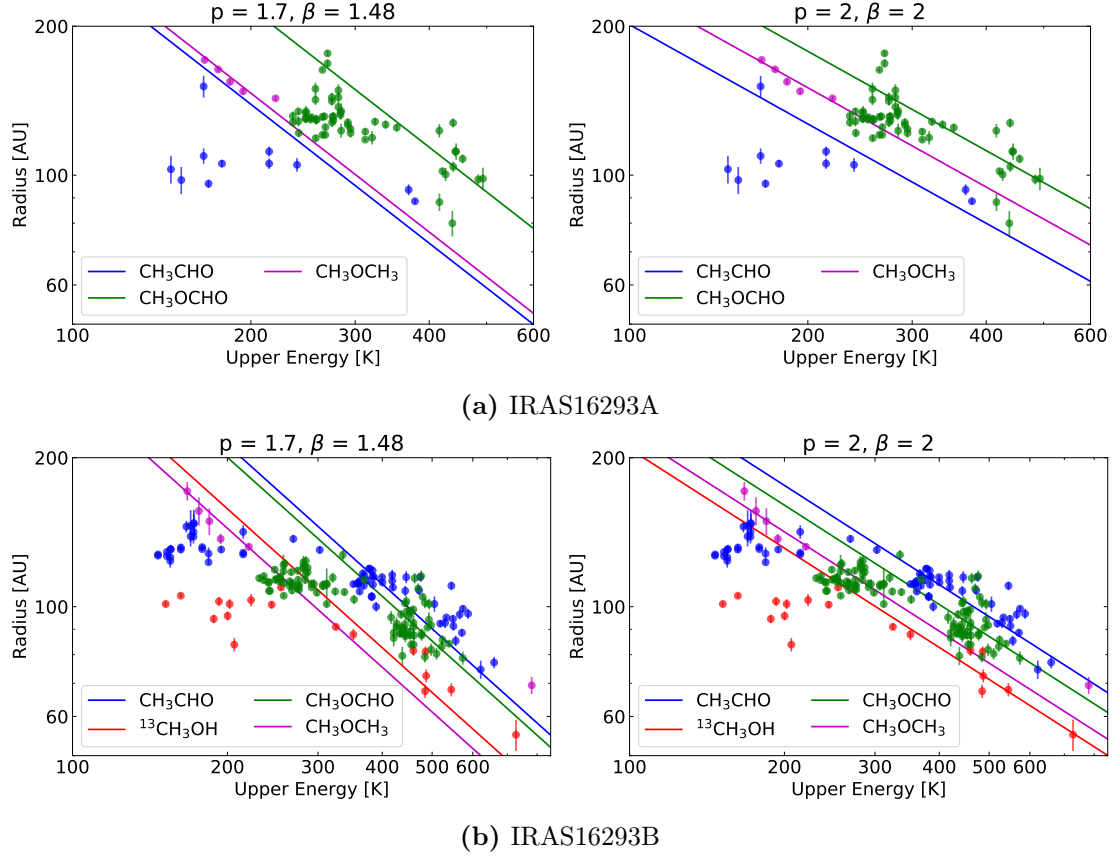


**Figure 26:** The different molecules plotted with the temperature profile for an optical thick envelope. On the left-hand side, we have  $p = 1.5$  and  $\beta = 1.48$ , and on the right-hand side we have  $p = 2$  and  $\beta = 2$ .

used ( see Equation 13), and we get the power of the temperature profile for an optical thick envelope, which is  $-(4 - \beta)/(1 + p)$ . To get as close to the power for the temperature profile, we can see that  $4 - \beta$  needs to be smaller than  $1 + p$ . However, many different values give the power of  $\sim -0.55$ . If we use  $p = 2$  and  $\beta = 2$  as we started with, we get the power to be  $-0.67$ , and if we use  $p = 1.7$  and  $\beta = 1.48$ , which is what we got from the radiative transfer analysis, we get the power to be  $-0.93$ . From this, we were closest with our initial guess for  $p$  and  $\beta$ .

From this analysis, we can say that there is a correlation between the upper energy and the extent of the emission from the line that the temperature profile for an optical thick envelope represents. However, we cannot constrain  $p$  or  $\beta$  within this analysis, but our best guesses are that both  $p$  and  $\beta$  are 2.

## 6.4 The temperature profile dependency on the luminosity

In the final analysis, we want to combine the information we have so far on the empirical and theoretical temperature profile. We want to see what happens when we change the luminosity. In Section 5.3, we looked at the difference in the empirical temperature profile for IRAS16293A and IRAS16293B, and in this section, we want to explore the difference in the luminosity between the two protostars.

The first thing we did was see what happened with the temperature profile from *Transphere* when we change the luminosity with a factor of 10. So we reran *Transphere* with the same parameters as before but changed the luminosity from  $3 L_{\odot}$  to  $30 L_{\odot}$ . This means that the luminosity changes with a factor of 10. With the new temperature profile, we want to compare it with the old one; we want to find the ratio between the two profiles.

To find the ratio of the temperature profile, we need to interpolate the temperature profile. This is because the datapoints we have for the temperature profile are not at the same temperatures but the same radius, and we want to find the difference in radius at a specific temperature. When we interpolate, we take the logarithm to the data and making a linear interpolation. We can do this because we know that the temperature profile follows a power-law function.

Before we look at the ratio between the two temperature profiles, we first look at the theory from Section 1.2.1 to see how much the temperature profile is supposed to change when we change the luminosity with a factor of 10. From Equation 6, we can see how the temperature profile change compared to the luminosity. We already found out that  $\beta = 1.48$  from the dust properties we used to solve the dust radiative transfer code. Therefore, when the luminosity change with a factor of 10, the temperature should change with:

$$T \propto 10^{1/(4-\beta)} = 10^{1/(4-1.48)} = 2.5$$

Where  $T$  is the ratio of the two temperature profiles. When we get the ratio of the two temperature profile where the difference in the luminosity is a factor of 10, the ratio should approach 2.5. However, it is essential to remember that Equation 6 only counts for an optical thick envelope. In section 6.1, we saw that the temperature profile follows an optical thick envelope when we have the highest temperature and the smallest radius, so this is where we should see the ratio approach the value.

In Figure 27, the two different temperature profiles are on the left-hand side of the figure. On the right-hand side of the figure, we have the ratio between the two temperature profiles. Here we can see that the ratio of the temperature profiles approaches a value of 2.35 and that the ratios of the temperature profile almost follow the predicted ratio. So now that we know that the relationship between

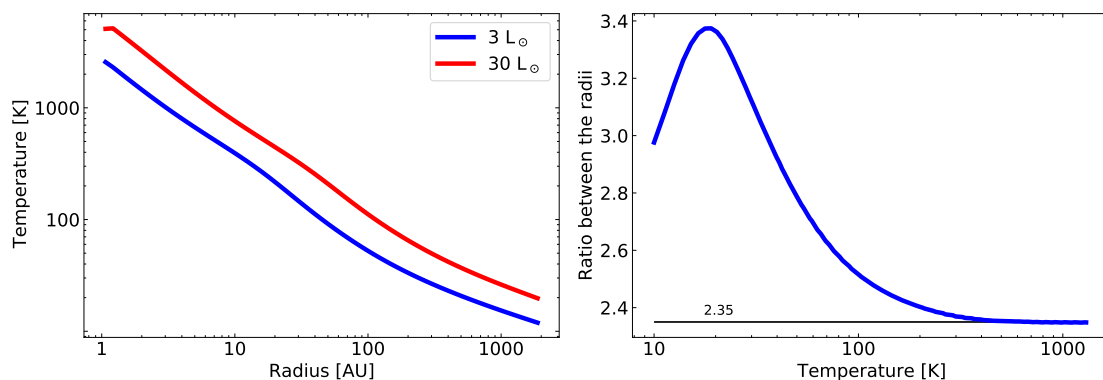


**Figure 27:** On the left-hand side, is the two temperature profile from *Transphere* with different luminosities. On the right-hand side is the ratio between the two.

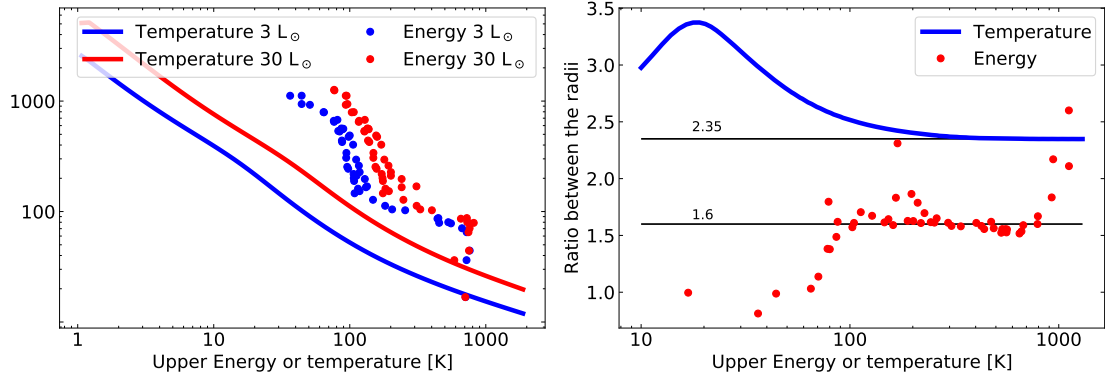
the luminosity and the temperature profile holds, we will compare the ratio of the temperature profile with the ratio of the empirical temperature profile.

To get the ratio of the empirical temperature profile, we ran *Ratran* for CH<sub>3</sub>OH, and we created our own population files for CH<sub>3</sub>CHO and CH<sub>3</sub>OCHO again. We change the luminosity to 30 L<sub>⊙</sub>, but the rest of the parameters stayed the same as in Table 2 and 4. We then created the empirical temperature profile by following the same steps as we did in Section 6.2. We now have two empirical temperature profiles for each molecule, one where the luminosity is 3 L<sub>⊙</sub>, and one with 30 L<sub>⊙</sub>. The ratio between the two empirical temperature profiles is found, so it is possible to compare them with the ratio of the temperature profile from *Transphere*. When we created the new empirical temperature profiles, we used the same transitions for each molecule. This means that we have the same upper energy, but the radius change, so in order to get the ratio between the two profiles, we can just divide them with each other.

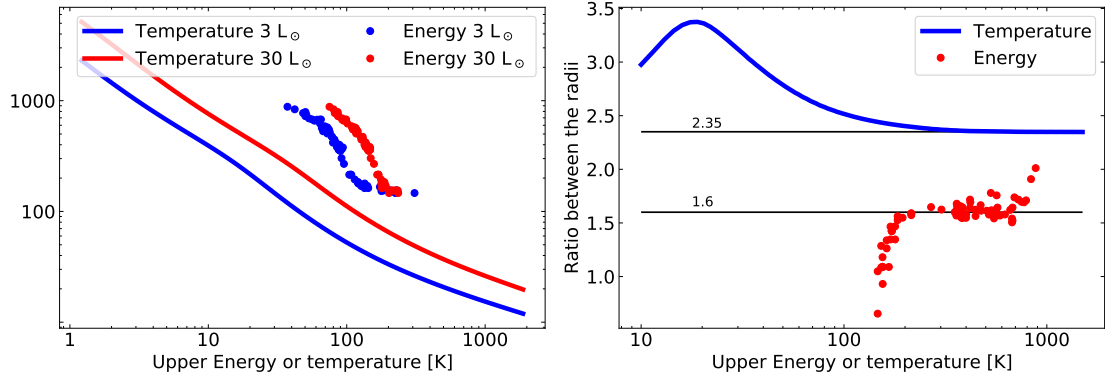
Figure 28 shows the empirical temperature profile and the temperature profile from *Transphere* and their ratio. On the left-hand side, we have the two temperature profiles plotted with the two empirical temperature profile. On the right-hand side, we have the ratio of the temperature profile and the ratio of the empirical temperature profile. When we look at the ratio of the empirical temperature profile, we need to remember that the datapoints with the highest and lowest energies might not be correct, and we need to look at the trend in the middle. From the ratio of the empirical temperature profile for the three different molecules, we can see that they all approach a value of  $\sim 1.6$ . So, when the ratio between the two temperature profile is 2.35, we get a ratio of 1.6 for the empirical temperature profile. Thus, the result is consistent for all three molecules used in the analysis.

The difference between the ratios of the temperature profile and the empirical

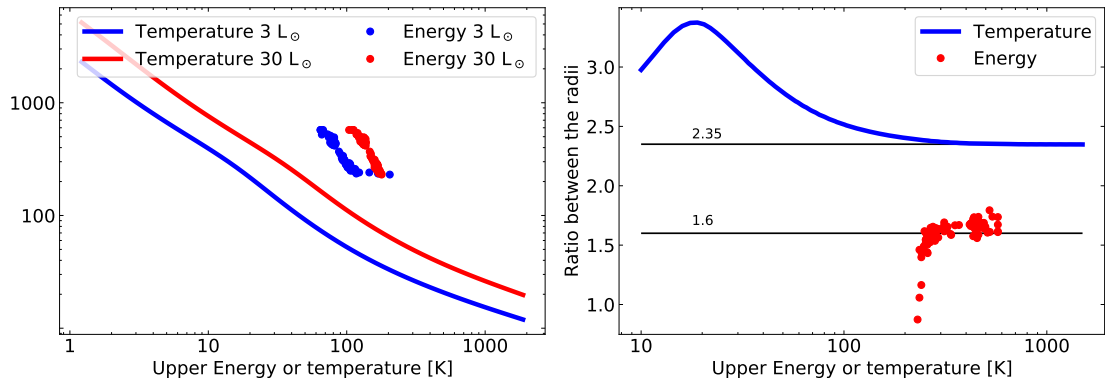




(a) CH<sub>3</sub>OH



(b) CH<sub>3</sub>CHO



(c) CH<sub>3</sub>OCHO

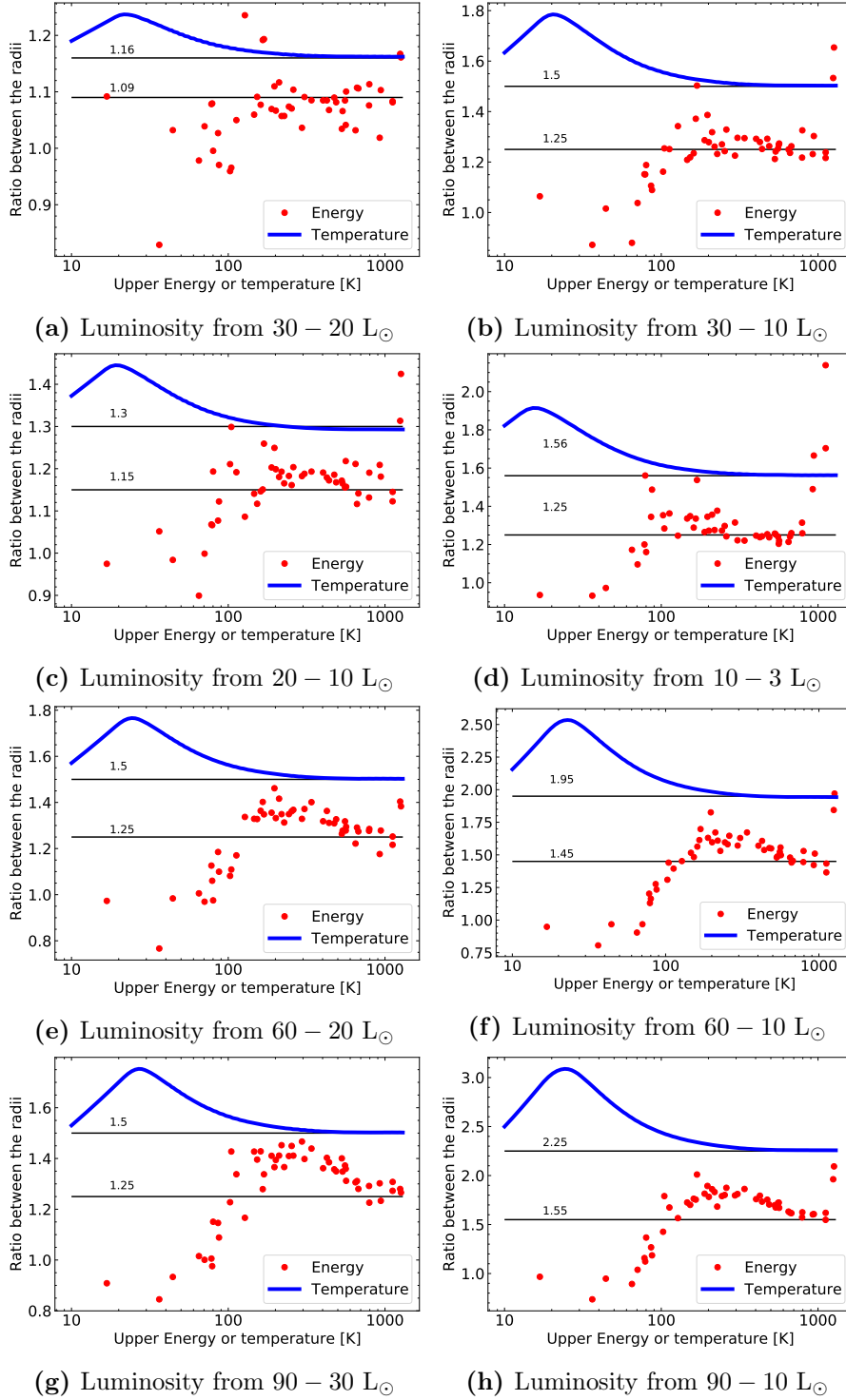
**Figure 28:** On the left-hand side are the temperature profile and the empirical temperature profile for the two different luminosities where the 3 L<sub>⊙</sub> is in blue, and the 30 L<sub>⊙</sub> is in red. On the right-hand side is the ratio between the two temperature profile in blue and the ratio between the two empirical temperature profiles in red. Furthermore, the numbers that the two ratios approached is plotted as the black lines.

temperature profile is consistent with a square root. This means that if we take the square root of the ratio of the temperature profile, we will get the ratio of the empirical temperature profile. Why we have this relationship between the two profiles is unclear.

Now that we know that there is a relation between the ratio of the temperature profile and the empirical temperature profile, we want to test if the relationships hold for different luminosities. We know that the relationship was consistent for all three molecules. However, we only tested this with one luminosity difference. To investigate this further, we expanded the analysis of the ratio between the temperature profile and the empirical temperature profile, but only for CH<sub>3</sub>OH. We used CH<sub>3</sub>OH for this expansion because it is the only molecule where we did not create the level population file ourselves. When we use CH<sub>3</sub>OH, we avoid the issue with LTE because *Ratran* does not assume LTE.

We ran both radiative transfer simulations (*Transphere* and *Ratran*) for CH<sub>3</sub>OH again with the same parameters as seen in Table 2 and 4, but with a luminosity of 10 L<sub>⊙</sub>, 20 L<sub>⊙</sub>, 60 L<sub>⊙</sub> and 90 L<sub>⊙</sub>. For the radiative transfer code with a luminosity of 60 L<sub>⊙</sub> and 90 L<sub>⊙</sub>,  $r_{in}$  was changes to 1.3 AU and 1.5 AU respectively. With this expansion, we can look at the ratio where the luminosity change with a factor of 1.5, 2, 3, 6 and 9, and we have multiple ratios where the luminosity change with a factor of 3.

The ratio between the temperature profiles and the empirical temperature profile for different luminosity ratios are in Figure 29. The black lines showed the expected ratio of the temperature profile and the empirical temperature profile. Looking at the first four plots (Figure 29a, 29b, 29c and 29d), it is possible to see that the ratios all follow the predicted ones. Thus, for the temperature profile, the ratio follows Equation 6 and for the empirical temperature profile, we have the ratio follows the square root of the temperature profile. For the four last figures, this trend is not very clear. For the temperature profile, we still see that the ratio follows the predicted ratio. However, for Figure 29e, 29f, 29g and 29h, the ratio of the empirical temperature profile does not follow the trend entirely, which is shown in the black lines. One thing these figures have in common is the high luminosity. For both the 60 L<sub>⊙</sub> and 90 L<sub>⊙</sub>, we had to move the inner radius out to get the code to work. With the high luminosity we used, the source needs to be bigger to use the same parameters. Because of this, they got bigger than our inner radius of 1 AU. However, the biggest problem with the empirical temperature profile for the two luminosities is that the emission most likely gets optical thick. This means that the empirical temperature profile will not scale the same way as for lower luminosities.



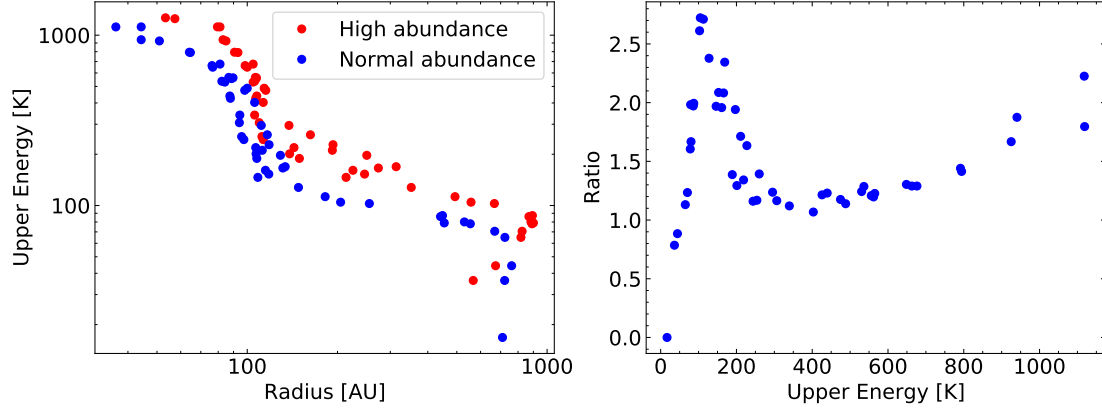
**Figure 29:** The ratio between the temperature profiles for two different luminosities in blue and in red is the ratio between the empirical temperature profiles.

Figure 29, shows the relationship between the ratio of the temperature profile and the empirical temperature profile holds. Nevertheless, it is essential to know that this relationship breaks down if the luminosity gets too high. From the figure, it looks like a luminosity of  $30 L_{\odot}$  is low enough for the relationship to hold, but a luminosity of  $60 L_{\odot}$  is too high.

From the relationship between the temperature profile and the empirical temperature profile, it should be possible to find the luminosity between IRAS16293A and IRAS16293B. This is because we have the joint luminosity of IRAS16293 of  $\sim 21 L_{\odot}$ . This luminosity is found with a distance of 120 pc, and in our code, we used a distance of 141 pc. However, this is the best estimate we have for the luminosity, so we still use it. For the analysis of the relationship, we saw an upper limit for how high the luminosity could be. However, the analysis worked with a luminosity of  $30 L_{\odot}$  and the luminosity for IRAS16293 is  $\sim 21 L_{\odot}$ , so this should not be an issue. However, there is one caveat we need to address first.

The way we construct the empirical temperature profile makes it sensitive to the abundance of the molecule. This means that if we have a higher abundance, the radius will get higher. To find out how much the abundance affects the empirical temperature profile, we ran the radiative transfer code for  $\text{CH}_3\text{OH}$  again. We used the same parameters as in Table 2, but we used an abundance that is a factor of 10 higher. The abundance does not change the temperature profile, as shown on the flow chart in Figure 6. So the temperature profile is the same even though we change the abundance with a factor of 10. From the radiative transfer code, we constructed a new empirical temperature profile. We can now compare the two empirical temperature profile, where the only change is the abundance. The two empirical temperature profile is in Figure 30 on the left-hand side, and on the right-hand side is the ratio between the two empirical temperature profile. From the figure it is possible to see the when we use a higher abundance for  $\text{CH}_3\text{OH}$ , we get larger radii in the empirical temperature profile. From the ratio, we can see that if we use an abundance a factor of 10 higher, we get a ratio of approximately 1.2. Again, we do not look at the highest and lowest energies.

In Figure 28a, we have changed the luminosity with a factor of 10, and the ratio of the empirical temperature profile is 1.6. On the other hand, from Figure 30 we get a ratio of the empirical temperature profile of 1.2 when we change the abundances with a factor of 10. This means that the change in luminosity is more important than the change in abundance. However, if we used the empirical temperature profile to find the relationship between two luminosities, it is crucial to make sure that the abundances of the molecules are comparable.



**Figure 30:** On the left-hand side is the two empirical temperature profiles for  $\text{CH}_3\text{OH}$ , where the abundance is a factor 10 higher for the model in red. On the right-hand side is the ratio between the two.

Now that we know that the abundance changes the ratio of the empirical temperature profile, it is important that the abundance of the molecules used when comparing the empirical temperature profiles are comparable. In Section 5.3, we compared three different molecules for IRAS16293A and IRAS16293B. For the ratio of the empirical temperature profile, we got:

$$\begin{aligned} \text{CH}_3\text{CHO} &: 0.65 \pm 0.01 \\ \text{CH}_3\text{OCHO} &: 1.11 \pm 0.01 \\ \text{CH}_3\text{OCH}_3 &: 1.06 \pm 0.01 \end{aligned}$$

Here we got that the ratio for  $\text{CH}_3\text{OCHO}$  and  $\text{CH}_3\text{OCH}_3$  is as expected because Jacobsen et al. (2018) found that the luminosity of IRAS16293A is higher. However, for  $\text{CH}_3\text{CHO}$ , we got the opposite.

Manigand et al. (2020) compared the abundance of IRAS16293A and IRAS16293B for different COMs. From Figure 2 in Manigand et al. (2020) we can see that the abundance of  $\text{CH}_3\text{OCHO}$  and  $\text{CH}_3\text{OCH}_3$  are comparable, but if we look at the abundance of  $\text{CH}_3\text{CHO}$ , the abundance of IRAS16293B is a factor  $\sim 20$  higher. In order to constrain the luminosities of IRAS16293A and IRAS16293B, the abundance needs to be comparable, so we can not use  $\text{CH}_3\text{CHO}$  for this. In the figure, we have that the abundance of the molecule is over  $\text{CH}_3\text{OH}$  for each protostar. To ensure that the abundance of  $\text{CH}_3\text{OCHO}$  and  $\text{CH}_3\text{OCH}_3$  are comparable, we need to make sure that the abundance of  $\text{CH}_3\text{OH}$  is also comparable. Kuan et al. (2004) found the abundance of  $\text{CH}_3\text{OH}$  for IRAS16293A is a factor 2 higher than for IRAS16293B. This means that we can use  $\text{CH}_3\text{OCHO}$  and  $\text{CH}_3\text{OCH}_3$  to get the relationship of the empirical temperature profile because the abundances are

comparable.

We now know that we can use  $\text{CH}_3\text{OCHO}$  and  $\text{CH}_3\text{OCH}_3$  to constrain the luminosity of the two protostars because of the abundance for IRAS16293A and IRAS16293B are comparable, and the luminosity of the whole system is known and low enough to use.

From Figure 19 we got the ratio between the  $\text{CH}_3\text{OCHO}$  and  $\text{CH}_3\text{OCH}_3$  for IRAS16293. From  $\text{CH}_3\text{OCHO}$  and  $\text{CH}_3\text{OCH}_3$ , the ratio is  $\sim 1.1$ . From this ratio, we can get the ratio of the temperature profile by squaring it. The ratio between the temperature profiles should be  $1.1^2 = 1.2$ . Now it is possible to find the luminosity difference by using Equation 6, but inverting it:

$$L \propto T^{4-\beta} = 1.2^{4-1.48} = 1.6$$

Where  $T$  is the ratio of the temperature profile, and  $\beta$  is 1.48 as found earlier.

We now have the relationship between the two luminosities, and we have the luminosity of the whole system. This means that we can find the luminosity of each protostar because we have two equations with two unknown:

$$\begin{aligned} \frac{L_A}{L_B} &= 1.6 \\ L_A + L_B &= 21 L_\odot \end{aligned}$$

Solving these equations leads to  $L_A = 13 L_\odot$  and  $L_B = 8 L_\odot$ . The luminosity of IRAS16293B is much larger than previously found by Jacobsen et al. (2018), However, the ratio from the empirical temperature profile for both  $\text{CH}_3\text{OCH}_3$  and  $\text{CH}_3\text{OCHO}$  point to another luminosity.

Looking at Figure 22, the PILS data for  $\text{CH}_3\text{CHO}$  and  $\text{CH}_3\text{OCHO}$  has a larger radius for the same upper energies than the *Ratran* data. One of the reasons for this could be that we used a luminosity that is too low. From the analysis above, we got a luminosity for IRAS16293B of  $8 L_\odot$ , which is higher than the luminosity we used of  $3 L_\odot$ . This is most likely why the PILS data does not match the radiative transfer data. For  $\text{CH}_3\text{OH}$ , the PILS data is of  $^{13}\text{CH}_3\text{OH}$ , and the radiative transfer data is of  $\text{CH}_3\text{OH}$ . This can be why we see that the PILS data has a smaller radius for the same upper energies than the *Ratran* data.

By comparing the analysis using radiative transfer data and the analysis using observed data, it is possible to give a constrain on the luminosities of IRAS16293A and IRAS16293B. This is done by first finding the relationship between the luminosity, the temperature profile and the empirical temperature profile in a controlled experiment using radiative transfer simulation. From that analysis, it was possible to compare it with the empirical temperature profile found from the observed data

of IRAS16293A and IRAS16293B. From this comparison, we got a luminosity for the two protostars,  $L_A = 13 L_\odot$  and  $L_B = 8 L_\odot$ .

IRAS16293A has a higher luminosity than IRAS16293B. There could be several reasons for it, and we will discuss a few. We need to look back at Section 1.2 to see what we know about the evolution of star formation. The first reason could be that the two sources are in different stages of their evolution. Both sources are classified as class 0, but there can still be a difference in their ages. Depending on their age, the luminosity change meaning that even if they were the same size, they would have different luminosities if they were not the same age. From class 0 to I, the accretion rate is supposed to drop. When we have a Bonnor-Ebert sphere, the inner part is a uniform core, where we have a high accretion rate. For the outer part, we have a singular isothermal sphere, where the accretion rate is constant and lower. This means that as time goes the accretion rate drops. From Equation 3, we can see that if we have a lower accretion rate, the luminosity should be smaller. However, as the accretion rate becomes smaller, the protostar's mass becomes bigger, so the luminosity does not necessarily become smaller. However, the precise relationship between luminosity and time is unknown. Another reason for the difference in luminosity could be the difference in mass and size between the two protostars. If we consider a scenario where the two protostars are the same age, their luminosity still depends on their mass and size (see Equation 3). Therefore their properties could be a reason for the difference in luminosity.

Jacobsen et al. (2018) found that the luminosity of IRAS16293A should be a factor of 6 higher than IRAS16293B, as mentioned earlier. This is quite different from what we found: the difference is a factor of 1.6. Jacobsen et al. (2018) found the different luminosities using 3D modelling, and match the modelled data with the 868  $\mu\text{m}$  dust continuum and CO isotopologues. Jacobsen et al. (2018) could not constrain the disk structure around IRAS16293A, and for IRAS16293B, they found that the dust density structure must be vertically extended to match the observed properties. From this, it is possible to say that it was not easy modelling the two protostars, and these complications might give a wrong answer for the luminosities. Furthermore, Jacobsen et al. (2018) used CO isotopologues as the emission data. However, CO evaporates of grain at a low temperature, so it might not only be the two sources it trace but also the emission between them. Jacobsen et al. (2018) included a bridge between the two protostars, so they modelled three things at once, which is why it makes sense to use CO isotopologues. However, our method used COMs to ensure that the emission we investigate only came from the protostars themselves. This could be the reason why we get two different answers for the luminosity of IRAS16293A and IRAS16293B.

## 7 Conclusion and summary

This thesis presents analyses of the binary system IRAS16293 using data from ALMA PILS and radiative transfer simulation. For the first three analyses of the thesis, analyses of IRAS16293 are done using O-bearing COMs. For the final part, we use radiative transfer code to recreate the result found in the first part and compare the temperature profile and the empirical temperature profile.

- First, several lines of different O-bearing complex organic molecules are identified, and contour maps of IRAS16293A and IRAS16293B were created successfully.
- An analysis of the structure of the molecule seen on the contour maps for IRAS16293B is done for three different COMs. Here it is explored how the optical depth, i.e. the Einstein A coefficient, change the structure of the molecule. In the contour maps, a feature is seen, and if the Einstein A coefficient is large, i.e. the optical depth is large, the feature in the structure on the contour maps become more visible. This was clear to see for two of the three molecules analysed. However, more molecules need to be investigated to know if this trend is valid for all molecules. Furthermore, this analysis needs to be done for more protostars to know if this is a common trend.
- Next, an analysis of the upper energy and the extent of the emission from the line is made. From this analysis, it was possible to see that the lower the upper energy for a transition is, the larger is the extent of the molecular emission. This analysis is done for both IRAS16293A and IRAS16293B and for three and four COMs, respectively. From the plot of the radius of the molecular emission and the upper energy, it was possible to fit the temperature profile for an optical thick envelope for the highest energies, which have the smallest radii; this is the empirical temperature profile.
- From the empirical temperature profile of IRAS16293A and IRAS16293B, we tried to constrain  $p$  and  $\beta$  from the temperature profile. There was no one clear answer for this; however, our best guess is that  $p = 2$  and  $\beta = 2$ .
- From dust radiative transfer simulations, it was possible to create a temperature profile for a protostar that resemble IRAS16293B. This temperature profile was successfully fitted with the theoretical temperature profile for an optically thick and thin envelope. Therefore, we can say that the envelope must be optically thick at the centre and optical thin further out. However, in the middle of the envelope is a combination of the two.



- With detailed dust and line radiative transfer simulations, the empirical temperature profile for IRAS16293B was recreated for three different COMs. Furthermore, it was possible to fit the empirical temperature profile from the radiative transfer data with the theoretical temperature profile for both an optically thick and thin envelope. Again, we got that the inner part is optically thick, and the outer part is optically thin. Because the data was computationally created, it was possible to fit both temperature profiles.
- Finally, radiative transfer simulations are used to constrain the relationship between the luminosity, the temperature profile and the empirical temperature profile. We tested what happens with the temperature profile and the empirical temperature profile if we change the luminosity with a factor of 1.5, 2, 3, 6, 9 and 10. For this analysis, we look at the ratio of the temperature profile and the ratio of the empirical temperature profile when the luminosity changes. The ratio of the temperature profiles follows the relationship for the luminosity for an optical thick envelope. For the ratio of the empirical temperature profile, it was a square root of the temperature profile.
- From this relationship between the temperature profile and the empirical temperature profile, found from the radiative transfer simulation, the empirical temperature profile for IRAS16293A and IRAS16293B is used to constrain the luminosities of the two. IRAS16293 has a luminosity of  $\sim 21 L_{\odot}$  and we found  $L_A = 13 L_{\odot}$  and  $L_B = 8 L_{\odot}$ .
- The difference in luminosity between IRAS16293A and IRAS16293B could be because of the two protostars having different properties. For example, the age of the protostars, the size, mass, and accretion rate of the two protostars can change the luminosity.

A new method on constraining each protostar’s luminosity in a protostellar binary system is found in this thesis. More COMs from other protostellar systems needs to be analysed to check if the relationship holds. From analysing the upper energy as a function of the extent of the molecular emission, the temperature profile was found. This was possible to do for both protostars in this system, but further analysis would help validate it. With ALMA, it is possible to zoom in on small scales during star formation, and more knowledge of what is going on during the earliest phases is obtained, but there are still many unknown questions to explore.

## Acknowledgements

I want to give a special thanks to my supervisor, Jes Jørgensen, for providing professional support throughout the process of writing this thesis. It was very helpful how quickly he adapted when the pandemic changes the working conditions, making it easy to continue my work through troubling times. It has been an educational experience and a pleasure to work with you. Thank you for always staying patient, providing inspiring discussions and encouraging me to stay curious. I will also like to thanks Hannah Calcutt for introducing me to the VINE maps and helping me to get them to work. Finally, I would like to thanks the submm group at starplan for the weekly meeting and discussion.

## References

- Calcutt, H. et al. 2018, *A&A*, 616, A90
- Dunham, M. M., et al. 2015, *The Astrophysical Journal Supplement Series*, 220, 11
- Dzib, S. A. et al. 2018, *A&A*, 614, A20
- Goldsmith, P. F., & Langer, W. D. 1999, *ApJ*, 517, 209
- Hartmann, L. 2008, *Accretion Processes in Star Formation*, 2nd edn., Cambridge Astrophysics (Cambridge University Press)
- Herbst, E., & Van Dishoeck, E. F. 2009, *Annual Review of Astronomy and Astrophysics*, 47, 427
- Hogerheijde, M. R., & van der Tak, F. F. S. 2000, *A&A*, 362, 697
- Jacobsen, S. K., et al. 2018, *A&A*, 612, A72
- Jeans, J. H. 1902, *Philosophical Transactions of the Royal Society of London Series A*, 199, 1
- Jørgensen, J. K., Belloche, A., & Garrod, R. T. 2020, *ARA&A*, 58, 727
- Jørgensen, J. K., et al. 2016, *A&A*, 595, A117
- . 2018, *A&A*, 620, A170
- Jørgensen, J. K., Bourke, T. L., Nguyen Luong, Q., & Takakuwa, S. 2011, *A&A*, 534, A100
- Kuan, Y.-J., et al. 2004, *The Astrophysical Journal*, 616, L27
- Larson, R. B. 1969, *MNRAS*, 145, 271
- Manigand, S., et al. 2020, *A&A*, 635, A48
- Oya, Y., et al. 2018, *The Astrophysical Journal*, 854, 96
- Schöier, F. L., Jørgensen, J. K., van Dishoeck, E. F., & Blake, G. A. 2002, *A&A*, 390, 1001
- Stahler, S. W., & Palla, F. 2004, *The Formation of Stars*
- van der Wiel, M. H. D., et al. 2019, *A&A*, 626, A93
- van Dishoeck, E. F. 1988, *Molecular Cloud Chemistry*, ed. R. D. Wolstencroft & W. B. Burton (Dordrecht: Springer Netherlands), 117–164
- Wilson, T. L. 2009, *Introduction to Millimeter/Sub-Millimeter Astronomy*

# A Appendix: Contour maps

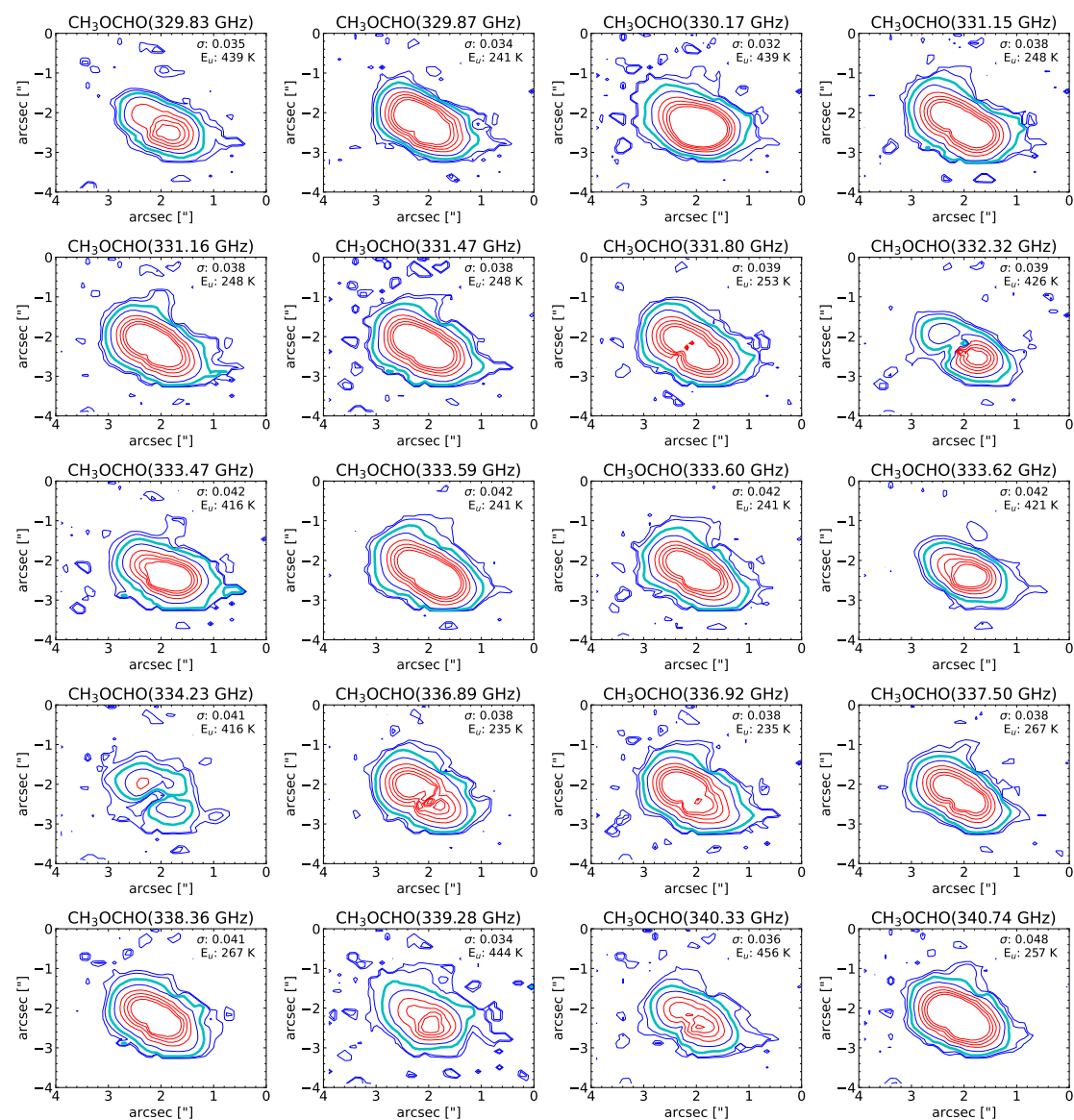


**Figure A.1:** Contour maps of CH<sub>3</sub>OCHO for IRAS16293A. The different levels are for  $3\sigma$ ,  $5\sigma$ ,  $10\sigma$ ,  $20\sigma$ ,  $40\sigma$ ,  $60\sigma$ ,  $80\sigma$ ,  $100\sigma$ , where the  $10\sigma$  contour is in cyan. The upper energy and  $\sigma$  is displayed on the maps.

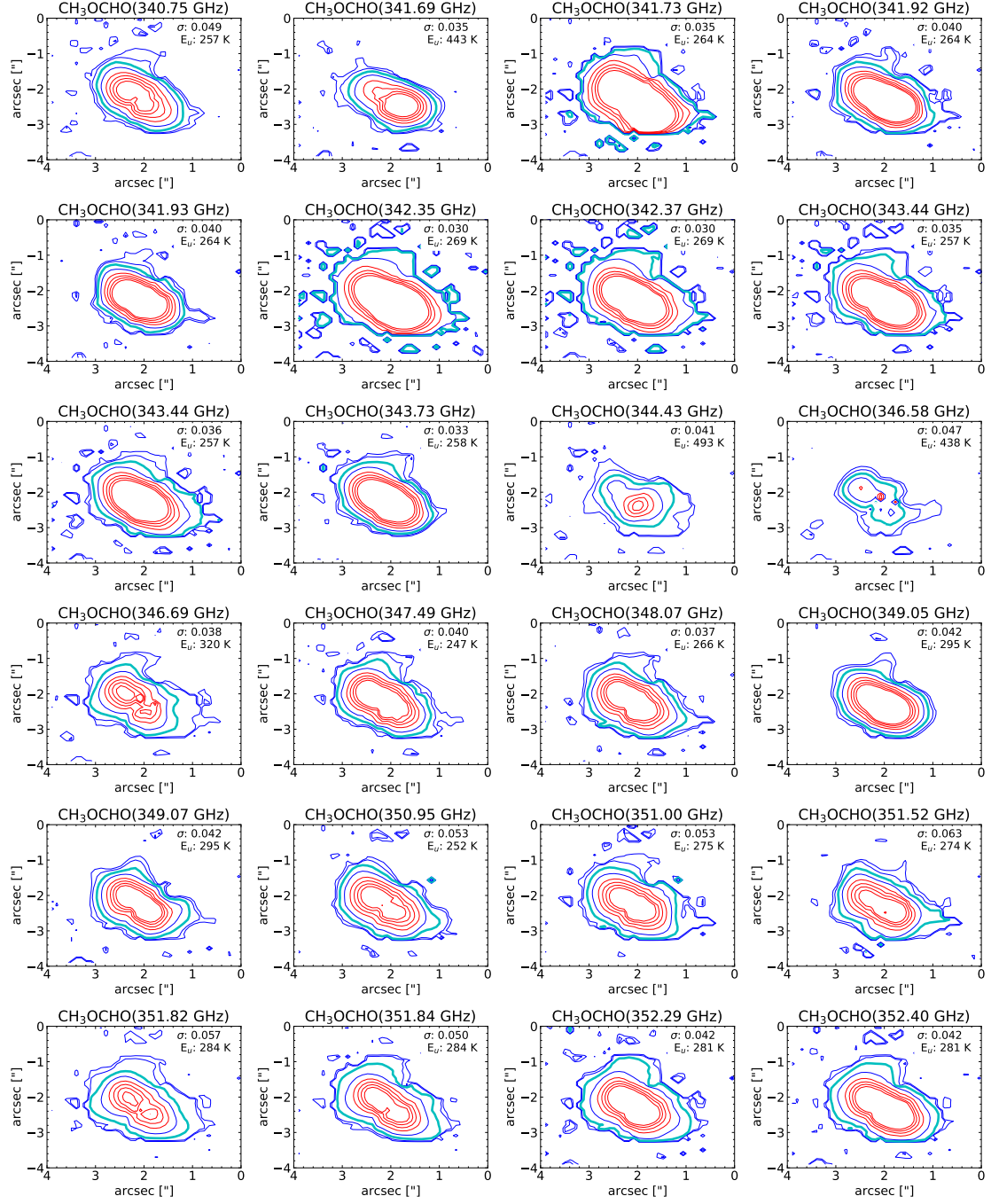


**Figure A.2:** Contour maps of CH<sub>3</sub>OCHO for IRAS16293A. The different levels are for 3σ, 5σ, 10σ, 20σ, 40σ, 60σ, 80σ, 100σ, where the 10σ contour is in cyan. The upper energy and σ are displayed on the maps.

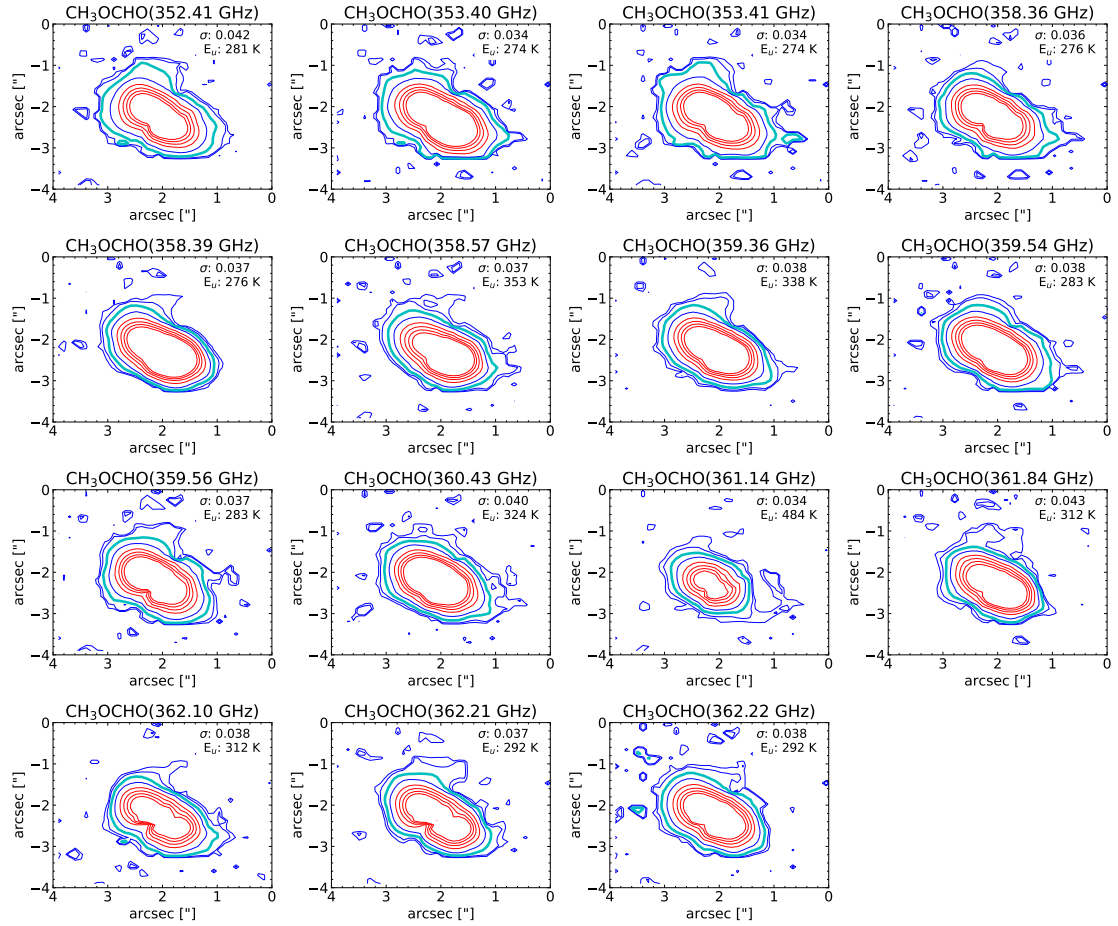


**Figure A.3:** Contour maps of CH<sub>3</sub>OCHO for IRAS16293A. The different levels are for  $3\sigma$ ,  $5\sigma$ ,  $10\sigma$ ,  $20\sigma$ ,  $40\sigma$ ,  $60\sigma$ ,  $80\sigma$ ,  $100\sigma$ , where the  $10\sigma$  contour is in cyan. The upper energy and  $\sigma$  is displayed on the maps.

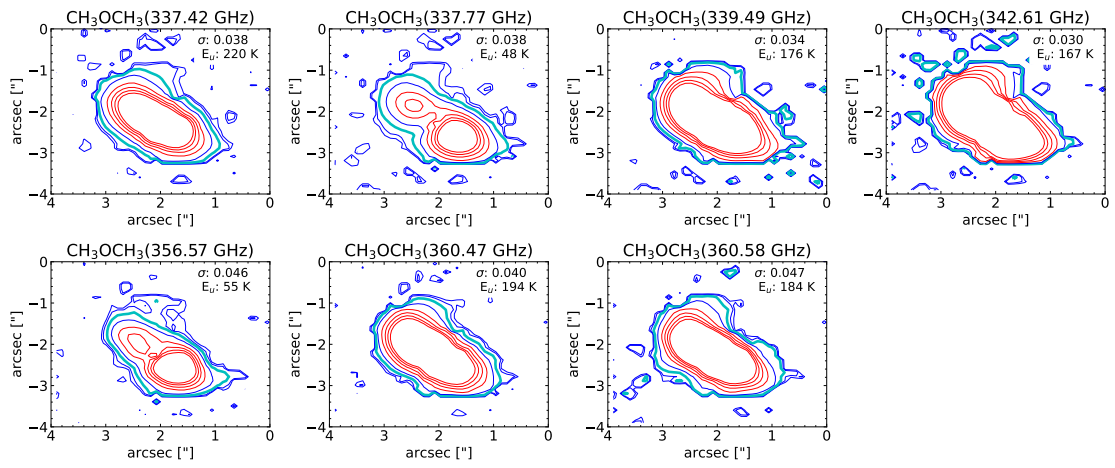


**Figure A.4:** Contour maps of  $\text{CH}_3\text{OCH}_3$  for IRAS16293A. The different levels are for  $3\sigma$ ,  $5\sigma$ ,  $10\sigma$ ,  $20\sigma$ ,  $40\sigma$ ,  $60\sigma$ ,  $80\sigma$ ,  $100\sigma$ , where the  $10\sigma$  contour is in cyan. The upper energy and  $\sigma$  is displayed on the maps.

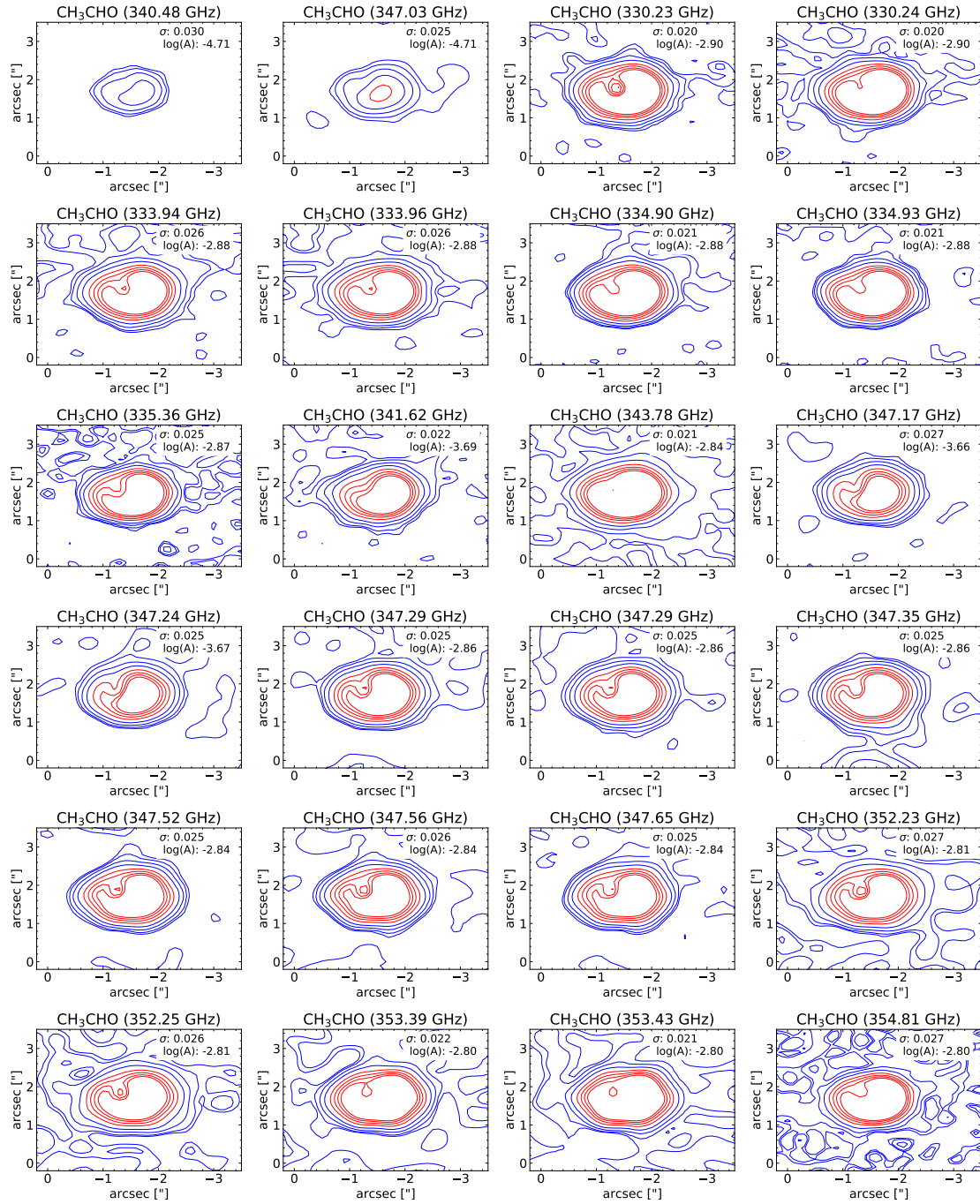


**Figure A.5:** Contour maps of CH<sub>3</sub>CHO for IRAS16293B. The different levels are for  $3\sigma$ ,  $5\sigma$ ,  $10\sigma$ ,  $20\sigma$ ,  $40\sigma$ ,  $60\sigma$ ,  $80\sigma$ ,  $100\sigma$ . The Einstein A coefficient and  $\sigma$  is displayed on the plots.

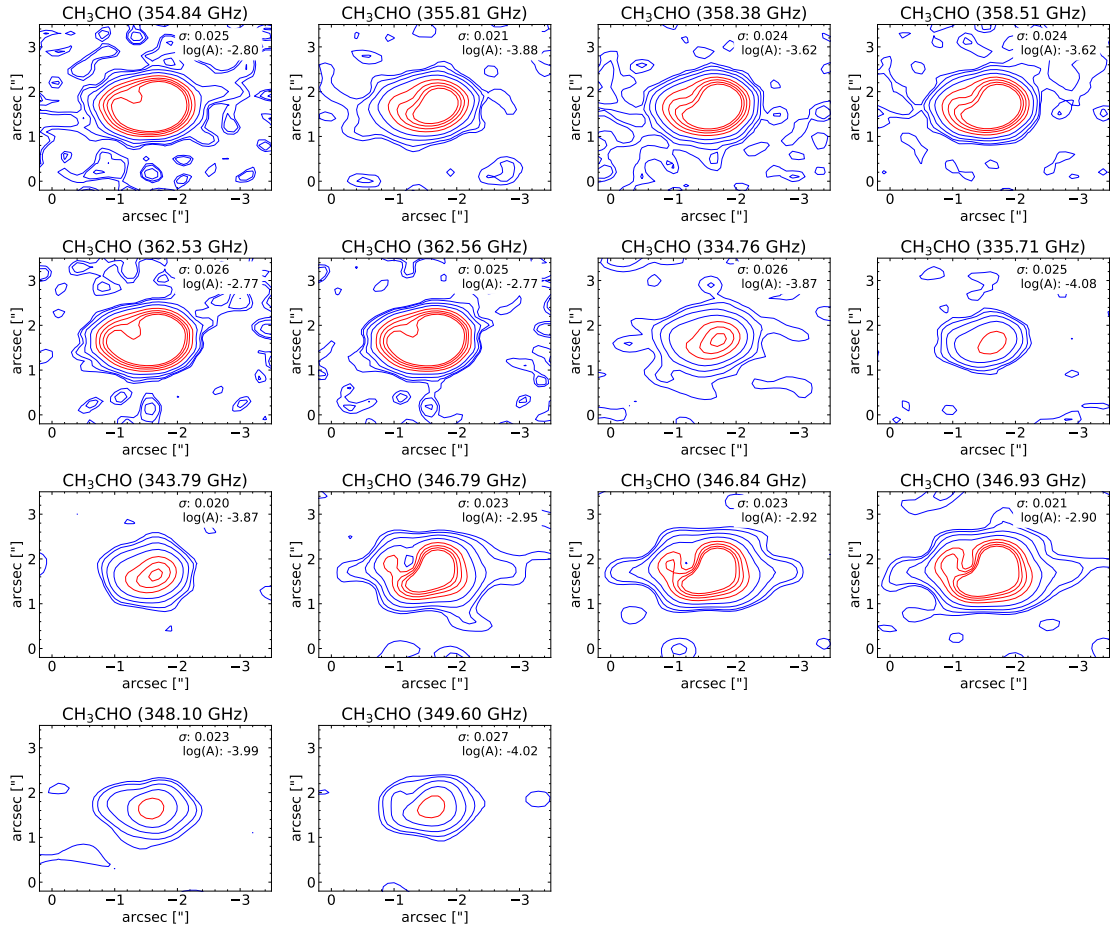


**Figure A.6:** Contour maps of CH<sub>3</sub>CHO for IRAS16293B. The different levels are for 3σ, 5σ, 10σ, 20σ, 40σ, 60σ, 80σ, 100σ. The Einstein A coefficient and σ is displayed on the plots.



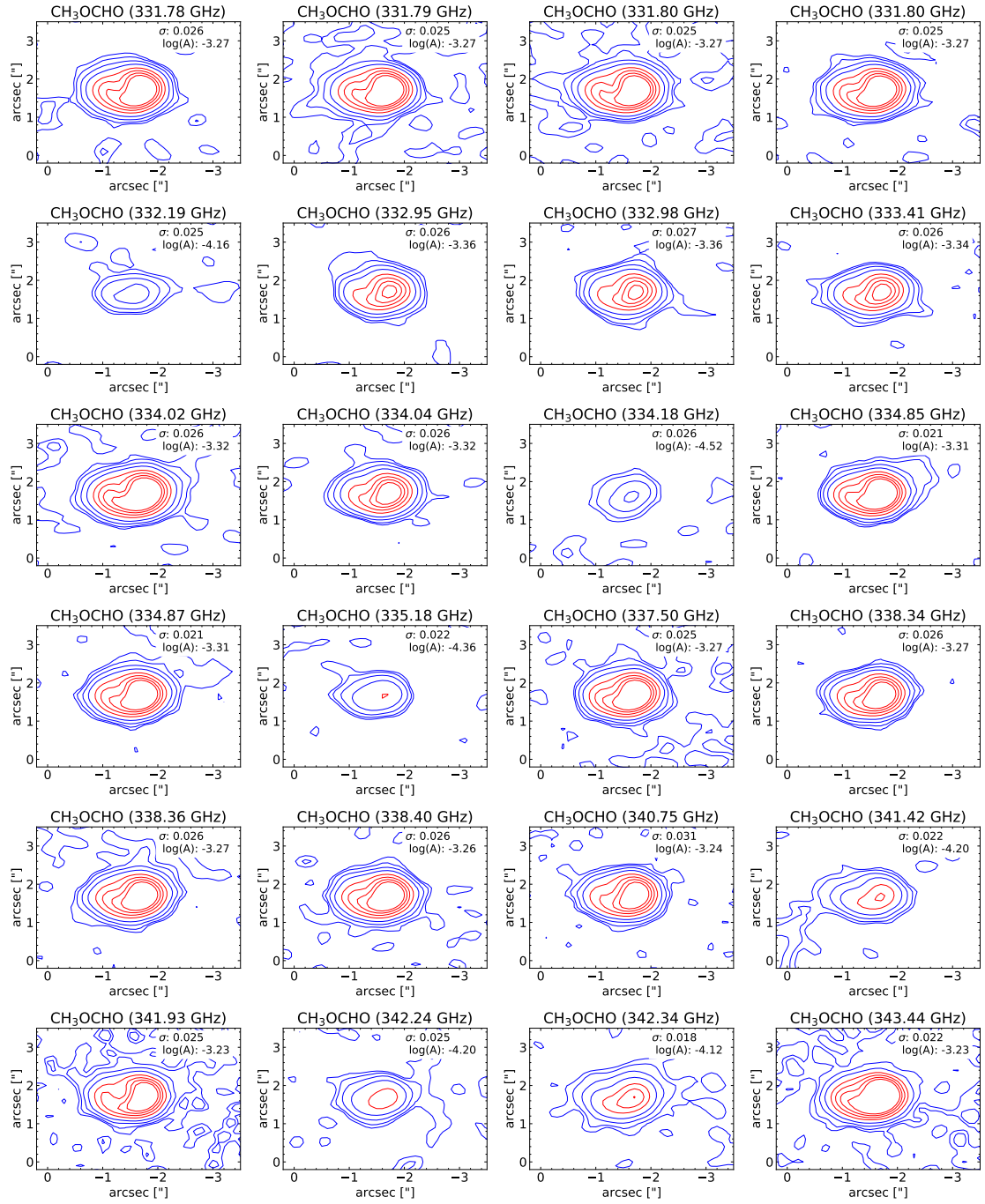


**Figure A.7:** Contour maps of CH<sub>3</sub>OCHO for IRAS16293B. The different levels are for  $3\sigma$ ,  $5\sigma$ ,  $10\sigma$ ,  $20\sigma$ ,  $40\sigma$ ,  $60\sigma$ ,  $80\sigma$ ,  $100\sigma$ . The Einstein A coefficient and  $\sigma$  is displayed on the plots.

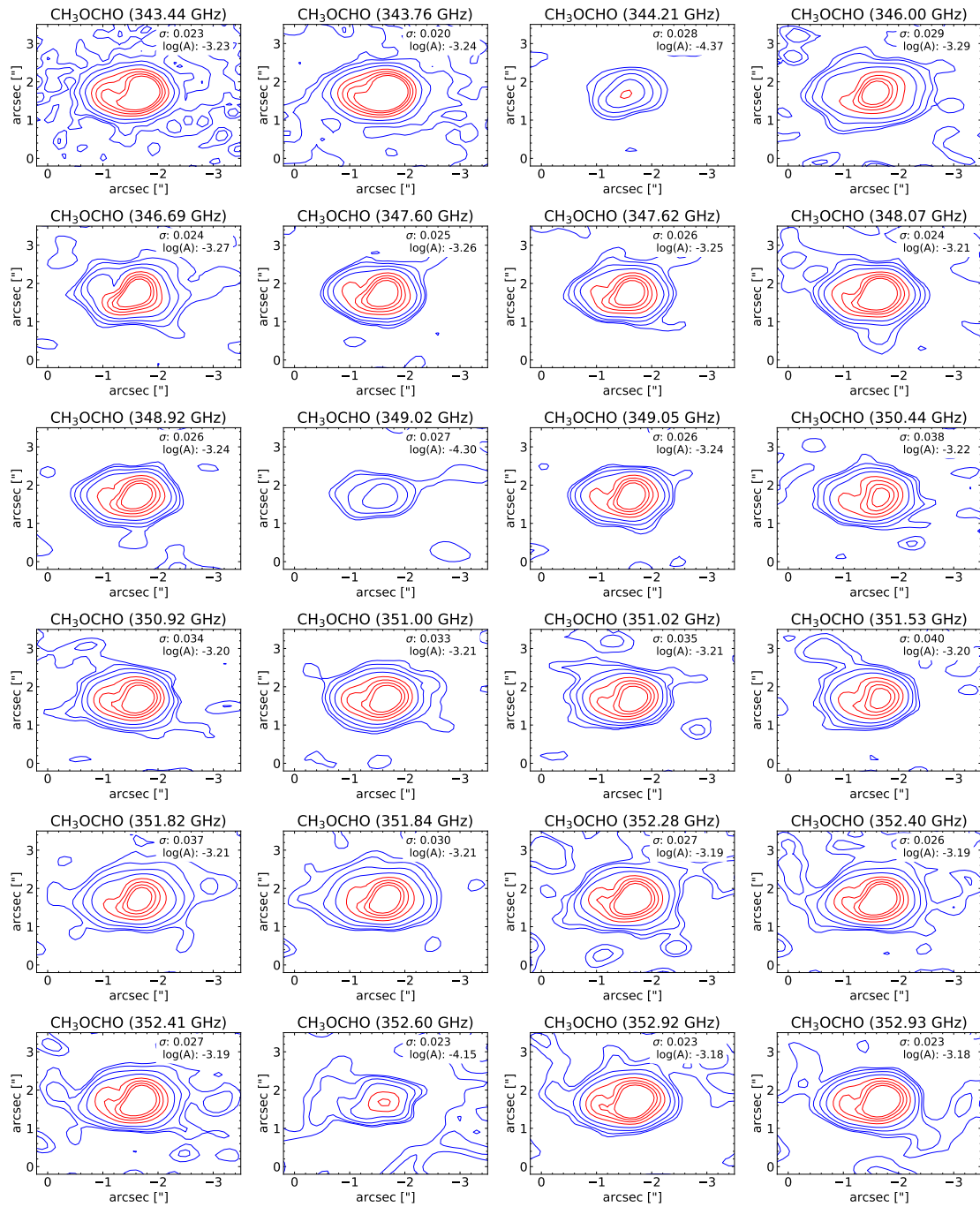


**Figure A.8:** Contour maps of CH<sub>3</sub>OCHO for IRAS16293B. The different levels are for  $3\sigma$ ,  $5\sigma$ ,  $10\sigma$ ,  $20\sigma$ ,  $40\sigma$ ,  $60\sigma$ ,  $80\sigma$ ,  $100\sigma$ . The Einstein A coefficient and  $\sigma$  is displayed on the plots.

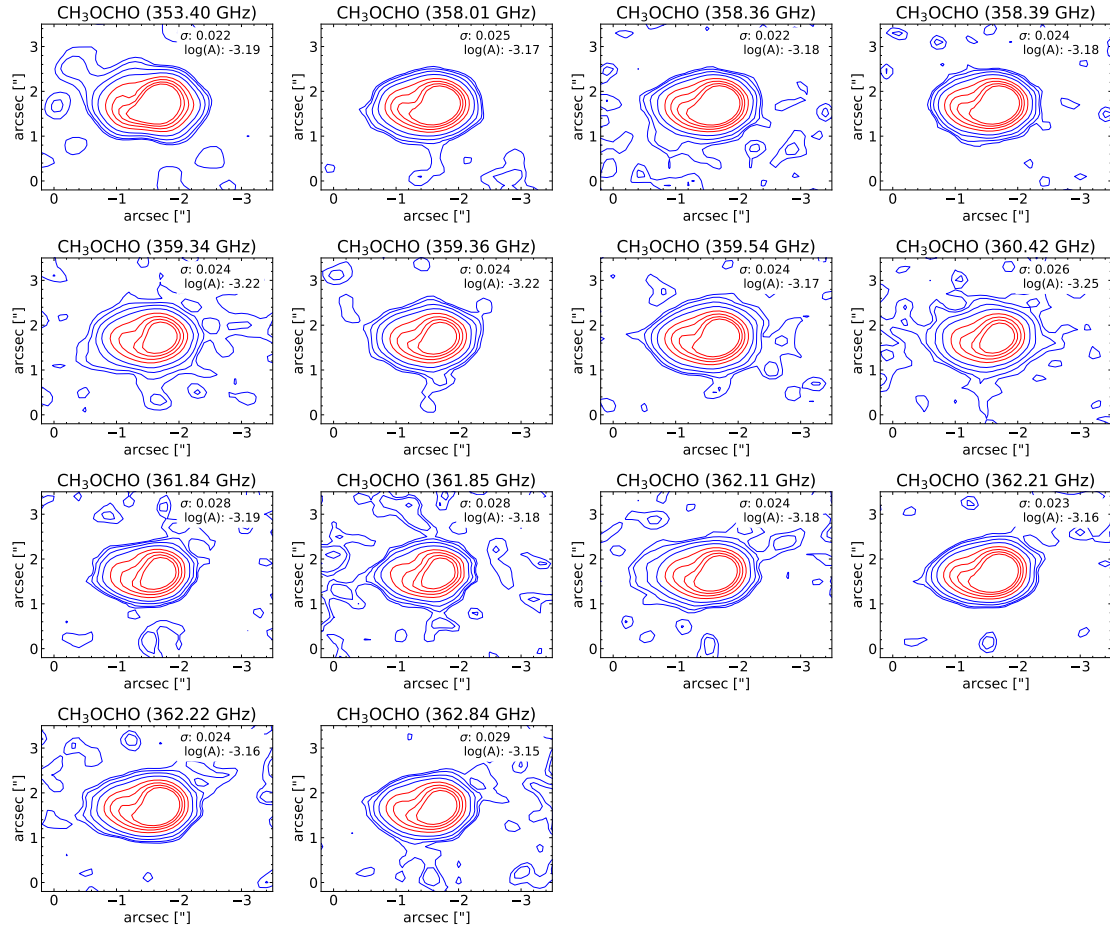


**Figure A.9:** Contour maps of CH<sub>3</sub>OCHO for IRAS16293B. The different levels are for  $3\sigma$ ,  $5\sigma$ ,  $10\sigma$ ,  $20\sigma$ ,  $40\sigma$ ,  $60\sigma$ ,  $80\sigma$ ,  $100\sigma$ . The Einstein A coefficient and  $\sigma$  is displayed on the plots.

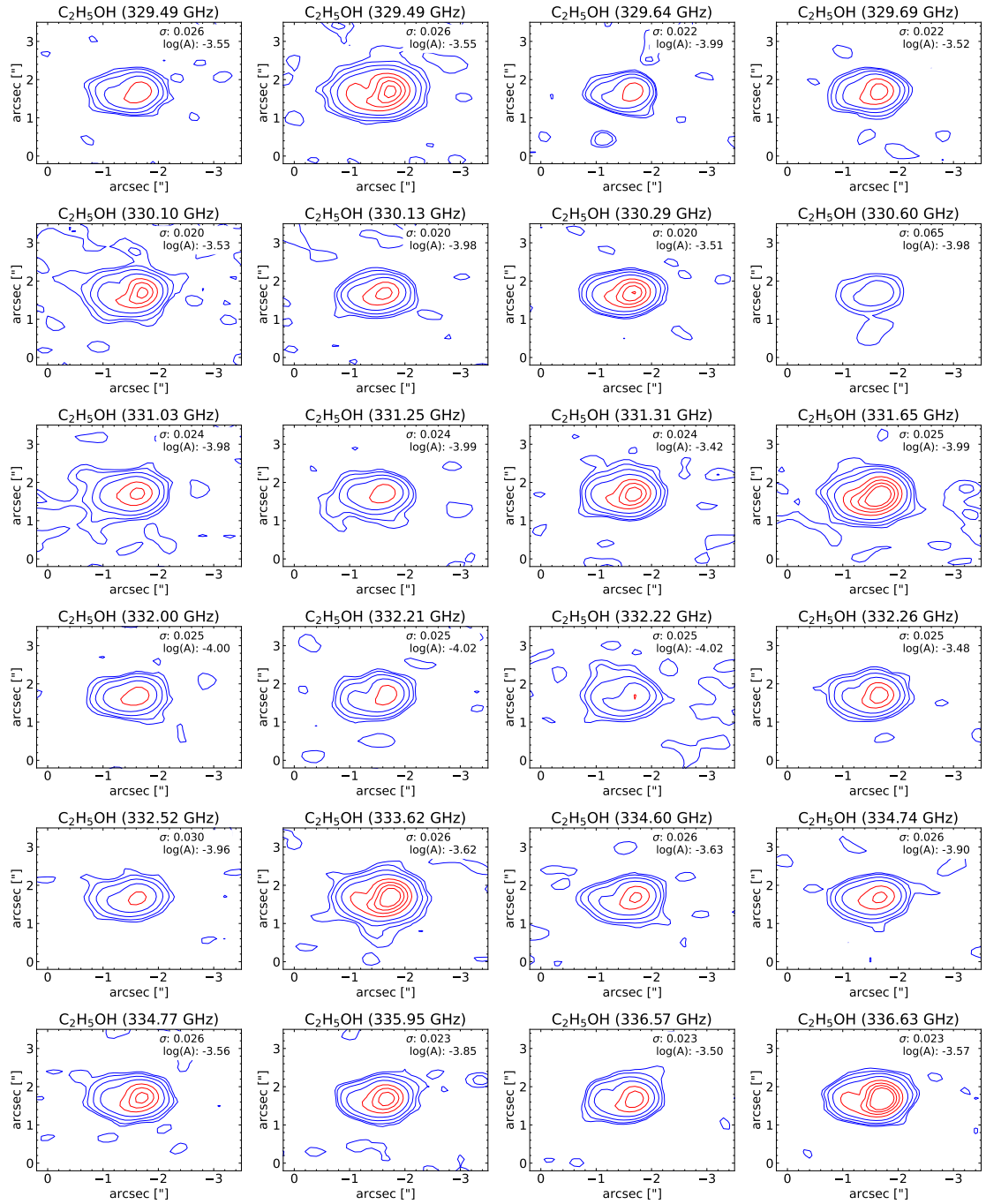


**Figure A.10:** Contour maps of  $\text{C}_2\text{H}_5\text{OH}$  for IRAS16293B. The different levels are for  $3\sigma$ ,  $5\sigma$ ,  $10\sigma$ ,  $20\sigma$ ,  $40\sigma$ ,  $60\sigma$ ,  $80\sigma$ ,  $100\sigma$ . The Einstein A coefficient and  $\sigma$  is displayed on the plots.

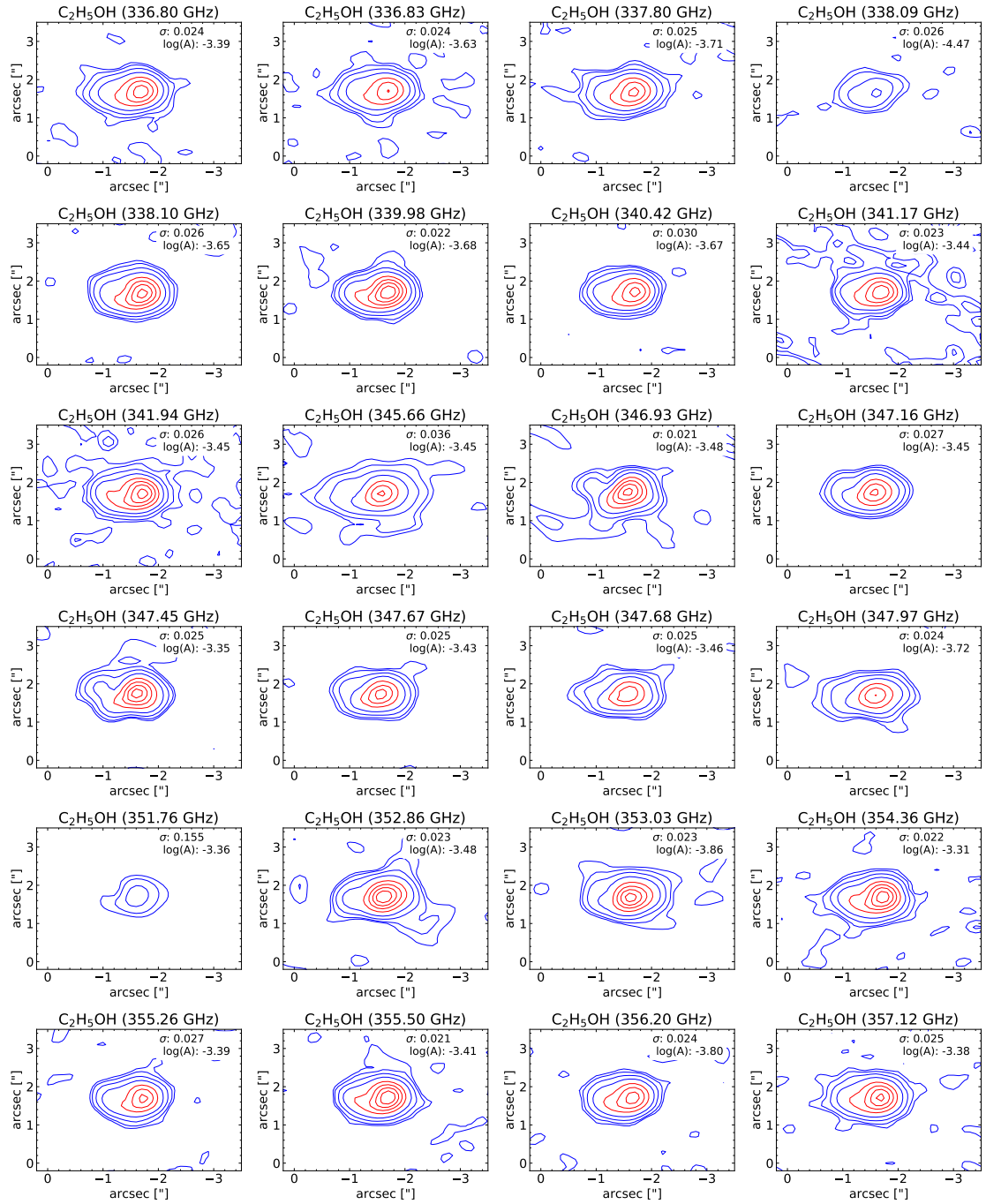


**Figure A.11:** Contour maps of  $\text{C}_2\text{H}_5\text{OH}$  for IRAS16293B. The different levels are for  $3\sigma$ ,  $5\sigma$ ,  $10\sigma$ ,  $20\sigma$ ,  $40\sigma$ ,  $60\sigma$ ,  $80\sigma$ ,  $100\sigma$ . The Einstein A coefficient and  $\sigma$  is displayed on the plots.

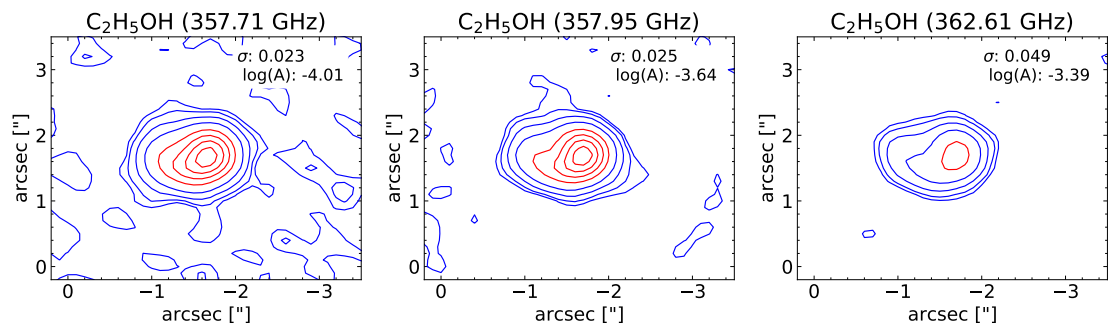


**Figure A.12:** Contour maps of  $\text{C}_2\text{H}_5\text{OH}$  for IRAS16293B. The different levels are for 3 $\sigma$ , 5 $\sigma$ , 10 $\sigma$ , 20 $\sigma$ , 40 $\sigma$ , 60 $\sigma$ , 80 $\sigma$ , 100 $\sigma$ . The Einstein A coefficient and  $\sigma$  is displayed on the plots.

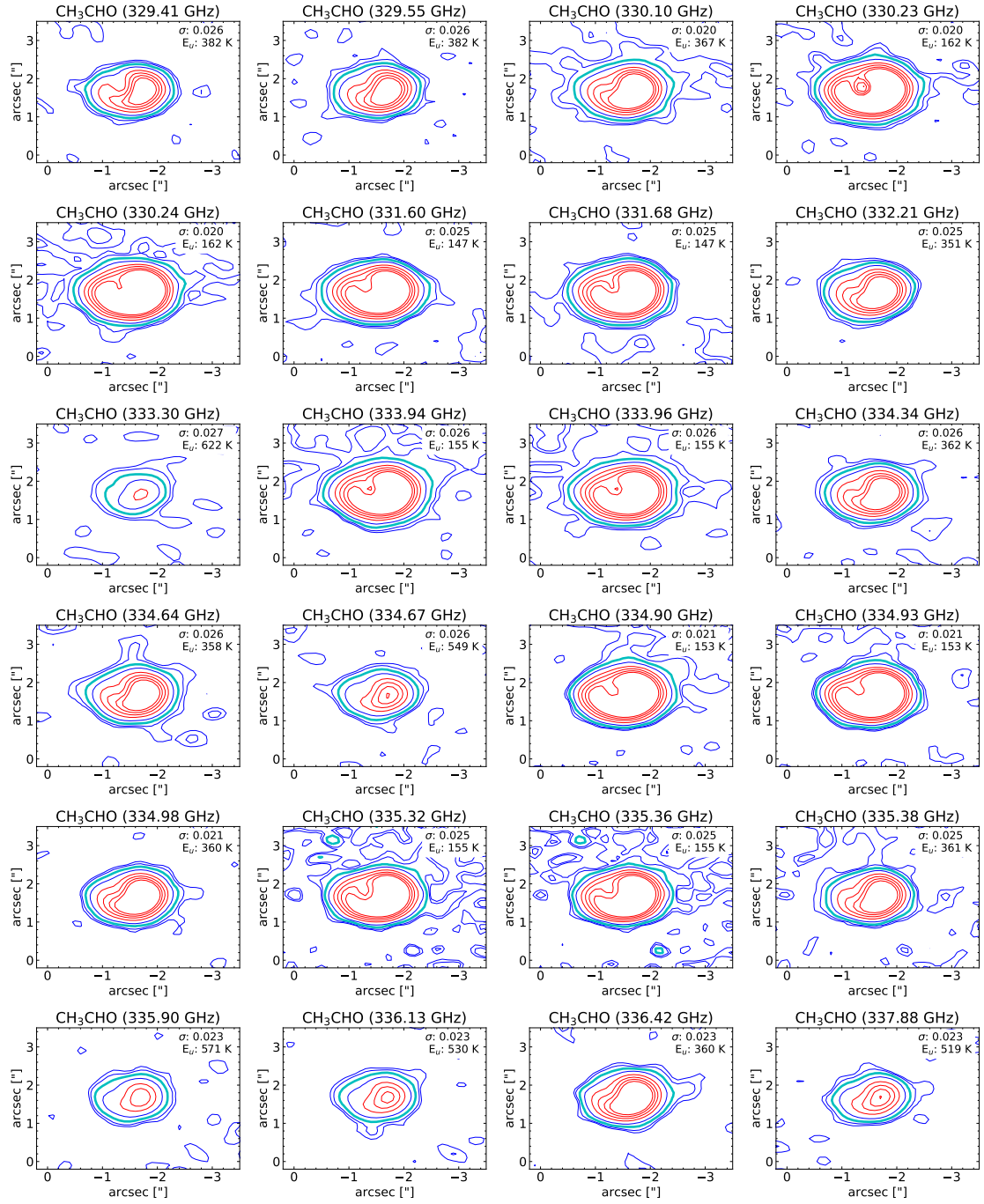


**Figure A.13:** Contour maps of  $\text{CH}_3\text{CHO}$  for IRAS16293B. The different levels are for  $3\sigma$ ,  $5\sigma$ ,  $10\sigma$ ,  $20\sigma$ ,  $40\sigma$ ,  $60\sigma$ ,  $80\sigma$ ,  $100\sigma$ , where the  $10\sigma$  contour is in cyan. The upper energy and  $\sigma$  is displayed on the maps.



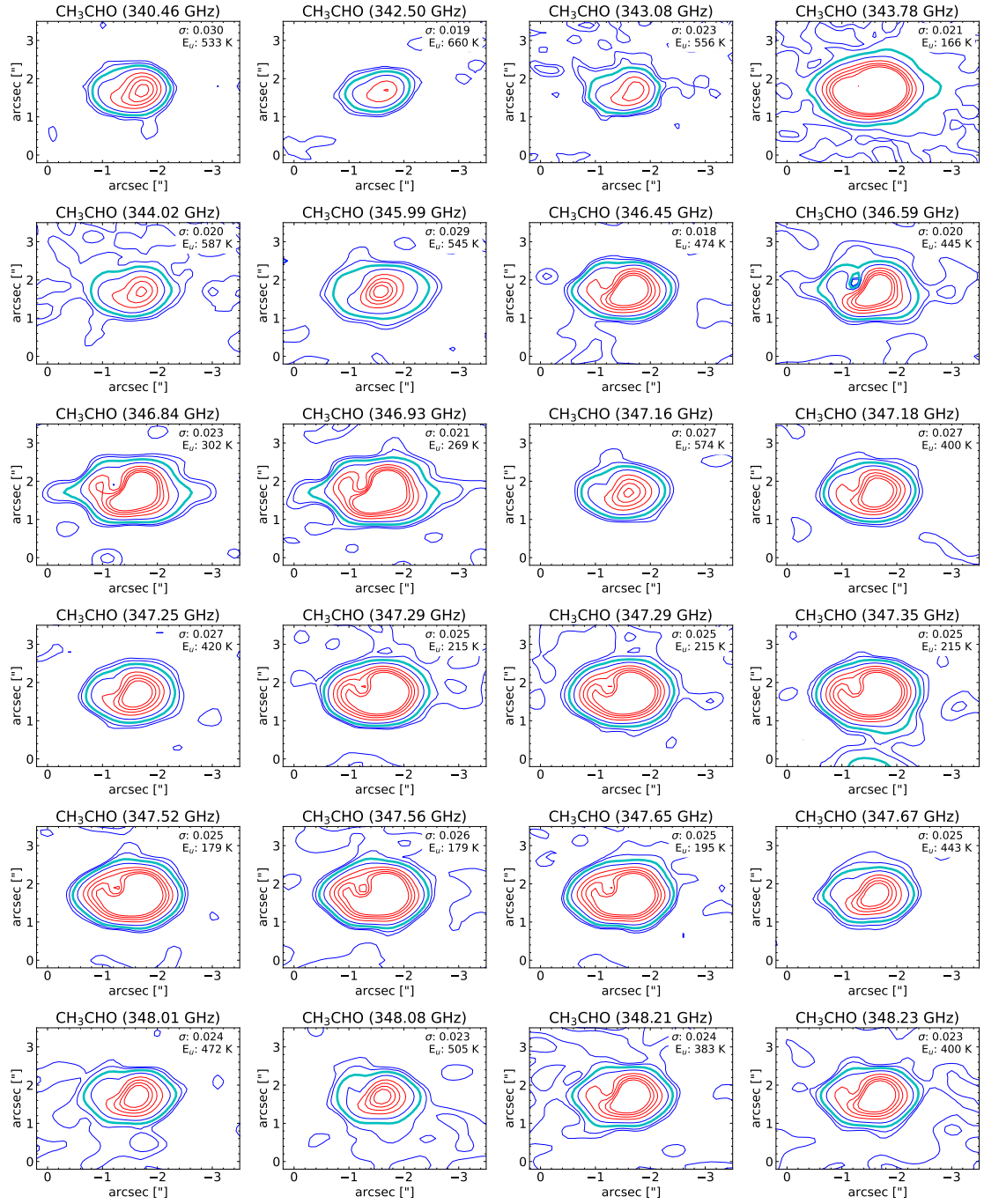


**Figure A.14:** Contour maps of  $\text{CH}_3\text{CHO}$  for IRAS16293B. The different levels are for  $3\sigma$ ,  $5\sigma$ ,  $10\sigma$ ,  $20\sigma$ ,  $40\sigma$ ,  $60\sigma$ ,  $80\sigma$ ,  $100\sigma$ , where the  $10\sigma$  contour is in cyan. The upper energy and  $\sigma$  is displayed on the maps.



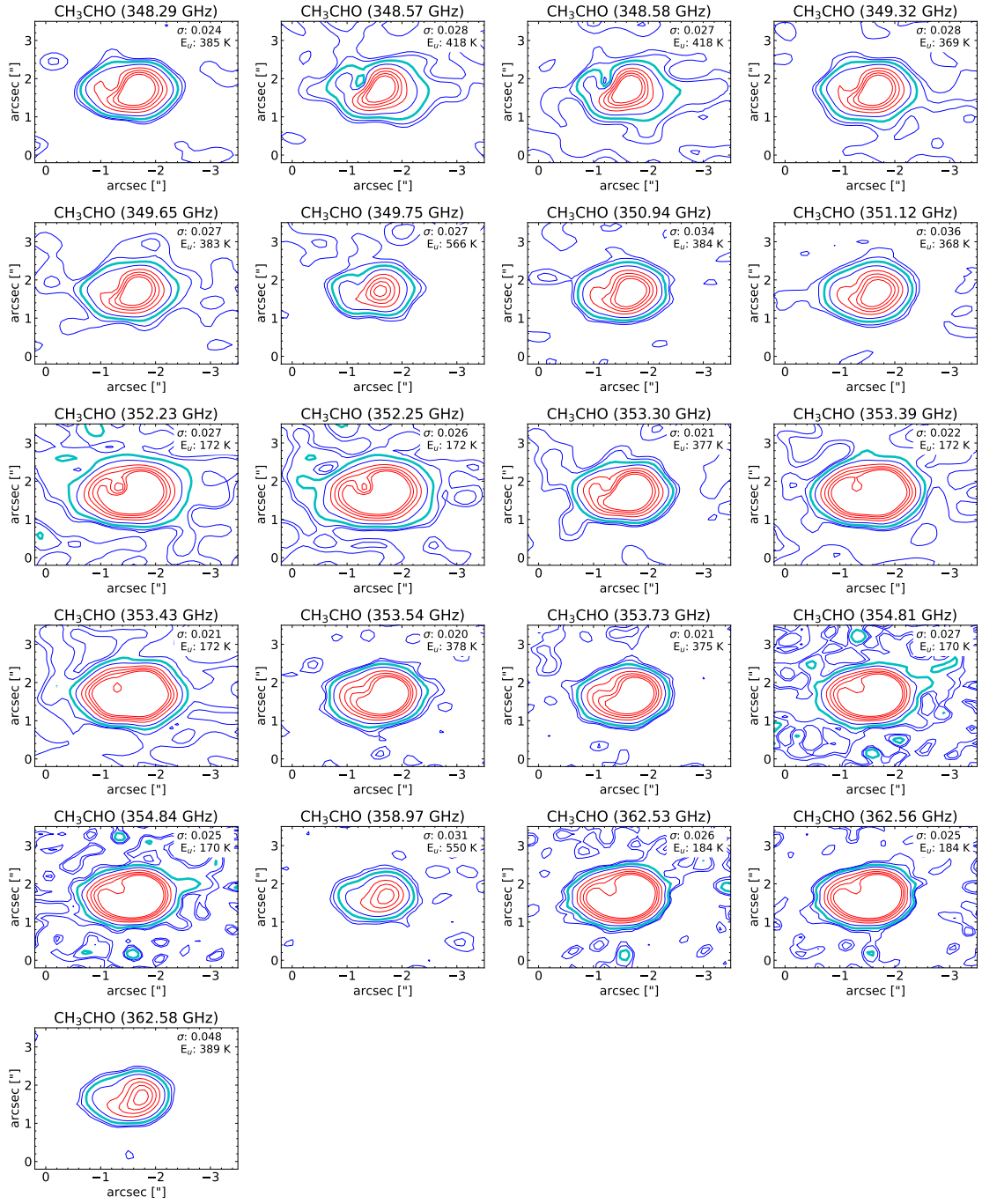


**Figure A.15:** Contour maps of  $\text{CH}_3\text{CHO}$  for IRAS16293B. The different levels are for  $3\sigma$ ,  $5\sigma$ ,  $10\sigma$ ,  $20\sigma$ ,  $40\sigma$ ,  $60\sigma$ ,  $80\sigma$ ,  $100\sigma$ , where the  $10\sigma$  contour is in cyan. The upper energy and  $\sigma$  is displayed on the maps.

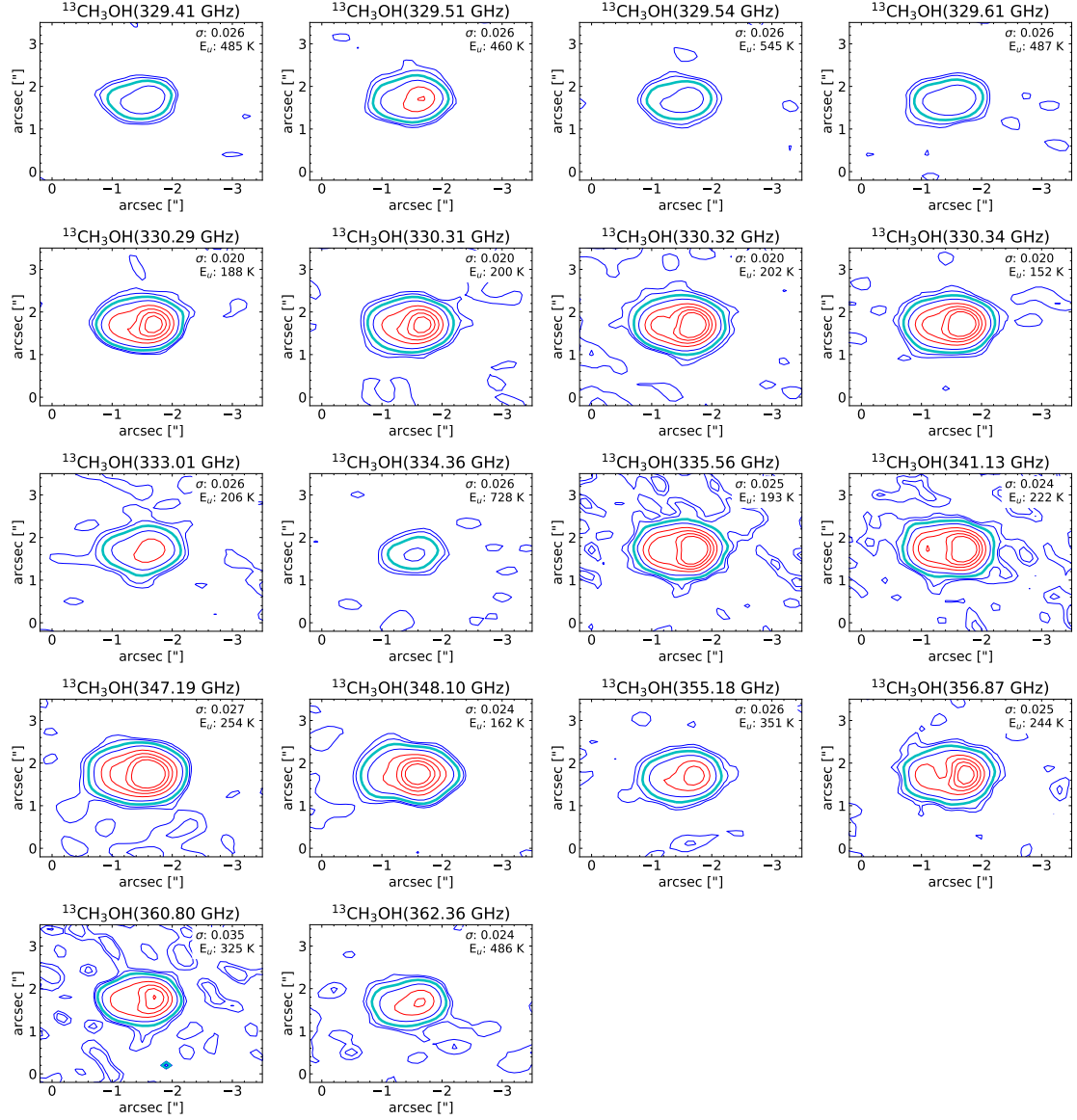


**Figure A.16:** Contour maps of  $^{13}\text{CH}_3\text{OH}$  for IRAS16293B. The different levels are for 3 $\sigma$ , 5 $\sigma$ , 10 $\sigma$ , 20 $\sigma$ , 40 $\sigma$ , 60 $\sigma$ , 80 $\sigma$ , 100 $\sigma$ , where the 10 $\sigma$  contour is in cyan. The upper energy and  $\sigma$  is displayed on the maps.

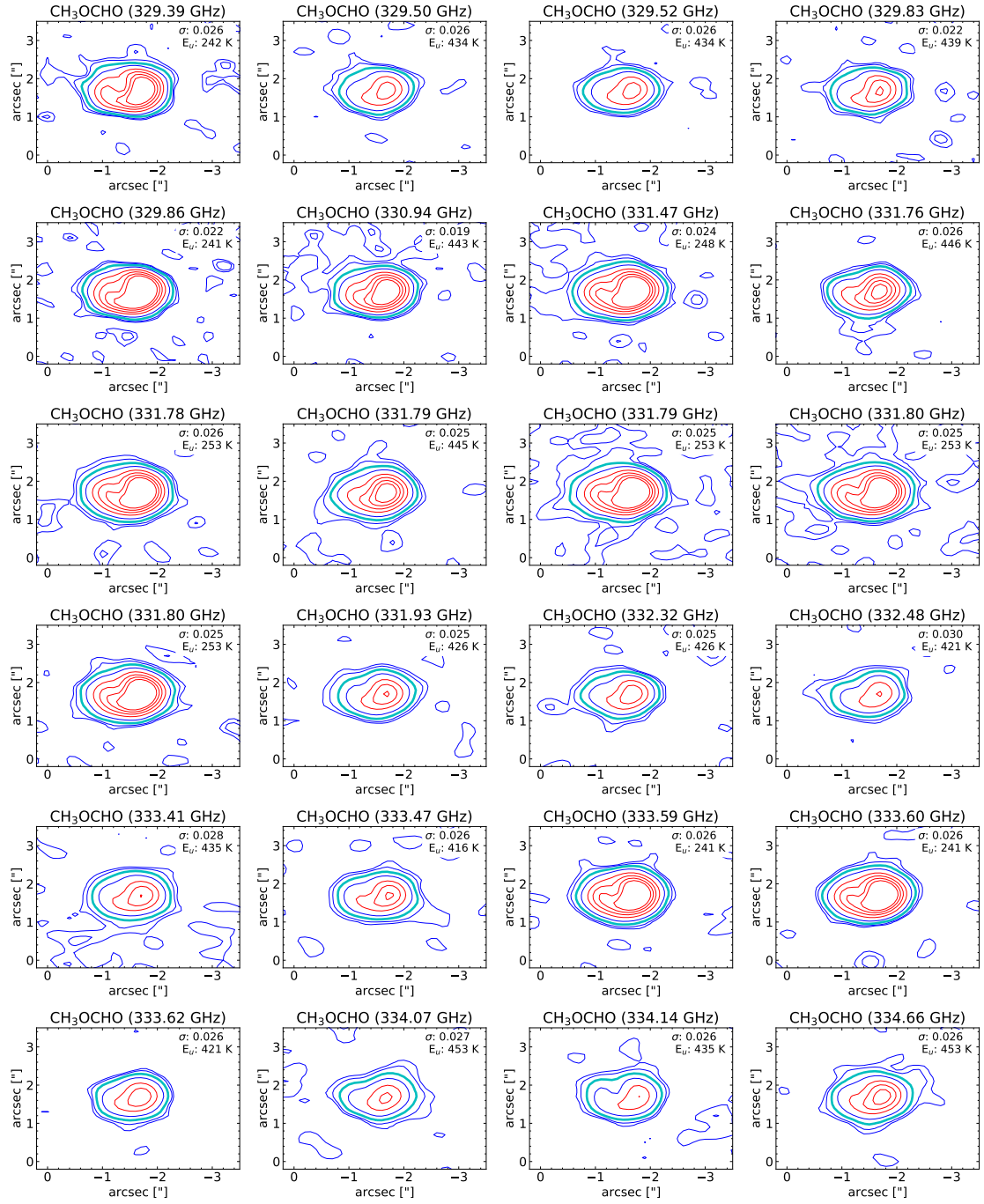


**Figure A.17:** Contour maps of CH<sub>3</sub>OCHO for IRAS16293B. The different levels are for 3 $\sigma$ , 5 $\sigma$ , 10 $\sigma$ , 20 $\sigma$ , 40 $\sigma$ , 60 $\sigma$ , 80 $\sigma$ , 100 $\sigma$ , where the 10 $\sigma$  contour is in cyan. The upper energy and  $\sigma$  is displayed on the maps.

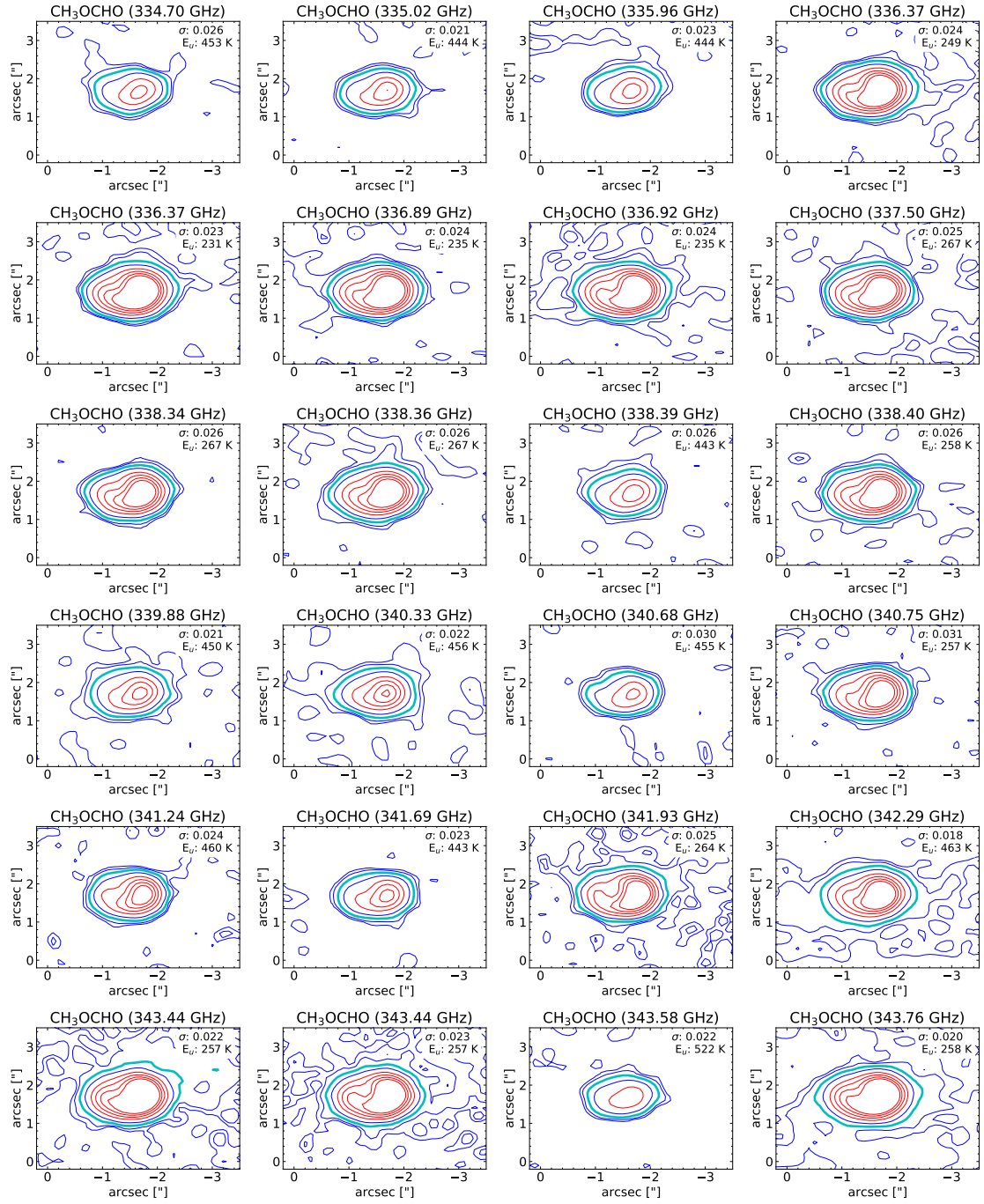


**Figure A.18:** Contour maps of CH<sub>3</sub>OCHO for IRAS16293B. The different levels are for  $3\sigma$ ,  $5\sigma$ ,  $10\sigma$ ,  $20\sigma$ ,  $40\sigma$ ,  $60\sigma$ ,  $80\sigma$ ,  $100\sigma$ , where the  $10\sigma$  contour is in cyan. The upper energy and  $\sigma$  is displayed on the maps.

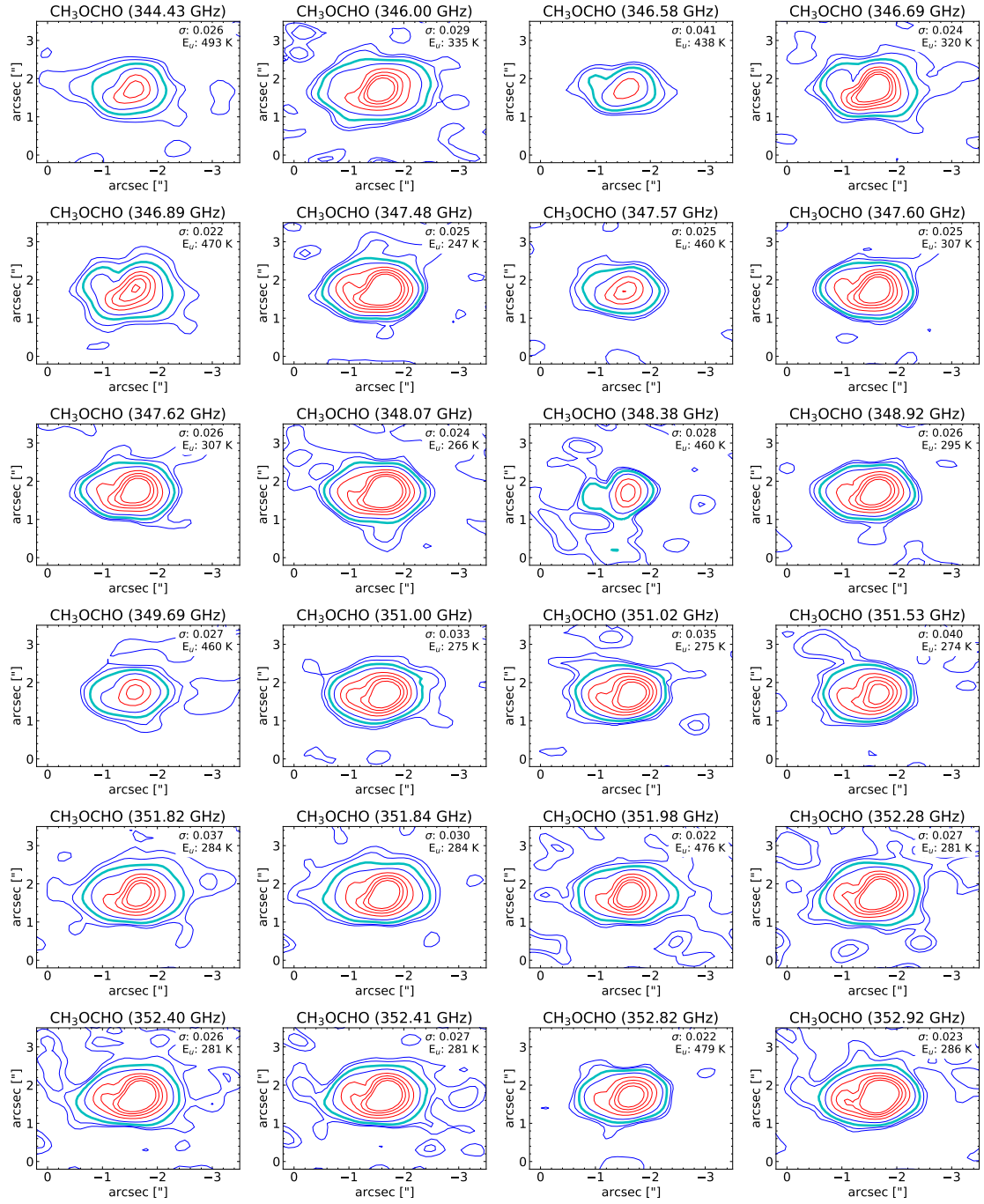


**Figure A.19:** Contour maps of CH<sub>3</sub>OCHO for IRAS16293B. The different levels are for 3 $\sigma$ , 5 $\sigma$ , 10 $\sigma$ , 20 $\sigma$ , 40 $\sigma$ , 60 $\sigma$ , 80 $\sigma$ , 100 $\sigma$ , where the 10 $\sigma$  contour is in cyan. The upper energy and  $\sigma$  is displayed on the maps.

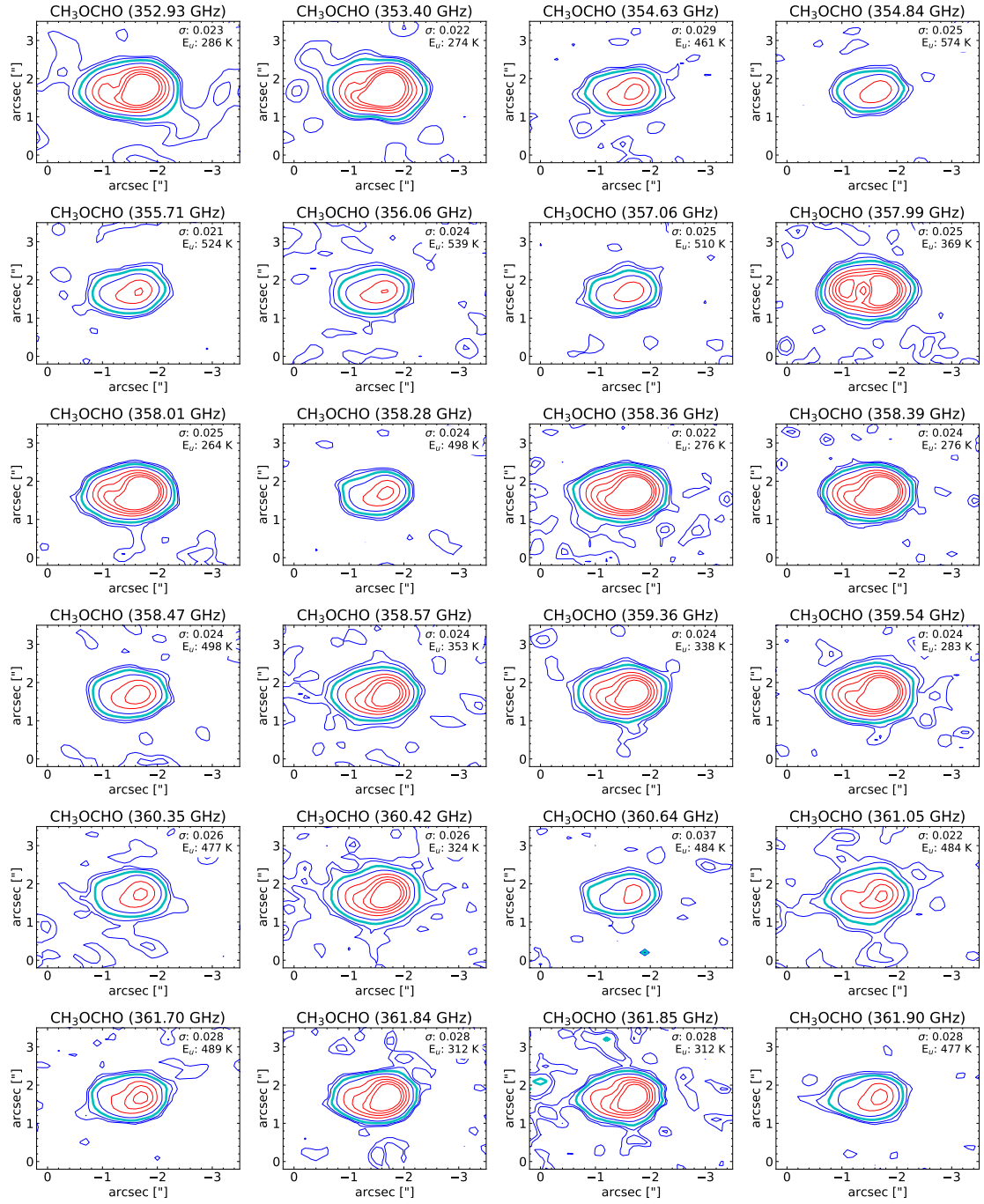


**Figure A.20:** Contour maps of CH<sub>3</sub>OCHO for IRAS16293B. The different levels are for 3σ, 5σ, 10σ, 20σ, 40σ, 60σ, 80σ, 100σ, where the 10σ contour is in cyan. The upper energy and σ is displayed on the maps.



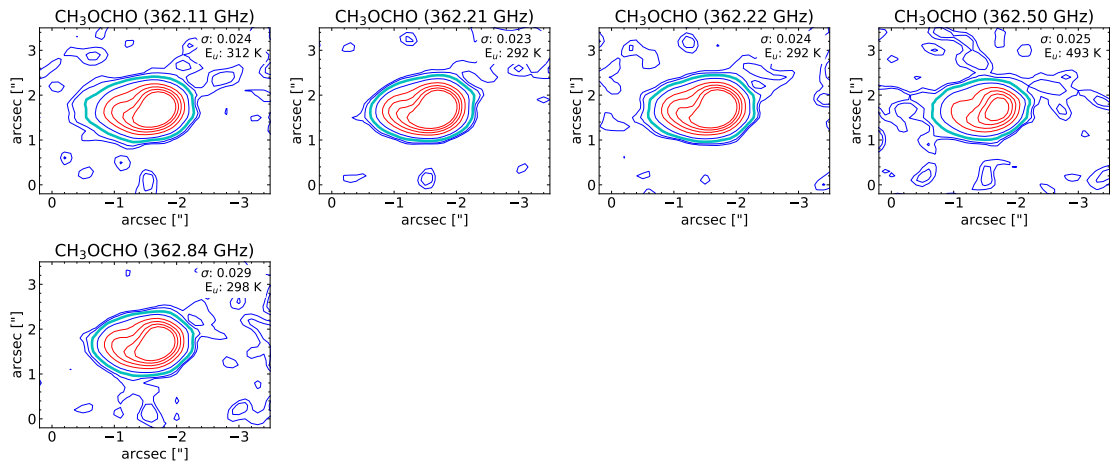


**Figure A.21:** Contour maps of  $\text{CH}_3\text{OCHO}$  for IRAS16293B. The different levels are for  $3\sigma$ ,  $5\sigma$ ,  $10\sigma$ ,  $20\sigma$ ,  $40\sigma$ ,  $60\sigma$ ,  $80\sigma$ ,  $100\sigma$ , where the  $10\sigma$  contour is in cyan. The upper energy and  $\sigma$  is displayed on the maps.

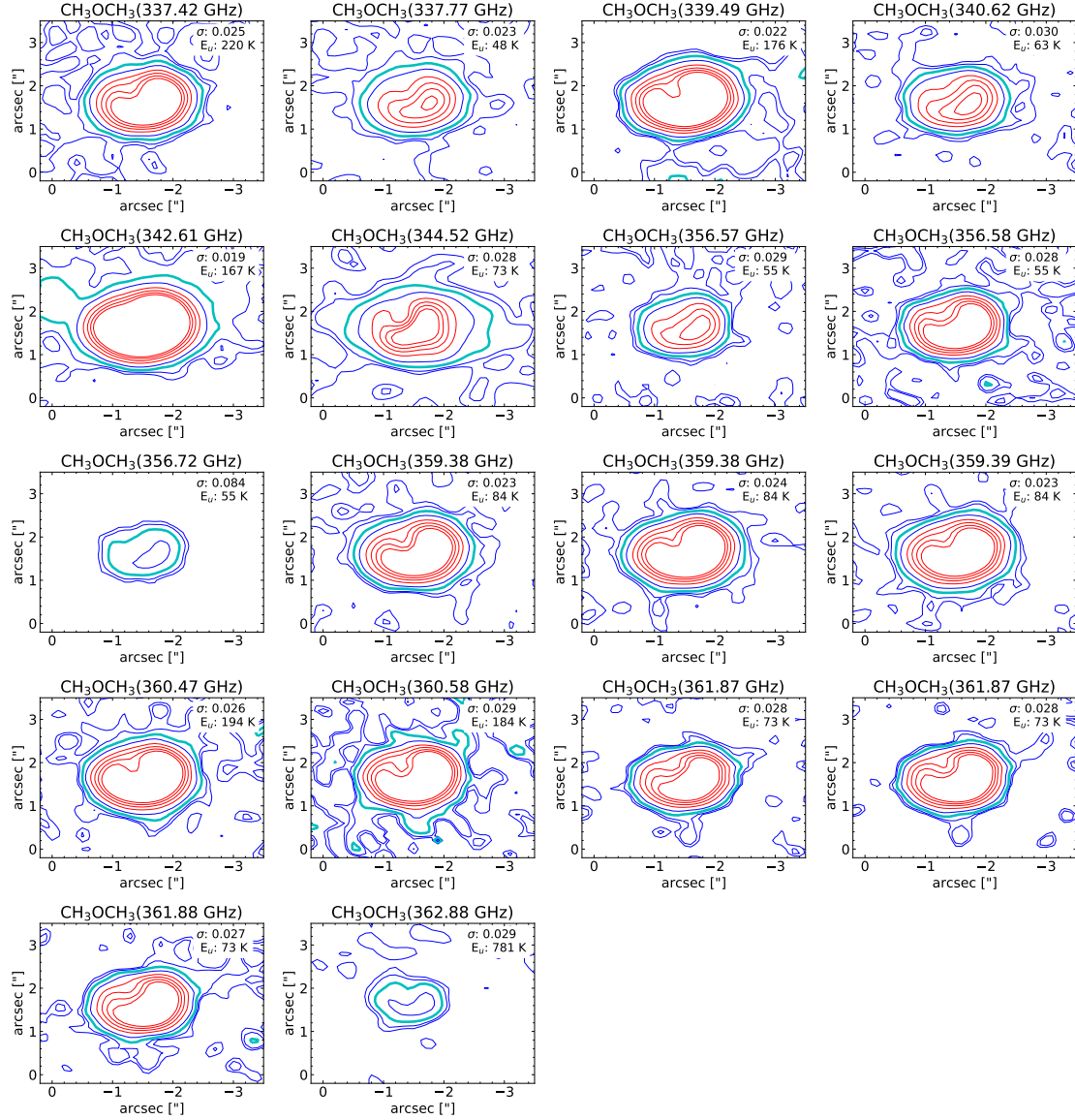


**Figure A.22:** Contour maps of  $\text{CH}_3\text{OCH}_3$  for IRAS16293B. The different levels are for 3 $\sigma$ , 5 $\sigma$ , 10 $\sigma$ , 20 $\sigma$ , 40 $\sigma$ , 60 $\sigma$ , 80 $\sigma$ , 100 $\sigma$ , where the 10 $\sigma$  contour is in cyan. The upper energy and  $\sigma$  is displayed on the maps.